IChF

Institute of Physical Chemistry
Polish Academy of Sciences
Kasprzaka 44/52, 01-224 Warszawa

LYOTROPIC LIQUID CRYSTALS -

FROM CUBOSOMES TO SMALL MONOCRYSTALS

A-21-7
K-g-160
K-g-156
K-g-158

thesis

by

Larisa Latypova

Supervisor D.Sc. Wojciech Góźdź

Dissertation was prepared within the program of international PhD Studies at the
Institute of Physical Chemistry of Polish Academy of Sciences in Warsaw

Warsaw, November 2013

Content

3

List of figures

I. Introduction

Amphiphilic molecules in aqueous solutions are known to self-assemble into a large variety of lyotropic liquid crystal phases. In particular, in the so-called bicontinuous inverted phases, the molecules self-assemble into a unique liquid bilayer which separates two interwoven labyrinths filled with water. In systems encountered in nature, three bicontinuous mesophases with cubic symmetry are the most common: gyroid – Ia3d, double diamond Pn3m, and simple cubic – im3m. In Ia3d, Pn3m and Im3m, the bilayer has shapes of respectively G, D and P infinite periodic minimal surfaces while in the sponge phase L3, the shape of the bilayer displays only a short range order. Due to their topology and liquid crystal structure bicontinuous lyotropic phases have original equilibrium and out-of-equilibrium properties that we intend to explore both by experimental and theoretical means. Surface properties are expected to be unusual because the requirement of the bilayer's continuity plays a crucial role here.

I.1. Liquid crystals and bicontinuous liquid crystalline phases

Liquid crystals are the state of matter which have properties of liquids with long range order characteristic for solids. Liquid crystals can be divided into two branches: thermotropic liquid crystals and lyotropic liquid crystals. Thermotropic liquid crystals exhibit phase transitions between the liquid crystalline phases with the changes of the temperature. Lyotropic liquid crystals have phase transitions between the liquid crystalline phase as the temperature and the concentration of the amphiphilic molecules from which they have been formed are changed. Here we focus on the formation of the lyotropic liquid monocrystals and dispersed particles called cubosomes.

Lyotropic liquid crystals are mixtures of amphiphilic molecules and solvents. Lyotropics (as they can be also called) are formed of the amphiphilic molecules that are self-assembled into supermolecular structures (Fig. 1). These supermolecular structures are the basic units of the lyotropic liquid crystals. In liquid crystals the basic units exhibit orientational order and positional order along some directions. These materials can flow but have characteristic optical properties of solid crystals like anisotropy.

Amphiphilic molecules are a necessary ingredient of the lyotropic liquid crystals. Here work we work with two amphiphilic molecules: monoolein and phytantriol.
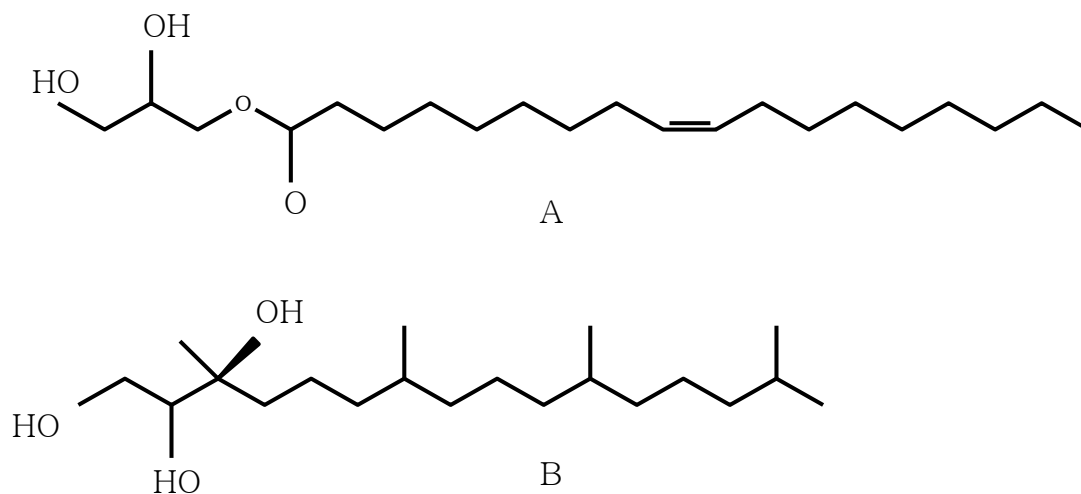
Fig. 1. A. The structure of monoolein, B. The structure of phytantriol.

When the concentration of the surfactant in water increases different self-assembled aggregates can be formed (Fig. 2). Depending on temperature, type and concentration of the solvents, there may exist direct or inverted molecular agregates in the lyotropic mesophases. The micellar isotropic phase L1 is the first phase appearing when the concentration of the surfactant reaches the specific concentration called critical micelle concentration. Depending on the concentration of the amphiphilic molecules in the solution, micelles can have spherical shape (mainly at low amphiphilic molecular concentrations) or have non-spherical shapes (at high amphiphilic molecular concentrations) (see Fig. 2). In the lamellar phase layers of surfactants are organized in such a way that a sandwich-like structure is formed. Lamellar phase is labelled as Lα phase (see Fig. 2). Hexagonal phase consists of the molecules forming the cylinders which are arranged in a hexagonal lattice (see Fig. 2).

There are three most common bicontinuous liquid crystalline phases: Pn3m, Ia3d, and Im3m (Fig. 3). These names correspond to symmetries (space groups) of the corresponding phases. Ia3d phase was observed both in polar and non-polar solvents. This phase consists of the rods, linked three by three, forming a three-dimensional structure with two networks interwoven and disconnected. The structure of this phase can be modeled also in terms of a triply periodic minimal surface called gyroid or G-surface. Triply periodic minimal surfaces are characterized by the mean curvature which is equal zero in every point of the surface. Pn3m phase is formed by the interconnected rods linked

tetrahedrally which form three dimensional networks. Im3m phase consists of the rods which are linked six-by-six and oriented along the edges of a cube. Investigation of the symmetry of the phases is done using the x-ray diffraction. Bragg peaks which are presented in the spectrum lead to the identification of the cubic symmetry of the structures.

Sponge phase is an optically isotropic phase (Fig. 2). The sponge phase is bicontinuous but does not have crystalline order like cubic phases do. The structure of the sponge phase was investigated by freeze-fracture electron microscopy. Sponge phase is different from the cubic phase, it doesn't possess periodicity.

Cubic phases can be used in drug delivery [1]. Particularly, cubic phases are very important for the delivery of drugs which are not water soluble. Cubic phase can also be used for protein encapsulation and this property of cubic liquid crystalline phase may be exploited in many applications which are related to the delivery of the proteins inside a human body. Some proteins and peptides exhibit controlled release within a cubic phase [2, 3, 4].
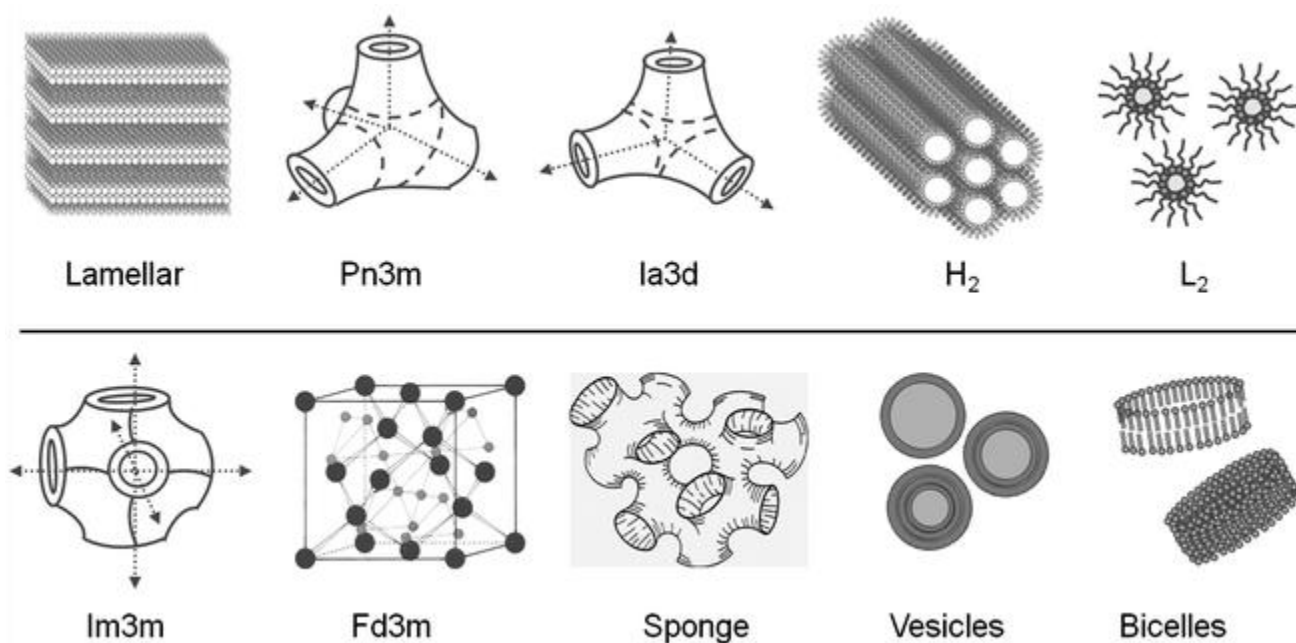
Fig. 2. Structures that can be formed in surfactant/water solution [5].

Cubic phase are also used as long-term storage material for some labile proteins. Ability to encapsulate proteins and enzymes makes cubic phases useful for applications in biosensing and as

biofuel cells. A common example is a blood glucose biosensor created on the enzyme glucose oxydase to determine the concentration of glucose in blood [6].

Cubosomes (nanoparticles made of cubic phases) with redox enzymes are applied as catalyst to convert chemical energy into electrical energy [7, 8, 9, 10]. Cells that convert chemical energy into electrical current using the redox enzymes as catalysts are called biofuel cells. The current which is generated during red-ox process can be supplied to the sensors and micro devices. Nazaruk at al. [6] demonstrated that liquid crystalline phase can be used for enzyme immobilization in the biofuel cells because it holds enzyme in active form close to the electrode surface and facilitates fast transport pathways for surface and products through the film [6]. Moreover, liquid crystalline phase provides biocompatible environment [6]. They are used for immobilizing such enzymes as laccase, glucose oxidase, and pyranose oxydase. [8, 11, 12, 13]. The liquid crystalline phase built of the monoolein is used for immobilizing enzymes. The monoolein is stable in contact with water, it is also transparent and highly viscous [10].

Luzzati was the first who discovered cubic liquid crystalline phase in the systems consisting of water and lipid [14, 15]. Fontell observed cubic liquid crystalline phases in ternary amphiphile/water/oil systems. In parallel, biologists discovered cubic liquid crystalline phases in plant leaf plastid membranes [16]. Larsson examined cubic liquid crystalline phase in details by NMR and x-ray scattering. He suggested that at the sides of the monolayer two continuous regions of hydrophobic and hydrophilic nature are contained [17] (monolayer as well as the bilayer can form cubic lattice). These observations led to the conclusion that cubic phase can be described mathematically within the concepts of periodic minimal surfaces [18]. The three types of the cubic phase identified in lipid systems can be mathematically modeled by the Schwarz diamond (D) and primitive (P) and on the Schoen gyroid (G) minimal surfaces (Fig. 3).

Bicontinuous cubic phases consist of the bilayer (or monolayer) formed the surfactants. The surfactant forms a complex 3-dimentional network with different symmetry and creates two interwoven channels: in the case of a monolayer, one of water and another of oil; in the case of a bilayer – both channels are filled with water or oil. These channels do not intersect ever. Since the channels never intersect these phases are called bicontinuous: they are continuous from one side and from another of the monolayer or bilayer. Cubic phases can be divided into inverse cubic phases and direct cubic phases. This division depends on which kind of channel (water or oil one) is wrapped inside the structure. 'In this case, the terminology of direct or inverted structures refers to the

relative concentrations of polar and non-polar solvents with respect to the concentration of the principle amphiphile. In direct structures, the polar solvents have the largest concentration; in inverted structures, the largest concentration is of non-polar solvents' [20].
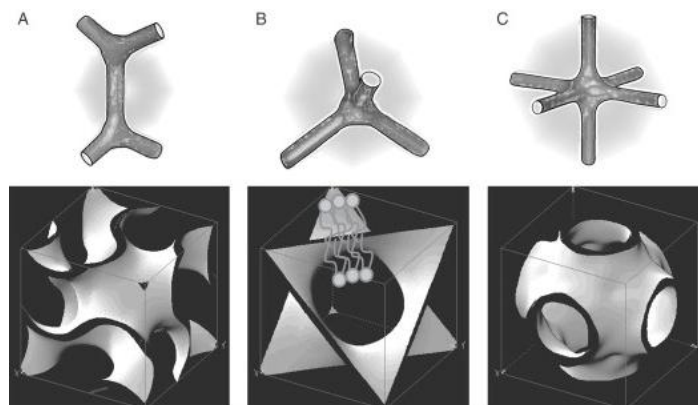
Fig. 3. A. G-surface (gyroid surface); B. D-surface (diamond surface); C. P-surface (primitive surface) [19].

The most common surfactant that can form cubic liquid crystalline phase is monoolein (MO). It is considered that MO has a large cross-sectional area of its hydrophobic tail region that leads to the ratio of the hydrophilic head group area slightly larger than one 1.03. Monoolein/water systems form a double diamond phase (D) surface, but it was also shown that at lower water level phase transition from the double diamond phase (D) to gyroid (G) phase occurs. A simple cubic phase (P) structure can also be formed in water-MO system in the presence of the third component either a casein [21] or a block copolymer [22].

Fig. 4 shows the phase diagram for monoolein/water system. As it can be seen from this diagram, cubic phases occupy a relatively small region. There are also regions of two cubic phase coexistence as well as regions of one cubic phase. As it can be seen from the phase diagram monoolein can form cubic phases with two different symmetries: diamond and gyroid. To obtain the phase of primitive symmetry the second surfactant has to be added. This surfactant is called 1,2-distearoyl-sn-glycero-3-phosphoglycerol, sodium salt or, shorter, DSPG.

Physical properties of the cubic phases formed from monoolein or phytantriol are the same. Cubic phases are optically isotropic [24]. They are viscoelastic liquids with different stiffness: some of them are very viscous others can almost flow as a liquid. It was shown by x-ray (or neutron) low-angle diffraction that they have crystalline structure [25].

13
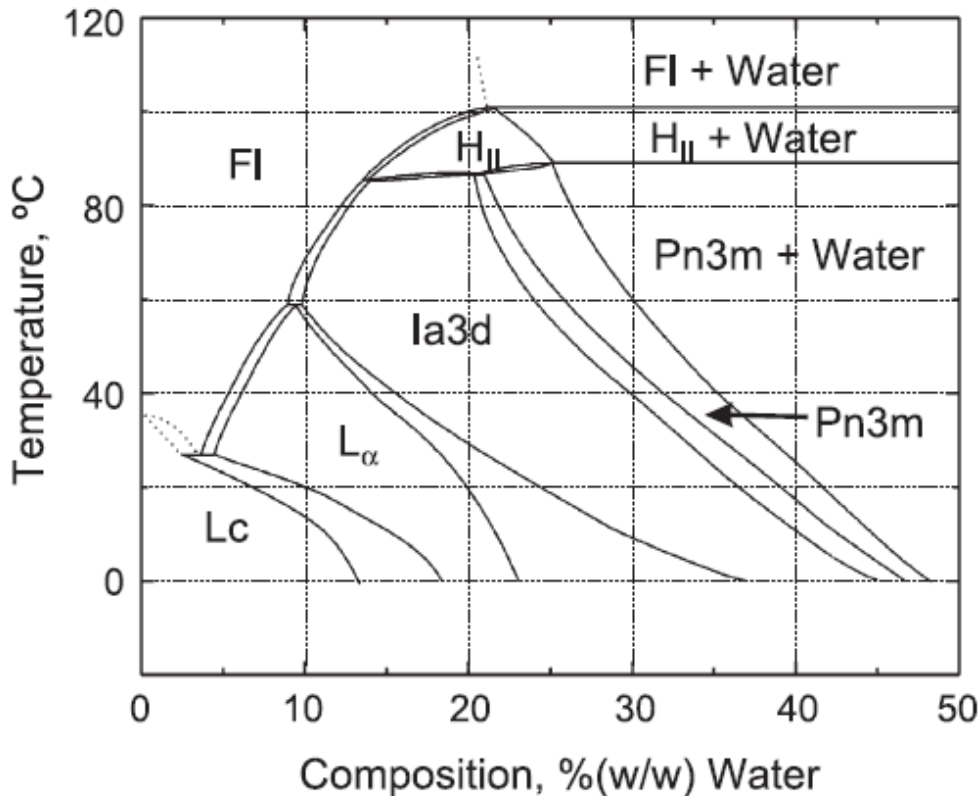
Fig. 4. The temperature-composition phase diagram for the binary monoolein/water system [23].

I.2. Monocrystals

First observations of the shapes of the lyotropic cubic crystals were made by F.C. Winsor [26]. There are two methods of the investigation the growth of the facets of the lyotropic cubic crystals called hygroscopic and isoplethal. They were developed in order to perform the controlled growth of the lyotropic liquid cubic crystals. The shapes of the crystals were observed by means of an optical microscope [27].

Using these methods it is possible to observe:

- Ia3d crystals which are grown from L2 droplets in humid atmosphere [28, 29]. Usually, these crystals are oriented with their (211) facets parallel to glass or mica substrates. Characteristic facets are: (112), (220), (321), (400) and (420).
- Pn3m crystals from L2-in-L1 droplets [30] with their planes (111) parallel to glass. Characteristic facets are: (111), (220), (400), (311) and (331).

- Im3m crystals which are grown from L2-in-L1 droplets with their (100) planes parallel to glass surface. Characteristic facets are: (100), (111), (110) and (211).

The experimental setup for hygroscopic method is shown in Fig. 5. The sample is a cubic crystal of Ia3d symmetry on the mica sheet or glass plate. It is in thermal contact with a copper plate whose temperature $T_s = T_r + \Delta T$ is regulated by means of two Peltier elements located on the thermalized aluminium base, where T_r is the temperature of the reservoir of water, made of copper. The temperatures T_r and T_s are regulated with accuracy better than 0.01°C. The relative humidity h at the sample level is given by the formula $h(T_s, T_r) = p_s(T_r)/p_s(T_s) * 100\%$, where $p_s(T)$ expresses the dependence of the saturated vapour pressure as a function of temperature. In order to change the humidity it is more convenient to keep the temperature T_r of water reservoir constant and to vary the temperature $T_s = T_r + \Delta T$ of the sample holder.

Using the hygroscopic method the phase diagram Temperature-vs-Humidity can be constructed. Another method is called isoplethal – the method we used in our experiments. This method is described in detail in chapter II.2.3. The experimental setup for this method is shown in Fig. 16. Using the isoplethal method the phase diagram Temperature-vs-Concentration can be constructed.
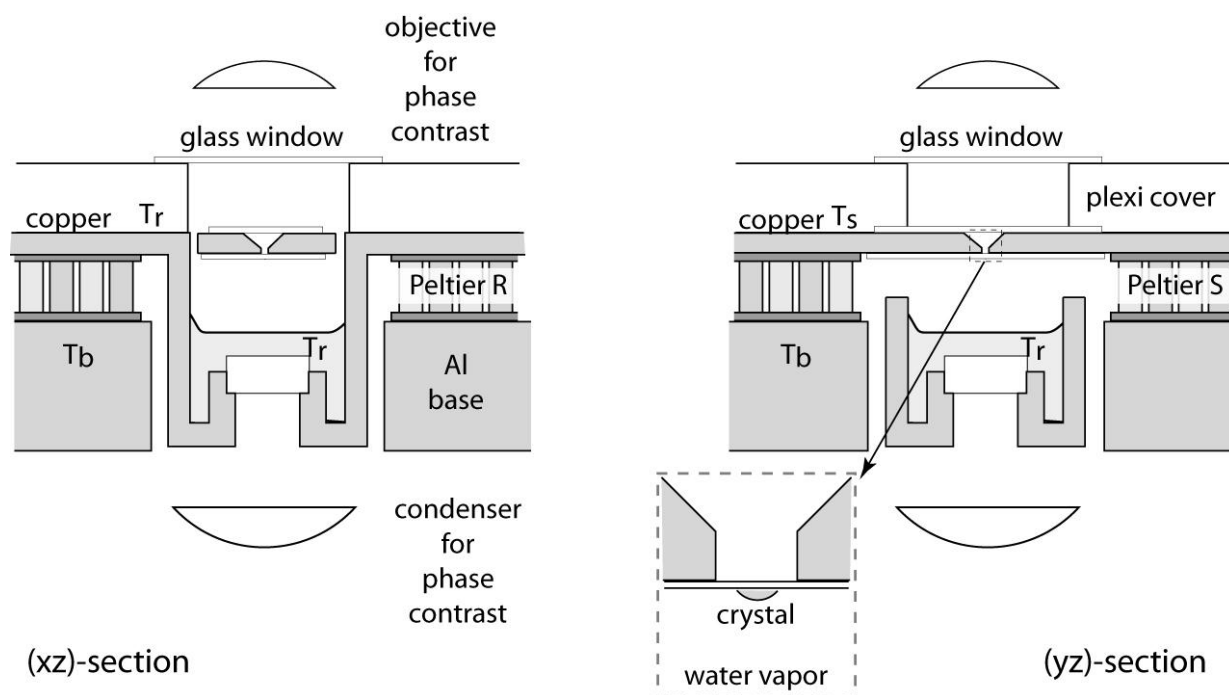
Fig. 5. Experimental setup. The distance between the Peltier elements can be adjusted. The temperature T_r and T_s are regulated separately by means of a LabView computer program [31].

I.3. Cubosomes

The unique property of the bicontinuous liquid crystalline phase is the possibility to be dispersed into small nanoparticles called cubosomes. Cubosomes have very often cubic shapes. An example of such a cubosome obtained by theoretical modeling is presented in Fig. 6. The first work where the word cubosome appeared was the review by Larsson on the implications of cubic phases to biological membranes [32]. Earlier, dispersed particles of the bicontinuous cubic phase were found during the investigation of the processes of fat digestion. According to this process oil combines with lipase and bile salts that stimulates stomach contents [33]. Oil droplets in contact with lipase create small particles of the cubic phase.
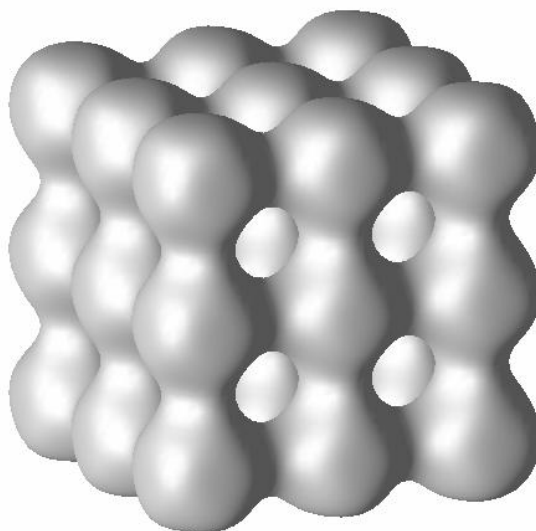
Fig. 6. Cubosome of the P symmetry calculated theoretically using Landau-Brazovskii functional.

Cubosomes may be formed in mixtures of amphiphilic molecules with water if such mixtures are characterized by a miscibility gap. Phytantriol, monoolein and some glycolipids can be used for cubosome formation. Only the phase diagram for phytantriol-water system and monoolein/water sytems are known. We investigate the phase diagram of the ternary phytantriol-water-ethanol mixture.

There are two different approaches for cubosomes processing: top-down and bottom-up techniques. Most cubosomes are produced by top-down-technique, where bulk cubic phase is produced first and then by high energy process cubosomes are formed. Top-down techniques include the dispersion

procedure with high energy input such as ultrasonication or high pressure homogenization. Unfortuntely, the existing studies can't give precise information about the mechanism of cubosomes's formation by top-down process. Systems prepared from monoolein have a complex behavior: their structure varies from dispertion to the colloidal scale [34]. In the studies of Siekmann et al. [34] the double diamond phase was used as the bulk cubic phase for top-down approach but after homogenization cubosomes have predominantly the symmetry of the simpe cubic phase. The original D-phase was destroyed during the process of sonication or high pressure homogenization in the presence of Poloxamer 407. Recently, bottom-up techniques are starting to be more and more popular. Almegren [35], suggested the method of the preparation of the cubosomes by dispersion of micellar phase in water at 80^{0}C and slow cooling these droplets that causes gradual crystallization of micelles into cubosomes. Spicer et al. [36] diluted monoolein-ethanol solutions with aqueous Poloxamer 407 solutions in which cubosomes are formed by the spontaneous emulsification. There is another process to prepare cubosomes from a powdered precursor where spray-dried powders comprising monoolein coated with starch or dextran form cubosomes on simple hydration and the cubosomes are immediately stabilized by the polymers [37]. The aim of spray-drying method is to produce dry powder that forms cubosomes upon dilution in water. For this reason Spicer used three component water/starch/monoolein system. Experimental setup consists of a cylindrical chamber with a cyclone collector at the air exit. Nozzle is used to feed the liquid to be spray-dried. Drying occurs via contact of the feed liquid with heated drying air at 200°C that flows down past the nozzle. When cubic liquid crystalline material forms in the monoolein/starch/water system high shear is applied to disperse the high-viscosity cubic gel.

I.4. Applications of the liquid crystalline phases and cubosomes

Bicontinuous liquid crystalline phases are very promising materials for controlled release. Liquid crystalline phases can trap different substances, in particular drugs and enzymes. It has been also shown that bicontinuous structures formed in a human body are similar to the artificial ones [38, 39]. Cubic phases are interesting for the controlled release because they have large surface area of the channels, pore sizes are approximately ~5-10 nm, they can solubilize hydrophobic, hydrophilic and amphiphilic molecules, and they are biodegradable [40].

As drug delivery systems bicontinuous liquid crystalline phases are capable to dissolve drugs of different polarities. Also they can dissolve drugs at various concentration: from extremely low to high. Interwoven channels enable cubic phases to incorporate drugs of different size and quantity. For example, hydrophilic drugs can be dissolved first in water and then this solution can be used for cubosomes' preparation and, vice versa, hydrophobic drugs can be dissolved in lipids as glyceryl monooleate (GMO) or monoolein (MO) and then this solution can participate in the formation of the cubosomes.

If we take GMO as the surfactant for preparation bicontinuous liquid crystalline phase, we will observe that this surfactant may be used to create cubosome containing from 55% to 89% of water and 15-45% of GMO. A wide variety of drugs can be accumulated in the cubic phase. Bicontinuous liquid crystalline phase are excellent carriers for drugs [41-50], but they also have disadvantages: drugs can ruin the lattice structure of the bicontinuous liquid crystalline phase also 'big' drug cannot penetrate inside the channels. One of the simplest mechanism of the drug release is controlled by pH oleic acid-containing cubosomes can change the symmetry from cubic to hexagonal [51, 52].

Although cubic phases exhibit high potential for the drug delivery no commercial applications of these phases as drug delivery vehicles are known. Partially, it can be explained by the extremely high viscosity of the bulk cubic phases. For this reason it is better to use cubosomes as the delivery vehicles because of their lower water-like viscosity. Certainly, there are other drug containers and carriers known in chemistry like for example vesicles and liposomes.

Cubosomes can incorporate not only drugs but they can also be used to transport DNA-lipid complexes to the tumor cells for example. There are a lot of works where DNA-lipid complexes in the form of liposomes are used for targeting the tumor cells. In the future cubosomes may be used in a similar way [53].

Cubosomes can have an influence on the structure of the encapsulated molecule as well as the encapsulated molecule can have an influence on the structure of the cubosomes. In the recent work of Angelova [54] the formation of the 'proteocubosomes' which have tertiary structures and consist of ordered and disoredered cubosomes were investigated. The proteocubosomes can be formed only from the bulk cubic phase with the help of the incorporated proteins.

Since cubosomes have regular structure their application in the field of material synthesis can also be interesting. The creation of particles with nanostructure opens the road to the application of the

cubosomes in electronics, photonics, catalysis, and medicine. Cubic phases can be used as matrices for protein encapsulation or the reaction of synthesis or polymerization. For example, aluminosilicate zeolite MCM-48 is formed in cubic phases [54]. Cubosomes may be important for pharmaceutical industry in the nearest future.

The possibility of potentially many applications of cubosomes in medicine motivated our investigations of these substances.

II. Experimental part. Investigation of the phase diagrams

We intend to study cubosomes (Fig. 7), very small particles of liquid crystalline cubic phases dispersed in water [55, 56]. Cubosomes can be prepared only with surfactants such as phytantriol, monoolein or C12EO2. The solutions of these surfactants with water are characterized by a solubility gap. In such solutions cubic phases coexist with the inverted micellar phase composed of almost pure water.
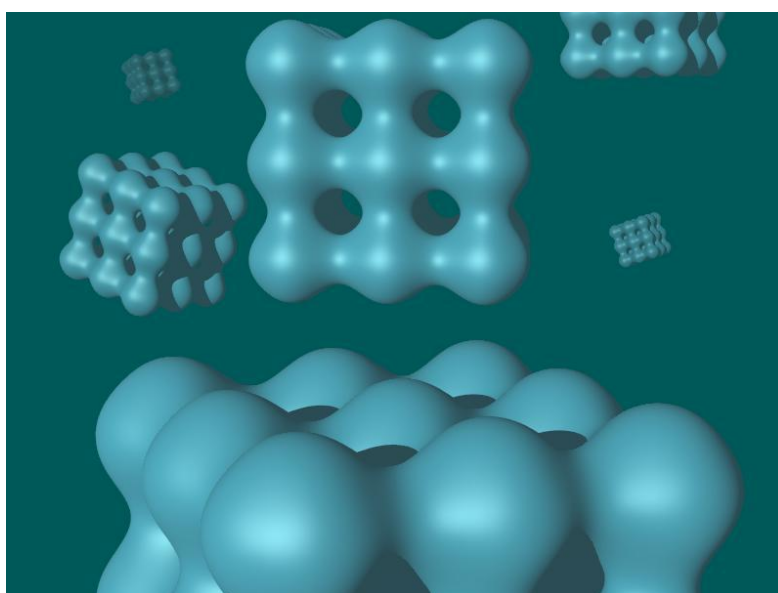
Fig. 7. Schematic illustration of cubosomes – nanoparticles of cubic lyotropic phases dispersed in water.

Our program of experimental investigations of cubosomes consists of two parts. The first part, which will form the basis for the second part, is devoted to the study of phase diagrams of lyotropic systems suitable for preparation of cubosomes. The phase diagrams of such systems are very complex. They contain many different phases such as (L2) an inverted micellar phase; (L1) a direct micellar phase; (L3) a sponge phase; (Lα) a lamellar phase; (Pn3m) a diamond cubic phase; (Im3m) a primitive cubic phase. The second part deals with the preparation of cubosomes and with investigation of cubosomes by means of an electron cryo-microscope.

The preparation of cubosomes involves evolution of ternary or quaternary mixtures along well defined trajectories in their Temperature-vs-Concentrations phase diagrams. Having at our disposal a large amount of phytantriol from a pharmaceutical source [Laserson Chimie, free sample offered by Mme Sylvie Messager], we decided to prepare cubosomes from mixtures of this surfactant with water and ethanol. For this reason we must know all the details of phase diagrams of the ternary phytantriol/water/ethanol and quaternary phytantriol/water/ethanol/DSPG (DSPG is 1,2-Distearoyl-sn-glycero-3-phosphoglycerol) systems. During experimental studies of phase diagrams we identify all phase transitions which take place in the investigated system either ternary or quaternary. In particular, we observe: 1 - macroscopic monocrystals of cubic phases Pn3m and Im3m, 2 - droplets of isotropic phases L3, L2, and 3 - droplets of the lamellar phase Lα. We will also investigate several out-of-equilibrium effects such as the growth-by-redistribution, the ratchet and the Ludwig-Soret effects.

II.1. On the necessity to work with a ternary system

Cubosomes can be prepared only from mixtures of water and surfactants characterized by a solubility gap. Among such surfactants, C12EO2 has been probably the most extensively studied; its phase diagram Temperature-vs-Concentration of water is well known (see Fig. 7) [57]. Unfortunately, the C12EO2/water system has a drawback: as shown in Fig. 8, the temperature range of its Pn3m/L1 phase coexistence domain is very narrow $\approx$3°C.
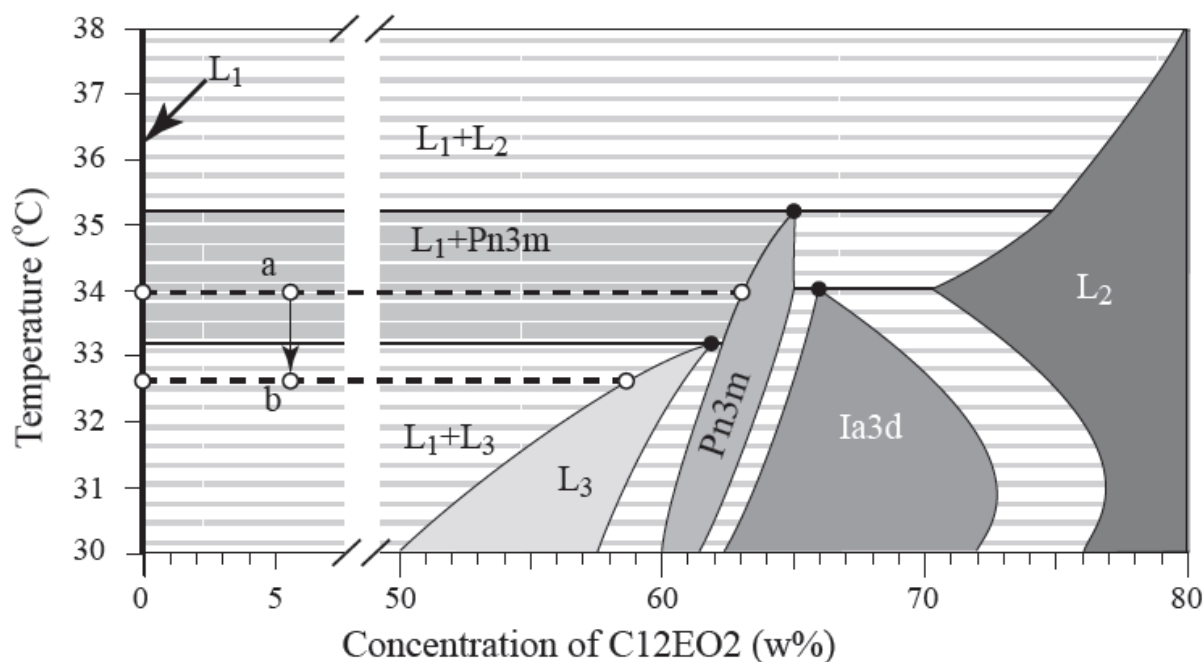
Fig. 8. Phase diagram of the C12EO2/water mixture established by Lynch and all [57]. The limits of the micellar L1 phase drawn with dashed lines are hypothetical. The presence of three peritectic points corresponding to the upper temperature limits of the L3, Pn3m and Ia3d phases can be seen. Cubosomes occurs only in the domain of coexistence L1+Pn3m.

The required phase coexistence Pn3m-in-L1 is known to occur also in aqueous solutions of phytantriol. Indeed, the phase diagram of phytantriol established by Barauskas and Landh [41] and shown here in Fig. 9 displays the Pn3m/L1 phase coexistence, like the one of the C12EO2/water mixture shown in Fig. 8, yet with a much wider temperature range. (Let us emphasize that this feature is suitable for studies of the Ludwig-Soret effect, see section II.3.1). The detailed structure of the phase diagram of phytantriol indicate some drawbacks for preparation of cubosomes. Due to the presence of the Pn3m/H/L2 triple point, in experiments performed with excess of water, Pn3m-in-L1 crystals can only be grown from anisotropic H-in-L1 droplets contrary to the case of the C12EO2/water system where Pn3m-in-L1 monocrystals were grown from isotropic L2-in-L1 or L3-in-L1 droplets (see Fig. 8). As a consequence, well oriented monocrystals of the Pn3m phase are difficult to obtain.
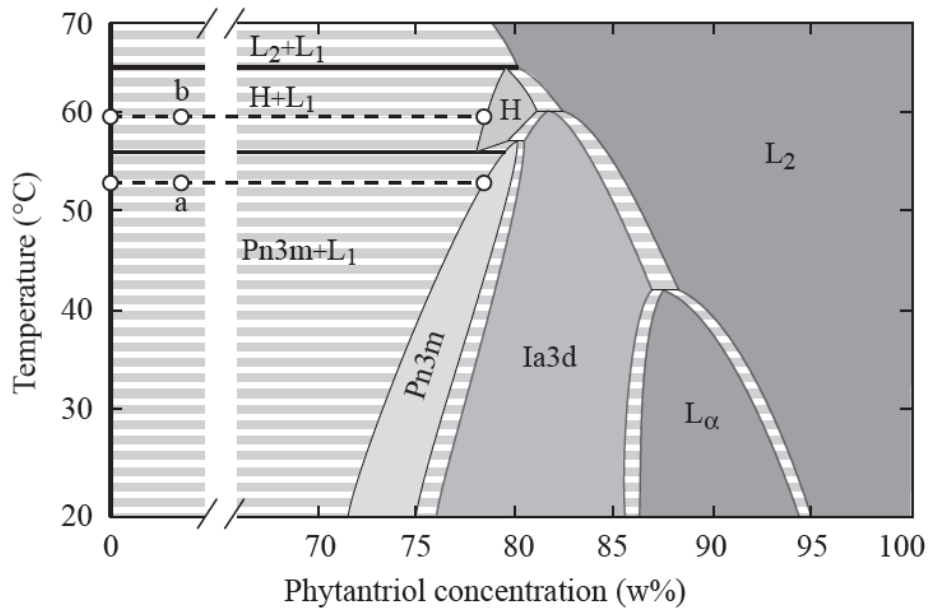
Fig. 9. Phase diagram of the phytantriol/water binary system. (Modification of the phase diagram established by Barauskas and Landh [58]. Collaboration of P. Faye and J. Okal).

Anticipating the results of the systematic study of the phase behavior of the phytantriol/water/ethanol ternary system, we show below in Fig. 10 its phase diagram.
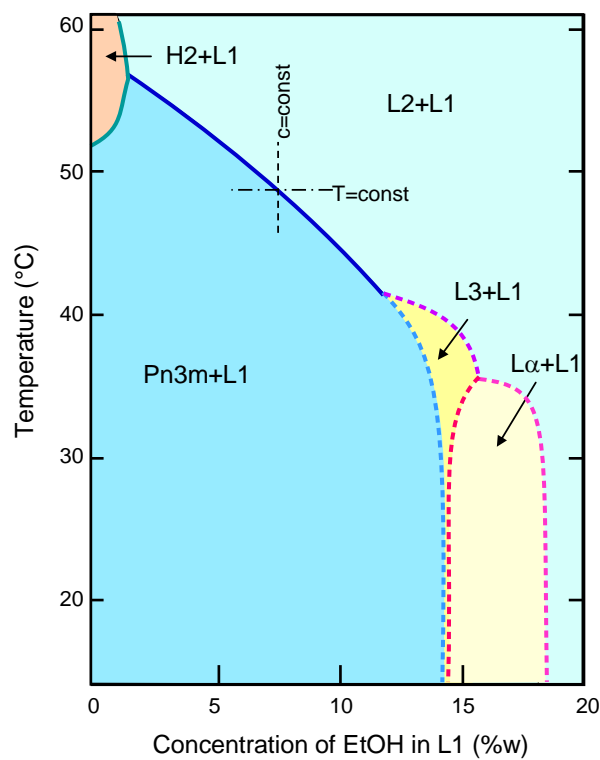
Fig. 10. Phase diagram of the phytatriol/water/ethanol system.

23

It is obvious that at large enough concentrations of ethanol in the L1 phase, Pn3m-in-L1 crystals can be melted into L2-in-L1 droplets and subsequently recrystallized again as required. More precisely, in the ternary phytantriol/water/ethanol system, the L2+L1 → Pn3m+L1 transition can be driven in two ways: 1 - either by adding ethanol to the L1 phase surrounding crystals at T=const (the horizontal path in Fig. 10), or 2 - by increasing the temperature at a constant proper concentration of ethanol in L1 (the vertical path in Fig. 10). In both cases, the concentration of ethanol in the L1 phase has to be adjusted precisely. This can be done in several ways. As we will see in the next section, we decide to use a quite sophisticated system allowing mixing, in variable proportions, of two ethanol-in-water solutions of different concentrations.

II.2. Description of the experiment

II.2.1. Determination of the upper limit of the solubility gap

The main feature of the binary phytantriol/water system is the solubility gap. In the context of our work (Fig. 14) it means that when a droplet of phytantriol is surrounded by pure water flowing through the capillary, it will not dissolve but its structure depends on temperature. On the other hand we know that phytantriol and ethanol taken alone are fully soluble at any concentrations. Therefore one can ask:

- How the phytantriol/water solubility gap evolves when ethanol is added to water and
- What are structural changes in the sample during this evolution?

Alternatively, one can ask

- How the solubility of phytantriol with ethanol is broken upon the action of water added to phytantriol/ethanol solution?

Most of our observations performed with the experimental setup shown in Fig. 14 are related to the first two questions. However, we will answer the third question with the aim to determine the upper limit of the ethanol-in-water concentration above which the sample is dissolved.

For this purpose we prepared in test tubes a series of eleven phytantriol-in-ethanol solutions with concentrations of phytantriol ranging from 5 to 80% (w) (see Fig. 11). On the isothermal section (at room temperature) of the phase diagram shown in Fig. 12 these isotropic solutions are represented by white circles located on the Ethanol-Phytantriol side of the Gibbs triangle. Subsequently, water was added drop-by-drop to these solutions. After each drop, solutions were homogenized by a gentle stirring.
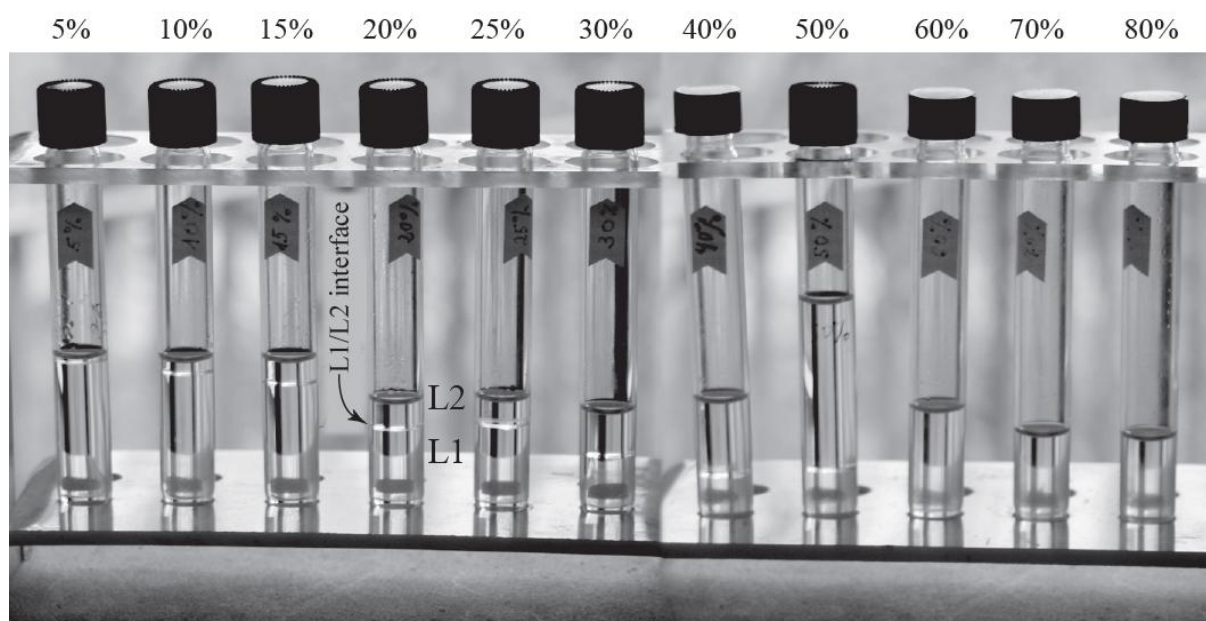
Fig. 11. Determination of the upper limit of the solubility gap in the phytantriol/water/ethanol ternary system at room temperature.

Let us consider as an example the 20% solution represented by a bigger circle. When water is added progressively to the solution that the composition evolves in the Gibbs triangle along the dashed line toward the "Water" corner. As long as the sample stays transparent, it remains in the monophasic domain L2. However, after the addition of an ultimate drop, the upper limit of the miscibility gap is crossed and the sample becomes milky because droplets of the water-rich phase L1 nucleates in the L2 phase. The sample remains milky as long as it is stirred. However, when stirring is stopped, the L1 droplets sediment, coalesce and finally form a transparent layer separated from the supernatant L2 phase by a well visible interface (Fig. 12). On the Gibbs triangle, this transition from the monophasic L2 domain to the biphasic L2+L1 one is represented by the gray circle.

All eleven samples (see Fig. 11) ware tested in this way and as a result the L2/L2+L1 boundary was determined. Extrapolated to the Water-Ethanol side of the Gibbs triangle it seems to cross it at 40%.
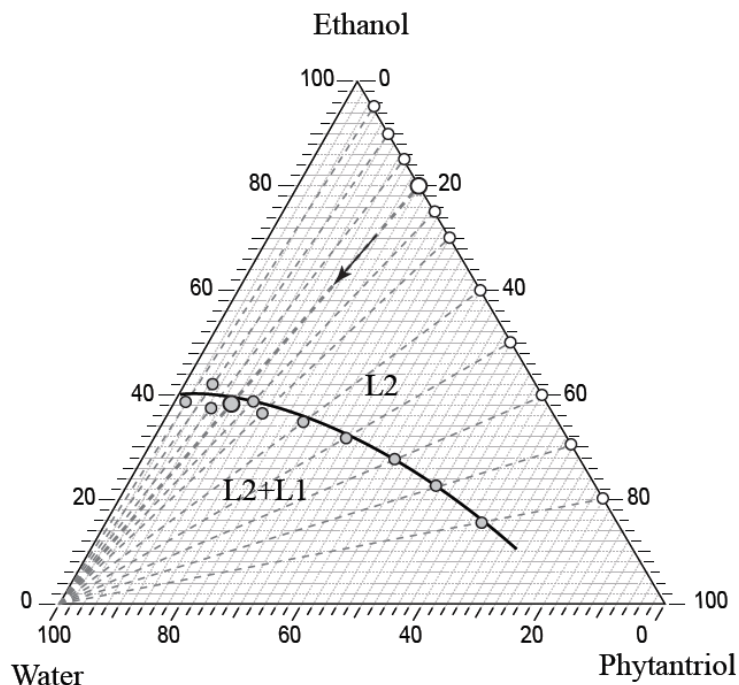
Fig. 12. Determination of the upper limit of the solubility gap in the phytantriol/water/ethanol ternary system at room temperature.

II.2.2. Relevant part of the phase diagram

From the phase diagram of the binary phytantriol water system shown in Fig. 11 we know also the immediate vicinity of the water-phytantriol side of the Gibbs triangle. As it is shown in Fig. 13, monophasic domains Pn3m, Ia3d, L1 and L2 must start there. It remains to find how far do they extend in the "ethanol" direction. With the experimental setup described in section II.2.3, tailored for the study of shapes of Pn3m-in L1 crystals, we will be able to explore only the domain of coexistence between the L1 phase, confined to the interval [0,40]% of the "water-ethanol" side of the Gibbs triangle, and mesophases at the left extremity of the area indicated as T.I. (terra incognita) in Fig. 13. We know already from Fig. 9 that when the L1 phase is composed of pure water it coexists with the Pn3m phase. We

know also that at upper extremity of the coexistence domain the Pn3m crystals must finally be replaced by droplets of the L2 phase. However, the expected direct transition

$$Pn3m + L1 \Rightarrow L2 + L1 \qquad (II.1)$$

driven by increasing concentration of ethanol occurs only at temperatures higher than 42°C. As we will see below, at lower temperatures, more complex sequences of phase transitions occur:

$$Pn3m + L1 \Leftrightarrow L3 + L1 \Leftrightarrow L2 + L1 \qquad (II.2)$$

or even:

$$Pn3m + L1 \Leftrightarrow L3 + L1 \Leftrightarrow L\alpha + L1 \Leftrightarrow L2 + L1 \qquad (II.3)$$
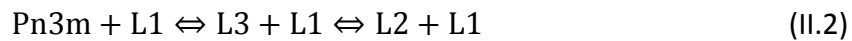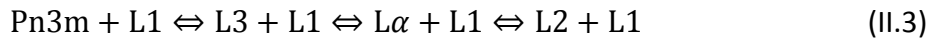
For the purpose of the forthcoming discussion of the method of preparation of samples let us note that at room temperature the L2+L1 coexistence is reached when the concentration of ethanol in the L1 phase is higher than 18%.
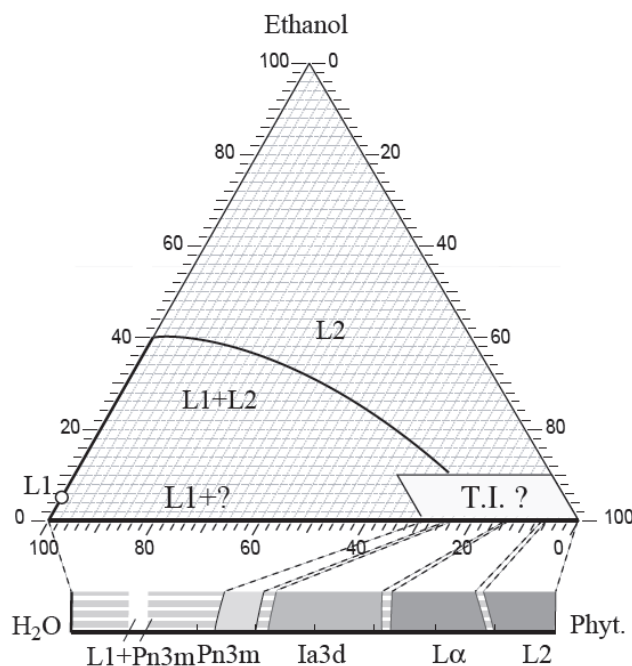
Fig. 13. Definition of the area on the PWE phase diagram pertinent for the the study of faceting. The phase sequence on the Water-Phytantriol axis is known from the phase diagram in Fig. 9. The upper limit of the L1+L2 coexistence domain is known from Fig. 11 and Fig. 12.

II.2.3. Experimental setup

Our setup is represented schematically in Fig. 14 below. The sample, i.e. a droplet of a surfactant, is situated on the wall of a flat capillary of section 0.2×4 mm shown in Fig. 14a and b. This sample is surrounded by a water/ethanol solution flowing slowly in the capillary. This solution is prepared by mixing two fluxes from two syringes whose pistons are driven by stepping motors. It means that the concentration c_s depends on concentrations c_1 and c_2 of the solutions contained by syringes as well as on angular velocities ω_1 and ω_2 of the stepping motors:

$$c_s = \frac{\omega_1 c_1 + \omega_2 c_2}{\omega_1 + \omega_2} \qquad\qquad (II.4)$$

In this setup flows are laminar so that the mixing process of the two fluxes is purely diffusive. It occurs between the "T" shaped connector and the sample. The major part of this section is made of a flexible tube of internal diameter $\emptyset$ = 1mm and having the length L=10cm. With the typical diffusivity of ethanol in water D ≈ 10^{-9}m^2/sec, one gets the characteristic time

$$\tau \approx \frac{\emptyset^2}{4\pi^2 D} \approx 30 sec \qquad\qquad (II.5)$$

In order to allow the mixing process to occur, the flow velocity in the flexible tube must be smaller than $\vartheta = 3mm/sec$. This requirement is satisfied when $\omega_1 + \omega_2$ is small enough, that is-to-say, $\omega_1 + \omega_2 \leq \omega_{max}$.

The mean concentration c of ethanol in the solution flowing through the capillary must be lower than 40% because for higher concentrations the sample starts to dissolve in the surrounding solution. This requirement has been always satisfied because all observed phase transition occur at concentrations lower than 20% (see for example Fig. 10).

At a constant total flux, that-is-to-say, when $\omega_1 + \omega_2 = \Omega = const$ so that $\Delta\omega_1 = -\Delta\omega_2 = \Delta\omega$, the precision of regulation of the mean concentration calculated from equation II.4:

$$\Delta c_s = \frac{\Delta \omega (c_1 - c_2)}{\Omega} \tag{II.6}$$

is the best when $c_1 - c_2$ is as small as possible. In practice it means that during the exploration of the phase diagram shown in Fig. 9 concentrations c_1 and c_2 were set in vicinity of triple lines.
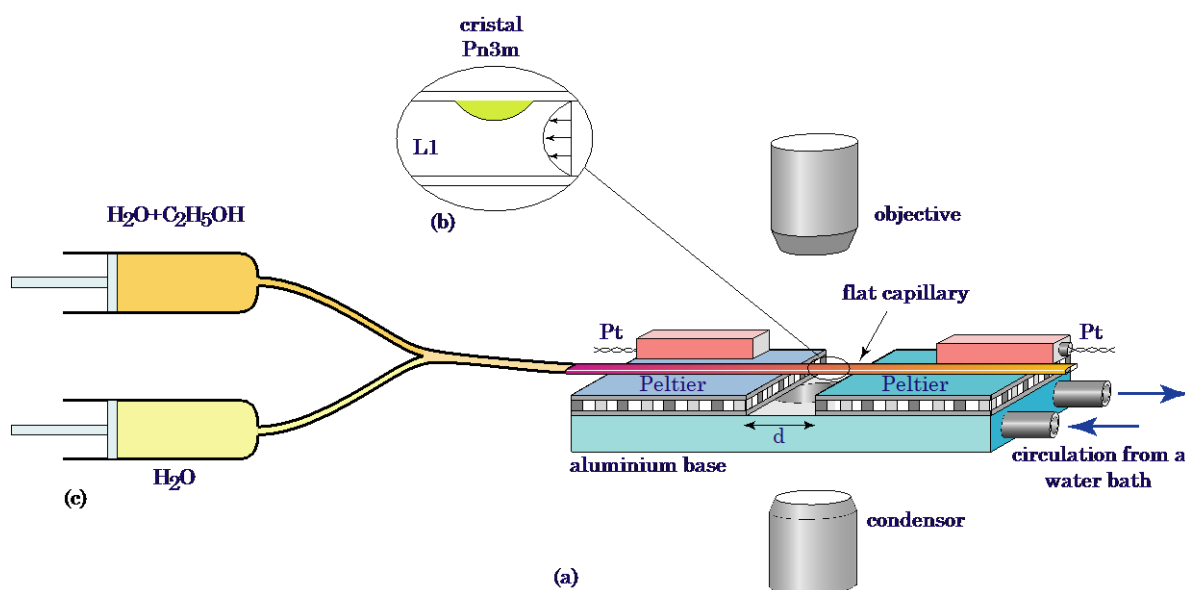
Fig. 14. Experimental setup. The distance d between the Peltier elements can be adjusted. Their temperatures are regulated separately by means of a LabView computer program. The temperature of the metallic base is set by a circulation of water from a thermal bath. The capillary is pressed against the Peltier elements by a plastic foam part not shown in the drawing.

The capillary is placed on two Peltier elements which are in thermal contact with a metallic base. The sample is pressed against the Peltier elements by an insulating plastic part not shown in the Fig. 14. The role of this part is to insure thermal contact of the capillary with the Peltier elements as well as to insulate the capillary from above. The distance d between the Peltier elements can be adjusted between 1 and 7 mm and is usually set to 3 mm.

The observation of the sample is made in transmitted light mode using a simple system consisting of a microscope objective, a video camera and a rudimentary illumination system (lamp+lens) mounted on a vertical bench. Videos of evolving crystal shapes are stored first

29

as files in the computer. Subsequently, ImageJ software is used, for example, to extract arbitrary spatio-temporal sections from the recorded videos.

II.2.3.1. Regulation of the temperature

The regulation of the temperature is achieved in two stages: 1) the temperature of the metallic base is set by means of circulating water from a thermostated bath; 2) the temperatures T1 and T2 of the Peltier elements are regulated by a LabView computer program reading resistances of the Pt probes (from a multiplexed Keithley multimeter) and, after a PID correction, setting the current sent to the Peltier elements via a DAC and a power op-amp. The use of Peltier elements has the advantage of providing a short response time of about 10 s on heating as well as upon cooling. The temperatures T1 and T2 are set with the precision of 0.01K and the stability of the regulation is of the order of 0.001K. The use of the computer in the temperature regulation loop enables easy programming of arbitrary temperature cycles T(t) [59].

II.2.3.2. Temperature cycling

As shown in Fig. 15, one period of the temperature cycling used in our experiments consists of four stages.
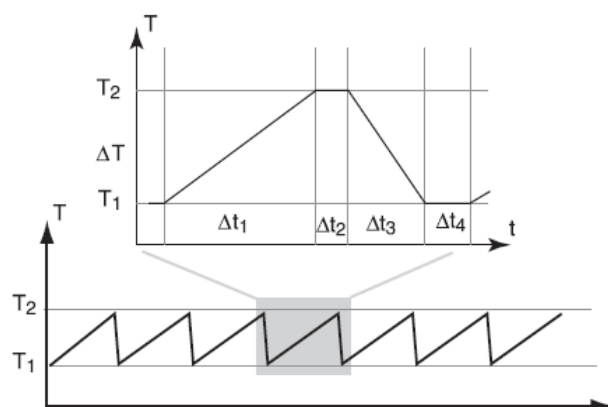
Fig. 15. Shape of the temperature cycling used in experiment.

30

The first one is a positive linear ramp. Its amplitude ΔT is obviously limited by the temperature range of the L1/Pn3m phase coexistence. For this reason, typically, ΔT is smaller than 1K for the C12EO2/water system but can be much larger in experiments with phytantriol. The slope of the ramp $\Delta T/\Delta t_1$ is limited too by the necessity of avoiding nucleation of L1 inclusions (see section II.3.4; II.3.5).

During the second stage of duration Δt_2, the temperature remains constant. The purpose of this stage is to allow the composition of the crystal to recover its equilibrium value and let the growth by redistribution to end. Its typical duration is about 30 s.

The third stage is a negative linear ramp returning the temperature to its lower limit T_1. Its slope can be much steeper than the one of the positive ramp because the undersaturation of water in the crystal has no drastic effects; it shifts the state of the crystal inside the Pn3m monophasic domain.

The purpose of the fourth stage (at constant temperature) is to allow the crystal to swell with water until the chemical equilibrium is restored [60].

II.2.3.3. Control of the ethanol concentration

As mentioned above (Fig. 14), the concentration of ethanol in the solution flowing through the capillary is set by mixing fluxes delivered by two motorized syringes containing aqueous solutions of ethanol of different concentrations. More precisely, pistons of the two syringes are pushed by screws driven by stepping motors. The sense and speed of rotation of the stepping motors are controlled by intermediate of a special purpose interface and by means of a LabView program.

II.2.4. Preparation of the samples

As already mentioned above, among the large variety of lyotropic systems in which occurs a solubility gap, we chose to work with phytantriol because we know well these surfactants

31

from previous studies [29, 36, 59, 60, 61, 62] in these three systems, the Pn3m bicontinuous phase is formed in excess of water.

II.2.4.1. Preparation of samples from a L3-in-L1 emulsion

At the beginning of our study we worked with the C12EO2 nonionic surfactant and prepared our samples from L3-in-L1 emulsions. Our method starts by producing an emulsion of the sponge phase L3 in the micellar phase L1 at room temperature. For this purpose, about 5 ml of water is mixed in a test tube with 0.2 ml of the surfactant. The phase diagram in Fig. 8 shows that in such a sample of average concentration c = 5%, at temperature larger than 21°C, droplets of the initially pure surfactant will absorb water until the sponge phase L3 will fill them. Simultaneously, a negligible amount of surfactant is dissolved in water and the micellar L1 phase is formed. As a consequence, one obtains an emulsion of sponge phase droplets dispersed in the micellar phase L1.
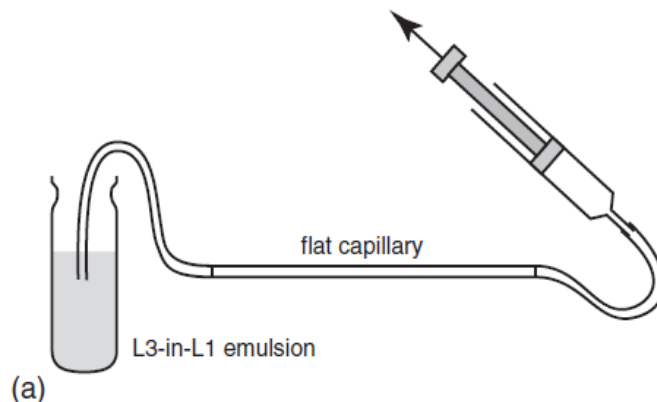
Fig. 16. Preparation of a sample: filling the capillary with the L3-in–L1 emulsion.

The flat capillary is filled with the emulsion by suction using one of the two syringes which are connected to the end of the capillary (Fig. 16). Observation reveals that most of the L3 droplets have a diameter smaller than the thickness of the capillary (see Fig. 17a).

32
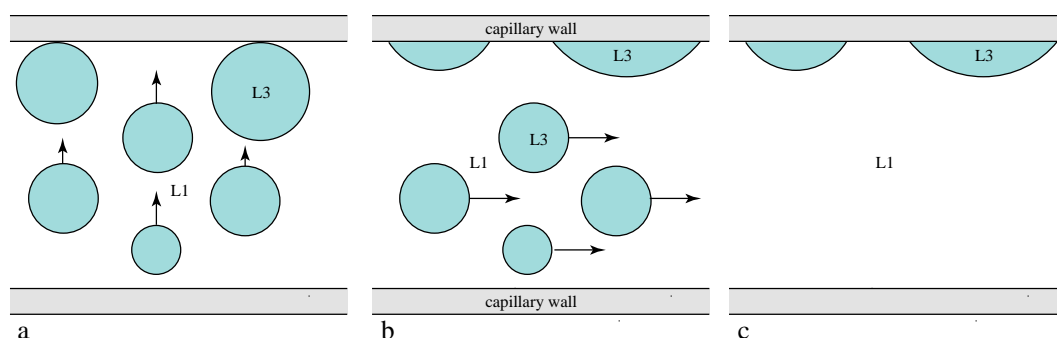
Fig. 17. Evolution of the sample: a) action of buoyancy on L3 droplets, b) partial spreading of L3 droplets on the upper capillary wall, c) after flushing with pure water.

Under the action of the buoyancy force (see Fig. 17a), such small droplets, less dense than water, reach the upper wall of the capillary where they spread partially. These small droplets of the sponge phase are transformed into defectless monocrystals of the Pn3m phase in two stages. First, the temperature is raised to about 37°C into the domain of the coexistence of the L1 and L2 phases so that the droplets of the sponge phase are transformed into droplets of the inverse micellar phase L2. After the second step 2 (see Fig. 10), the sample is cooled below the peritectic triple point L1/Pn3m/L2 so that the droplets of L2 phase are transformed into monocrystals of the Pn3m phase. The main reason for making such a detour, instead of going directly from the L1+L3 to the L1+Pn3m coexistence domain, is that the sponge phase is metastable with respect to the Pn3m phase. The Pn3m crystals obtained by this method are most of the time oriented with their (111) plane parallel to the capillary wall and are always truncated. The contact angle between L1/Pn3m and glass/Pn3m interfaces is about 110°.

II.2.4.2. Preparation of samples by an "*ad hoc*" method

From the structure of the phase diagram of the ternary phytantriol/ethanol/water system (see Fig. 10) it follows that the L3-in-L1 emulsion can be prepared only at temperatures higher than 38°C which is contradictory with the preparation of samples at room temperature detailed in the previous section. For this reason, when working with phytantriol, we used another "*ad hoc*" method presented below.

33

First, we mix phytantriol with about 10% of ethanol with the aim to lower its viscosity. A steel wire of diameter slightly smaller than the capillary's thickness (0.2 mm) is introduced to it as shown in Fig. 18a. By means of a pipette, a small amount of the phytantriol+ethanol solution is introduced by capillarity in the space between the wire and the wall of the capillary (see Fig. 18b).
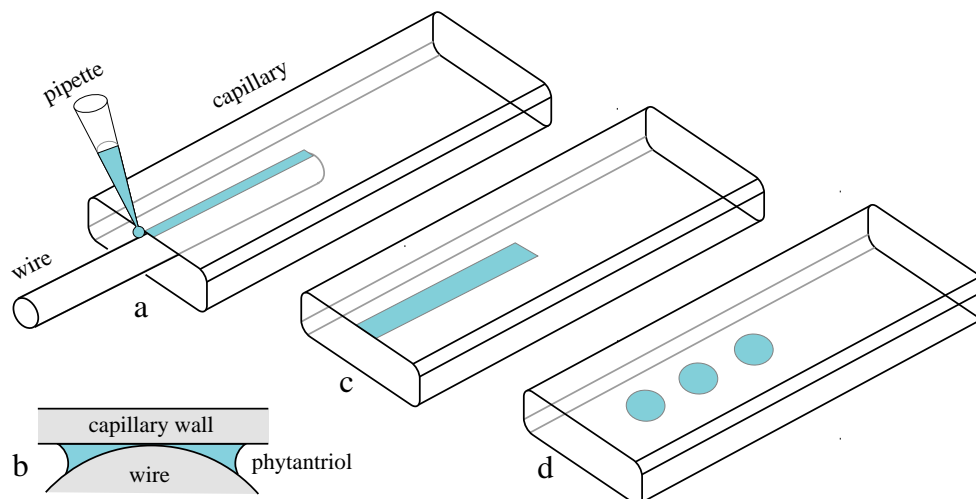
Fig. 18. Preparation of a sample by the "ad hoc" method.

Subsequently, the wire is rapidly pulled out and as a result a track of the phytantriol+ethanol solution remains on the capillary wall (see Fig. 18c). Finally, upon heating, ethanol evaporates which leads to formation of a chain of phytantriol droplets as shown in Fig. 20d. Finally, the capillary is positioned in the setup, connected to syringes and very slowly filled with pure water at room temperature. In agreement with the phase diagram of the phytantriol/water system shown in Fig. 9, the sequence of phase transitions

$$L2 \rightarrow Ia3d \rightarrow Pn3m$$
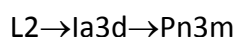
occurs when phytantriol droplets are put in contact with water in excess.

Let us emphasize that Pn3m-in-L1 crystals obtained by this method are polycrystalline and have very irregular shapes. However, their positions in the capillary are easier to control. As explained previously, after repeated melting+recrystallization cycles, that is to say, Pn3m-L2 or Pn3m-L3 transitions, perfect Pn3m monocrystals can be generated.

II.2.5. Results

Our experimental setup allows us to control precisely two parameters: the temperature T and the concentration c of ethanol in the water/ethanol solution flowing through the capillary. When c is lower than 40%, the phytantriol/water/ethanol system remains in its miscilibity gap (see Fig. 12) so that phytantriol does not dissolve in the flowing solution. Moreover, its total mass distributed in small droplets is very small so that the flowing solution acts as an infinite reservoir of water and ethanol. In such conditions the ethanol concentration c can be treated as an intensive parameter like the temperature. For the purpose of clarity, we anticipated the detailed description of the systematic exploration of the miscibility gap and show in Fig. 10 its final result - the T-vs-c phase diagram. It is composed of biphasic domains separated by triphasic lines which meet at quadruple points.

II.2.5.1. Phase transition L2 →Pn3m

As already mentioned in section II.1.2 (see Fig. 10), in the ternary mixture phytantriol/ethanol/water, we can drive the phase transition L2+L1 → Pn3m+L1 either by decreasing the concentration of ethanol in L1 phase or by decreasing the temperature. The series of four images in Fig. 19 illustrates this phase transition occurring upon the change of the ethanol concentration from 12 to 8%, at constant temperature T=43°C.
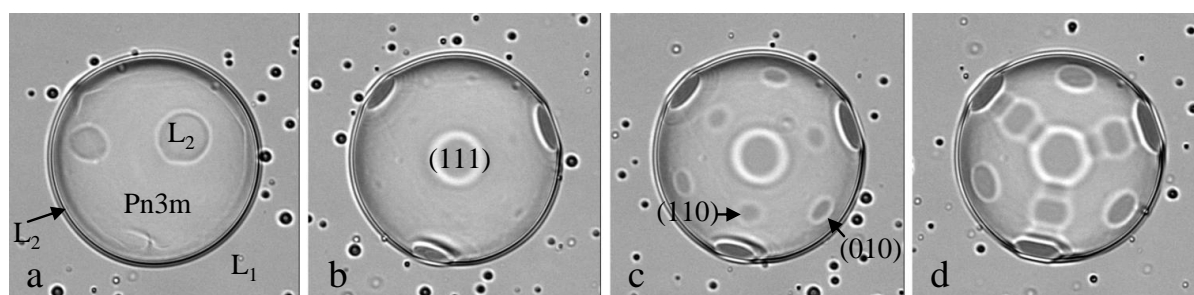
Fig. 19. Phase transition L2+Pn3m+L1 → Pn3m+L1 obtained by decreasing the concentration of ethanol in the L1 phase from 12% to 8% at constant temperature T=43^{0}C.

In these images obtained in non-polarized illumination all visible contrasts are due to differences in the refractive index of optically isotropic phases separated by curved interfaces. In Fig. 19a, three phases are present: the droplet surrounded by the L1 phase is mainly made of the Pn3m phase. The L2 phase forms a thin but well visible layer covering the Pn3m crystal as well as two inclusions. In terms of the Gibbs theory of thermodynamic equilibrium in ternary mixtures, this image could be interpreted as a three-phase coexistence represented in Fig. 20 by the red triangle. In fact, the concentration of ethanol in the L1 phase surrounding the droplet was set to a value slightly larger than that of the L1 vertex of the red triangle (or of the triple line in the phase diagram shown in the inset) so that the Pn3m phase is in fact metastable and actually is melting into the L2 phase. The departure of the ethanol concentration in the L1 phase from its three phase coexistence value being small, this Pn3m $\rightarrow$ L2 melting process is very slow because it involves diffusion of water and its transport through the Pn3m/L2 interface.
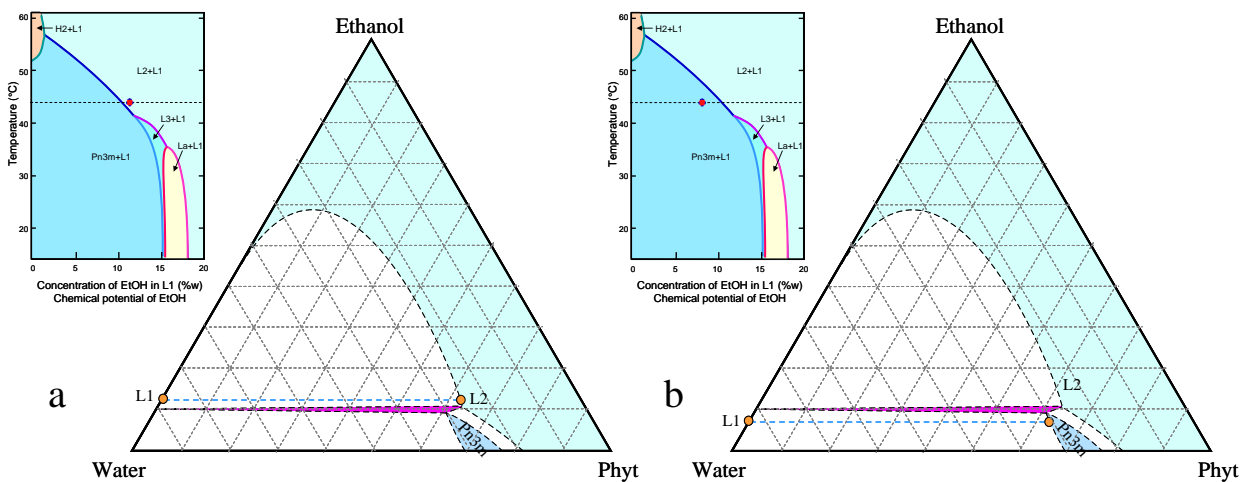
Fig. 20. The transition L2+L1 $\rightarrow$ Pn3m+L1 represented on the Gibbs triangle phase diagram of the ternary mixture phytantriol/ethanol/water (this diagram is simplified and only qualitative): a) coexistence of the inverted micellar phase L2 with the L1 phase practically free of phytantriol, b) upon the change of the ethanol concentration in the L1 phase from 12 to 8% , the three phase coexistence domain (in red) is crossed and the system is driven into the domain of coexistence of the L1 phase with the cubic phase Pn3m.

Remark: In this experiment, we did not allow the Pn3m monocrystal to melt completely with the aim to recover it later. In the contrary case *i.e.* if the Pn3m → L2 melting process went to its end, it would be difficult to recover a well oriented Pn3m monocrystal because the inverse L2→ Pn3m transition is characterized by a considerable hysteresis due the Pn3m-in-L2 nucleation barrier.

After crossing back the L2+L1 → Pn3m+L1 transition line (see the inset in Fig. 20), the L2 inclusions as well as the surface L2 layer recrystallize into the Pn3m phase. As a result, in Fig. 19d we see a Pn3m monocrystal surrounded by the L1 phase. The Pn3m/L1 interface is partially faceted: predominant rough parts of the Pn3m/L1 interface coexist with three types of facets: (111), (100) and (110).

Remark: From 21b to d, facets are growing at the expense of the rough surface. This phenomenon is due to the "growth-by-redistribution" effect which will be discussed later in section II.3.1.

II.2.5.2. Phase transition L2→L3

In another series of experiments the transition L2+L1 → L3+L1 was explored. These experiments begin with the melting of a Pn3m-in-L1 crystal into a L2-in-L1 droplet along the path a → b which is isothermal in Fig. 21. Subsequently, the L2 → L3 transition takes place along the isoplethal path b → c.
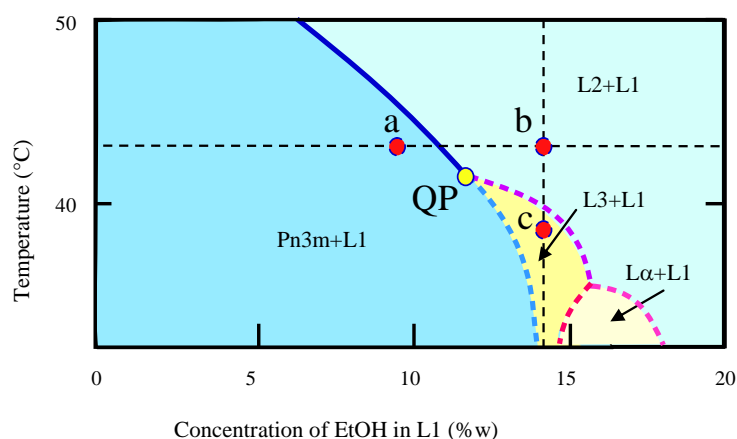
Fig. 21. Along the trajectory a → b → c occurs the sequence of transition Pn3m → L2 → L3.

37

This last transition is illustrated here by the series of six pictures in Fig. 22.
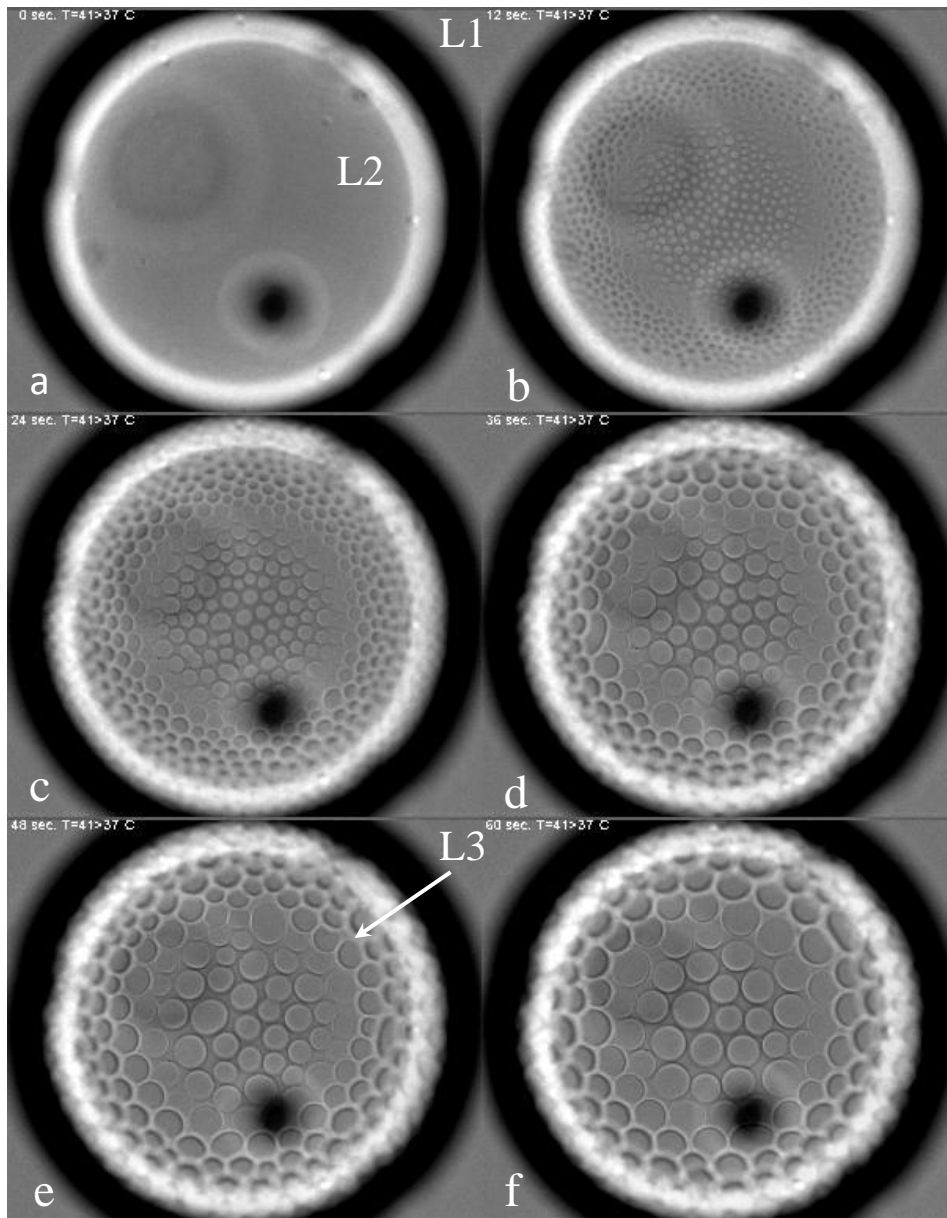
Fig. 22. Phase transition L2 +L1→ L3+L1.

The first image labeled "0 sec" shows a drop of the L2 phase located at the upper wall of the capillary and surrounded by the L1 phase as shown in Fig. 24. The next image shows the nucleation, at the L2/L1 interface, of lens-shaped droplets of the L3 phase (see Fig. 22). On the next four images we see the growth and coalescence of these L3 droplets. At the end of this process, the L2-in-L1 droplet is completely transformed into a L3-in-L1 drop.

Let us stress that this transition is very interesting from fundamental point of view because it involves the coexistence of three isotropic **liquid** phases: L1, L2 and L3. To our knowledge, in all other examples of the coexistence of three isotropic phases, one of them is always gaseous.
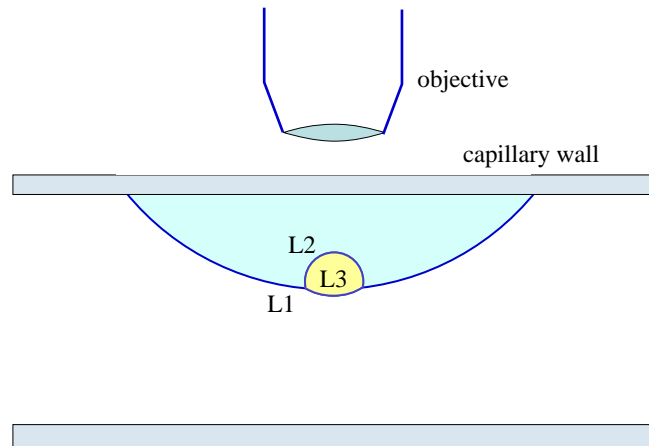
Fig. 23. Geometry of the L2 →L3 transition shown in Fig. 22.

The most striking feature of the L1/L2/L3 phase coexistence shown in Fig. 22 is that the L3 phase appears at the L2/L1 interface not as a macroscopic layer (the critical wetting case) but as a system of lens-shaped droplets. Therefore, we can conclude that the three interfacial tensions γ_{12}, γ_{13} and γ_{23} can be assembled into the so-called Neumann triangle as shown in Fig. 24b below.

$$\gamma_{12} + \gamma_{13}\cos\theta_1 + \gamma_{23}\cos\theta_2 = 0$$
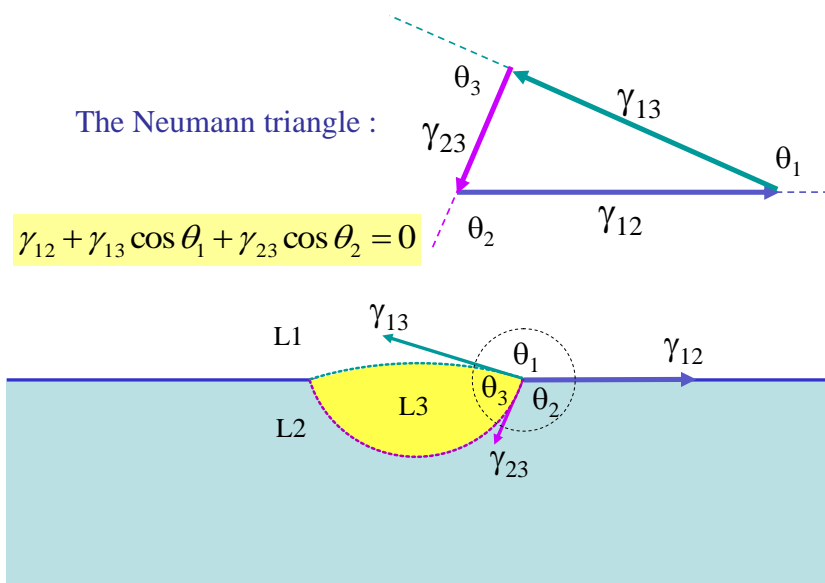
Fig. 24. Condition of the mechanical equilibrium at the L1/L2/L3 triple line.

Let us suppose that, in the first approximation, the interfacial tensions are proportional to differences in densities of adjacent phases. In such a case, γ_{23} should be much smaller than γ_{12} and γ_{13}. For the same reason, γ_{13} should be slightly smaller than γ_{12}. We end up with the asymmetric lens-like shape of the L3 interfacial droplet shown in Fig. 23.
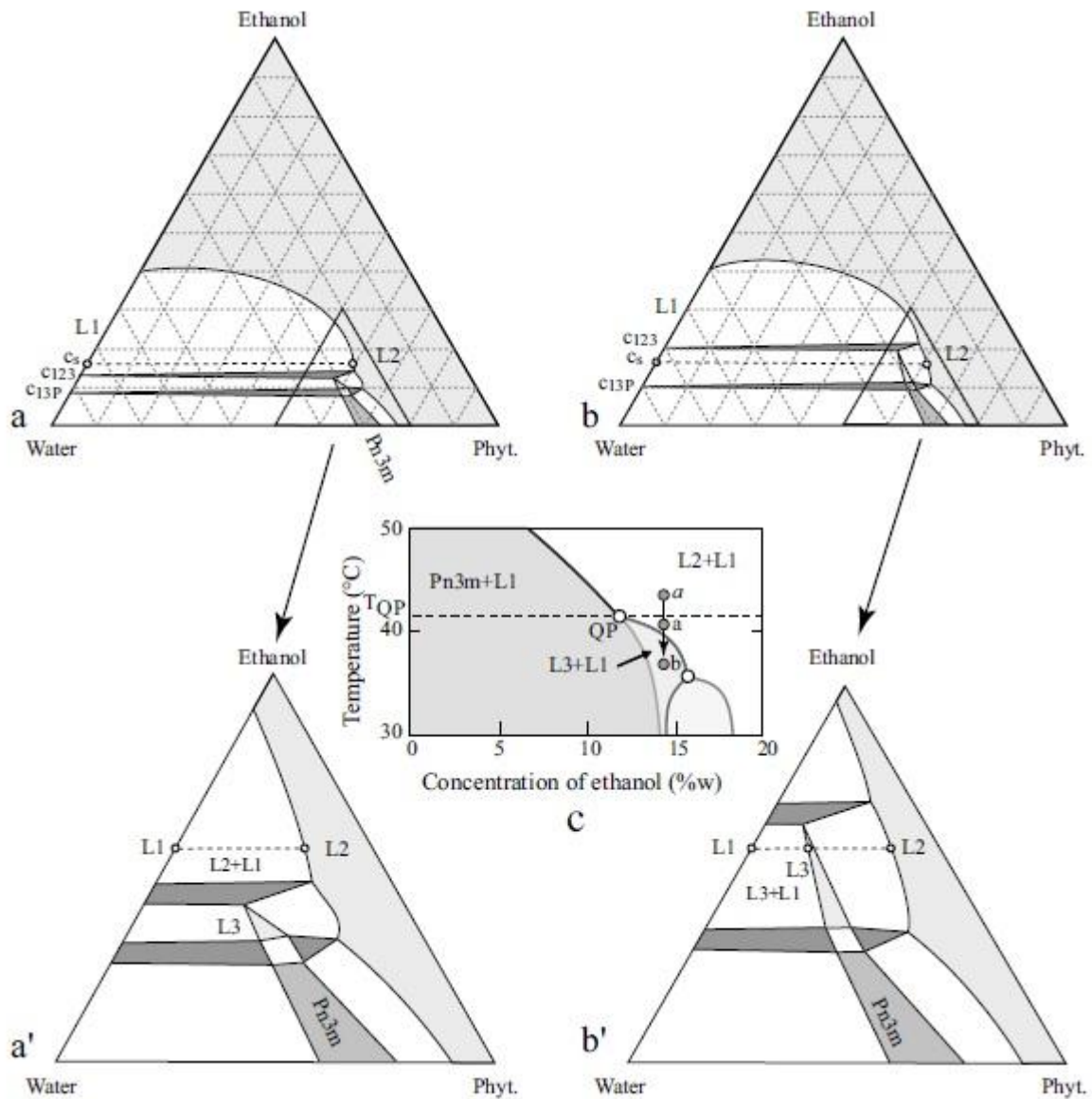
Fig. 25. L2+L1 $\rightarrow$ L3+L1 transition: a and b) simplified topologies of the Gibbs triangle at T=41°C and 37°C, c) the isoplethal path a $\rightarrow$ b on the T-vs-cEtOH phase diagram, a' and b') blow-up of the pertinent area of the Gibbs triangle.

From the observation of the L2 $\rightarrow$ L3 isoplethal (c_s = const) transition we can infer new structural details of the ternary phase diagram. For the purpose of simplicity, we will

suppose first that the initial temperature of the sample in the state of L2+L1 phase coexistence is lower than T_{QP} - the temperature of the quadruple point Pn3m+L1+L2+L3. In such a case, in the Gibbs triangle shown in Figs. 25a and a', the domain of the L3 phase is already present. It is located between three dark triangles representing three-phase coexistence domains: L1+L2+L3, L1+L2+Pn3m and L2+L3+Pn3m.

In this figure the concentration of ethanol c_{123} at the L1 corner of the L1+L2+L3 triangle is lower than the one of the sample c_s (white circle on the Water-Ethanol axis) so that the state of the sample is biphasic L1+L2. When the temperature is lowered, the L1+L2+L3 triangle moves up and the concentration c_{123} becomes larger than c_s (see Figs. 27b and b'). At the same time, the concentration c_{13P} remains lower that c_{123} so that the state of the sample should be L1+L3.

II.2.5.3. Quadruple point L1+L2+L3+Pn3m

The upper limit of the sponge phase L3 in the phase diagram in Fig. 21 (or in Fig. 26c) is given by the temperature T_{QP} of the quadruple point QP where three-phase coexistence lines meet.

In the Gibbs theory of ternary mixtures [36], this quadruple point is known as the *ternary peritectic point* and corresponds to a peculiar change in the topology of the Gibbs triangle phase diagram detailed in Fig. 26.

For $T > T_{QP}$, the coexistence of the L1+L2+Pn3m phases occurs when the mean composition of the phytantriol/ethanol/water system is located inside the red triangle in Fig. 20. In such a case, compositions of the coexisting phases are given by vertices of the red triangle.

At $T = T_{QP}$ (see Fig. 26a), the composition of the fourth phase – L3 – is given precisely by the position of the point L3 which appears inside the L1/L2/Pn3m triangle. For $T < T_{QP}$ (see Fig. 28b), this triangular three-phase domain splits into three three-phase triangles. Simultaneously, the L3 point from Fig. 26a is transformed into the monophasic domain of L3 phase.

41
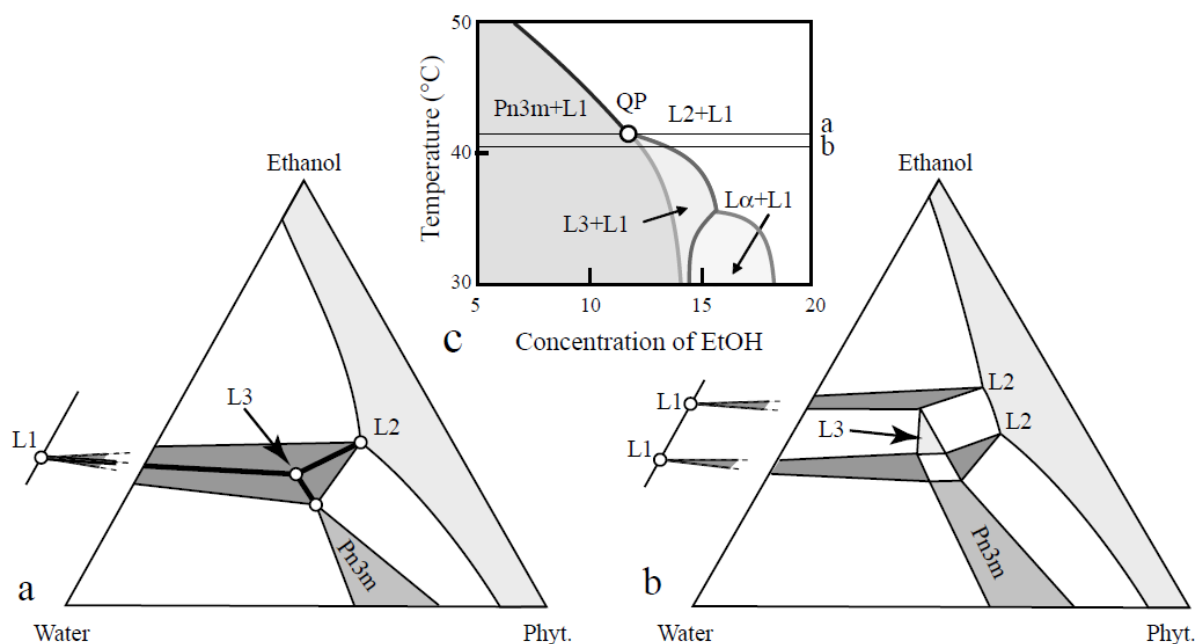
Fig. 26. Interpretation of the quadruple point (QP in d) in terms of the Gibbs theory of ternary mixtures.

II.2.5.4. Phase transitions Pn3m→L3→Lα→L2

To obtain the phase transition Pn3m-L3 we fixed the temperature at 36^0C and progressively increased the concentration of ethanol. Let us remind that our experimental setup with two syringes allow us to increase the concentration of ethanol progressively by varying fluxes delivered by the two syringes (see Fig. 14). So at the temperature of 36^0C the phase transition Pn3m→L3 takes place at the concentration of 12% of ethanol (Fig. 10).

To obtain the lamellar phase Lα we should pass through the phase L3 the temperatures lower than 43^0C (Fig. 10). So we continued to increase the concentration of ethanol, while we had obtained L3 phase. In order to detect Lα phase we have used the polarized illumination.

In the Fig. 27a there is a coexistence of 2 phases Pn3m and L1, where Pn3m phase contains inclusions of L1 phase inside. The crystal of the Pn3m phase is well faceted. While we were increasing the concentration of ethanol facets started to disappear and we obtained the phase transition Pn3m to L3 (Fig. 27d), but at the same time around the L1-in-L3 inclusions the nucleation of Lα phase took place. Rounds circles around the inclusions indicate the

presence of Lα phase (Fig. 27e). On the next pictures we can see the formation of the Lα phase from L3 phase (Fig. 27f, g, h, i).
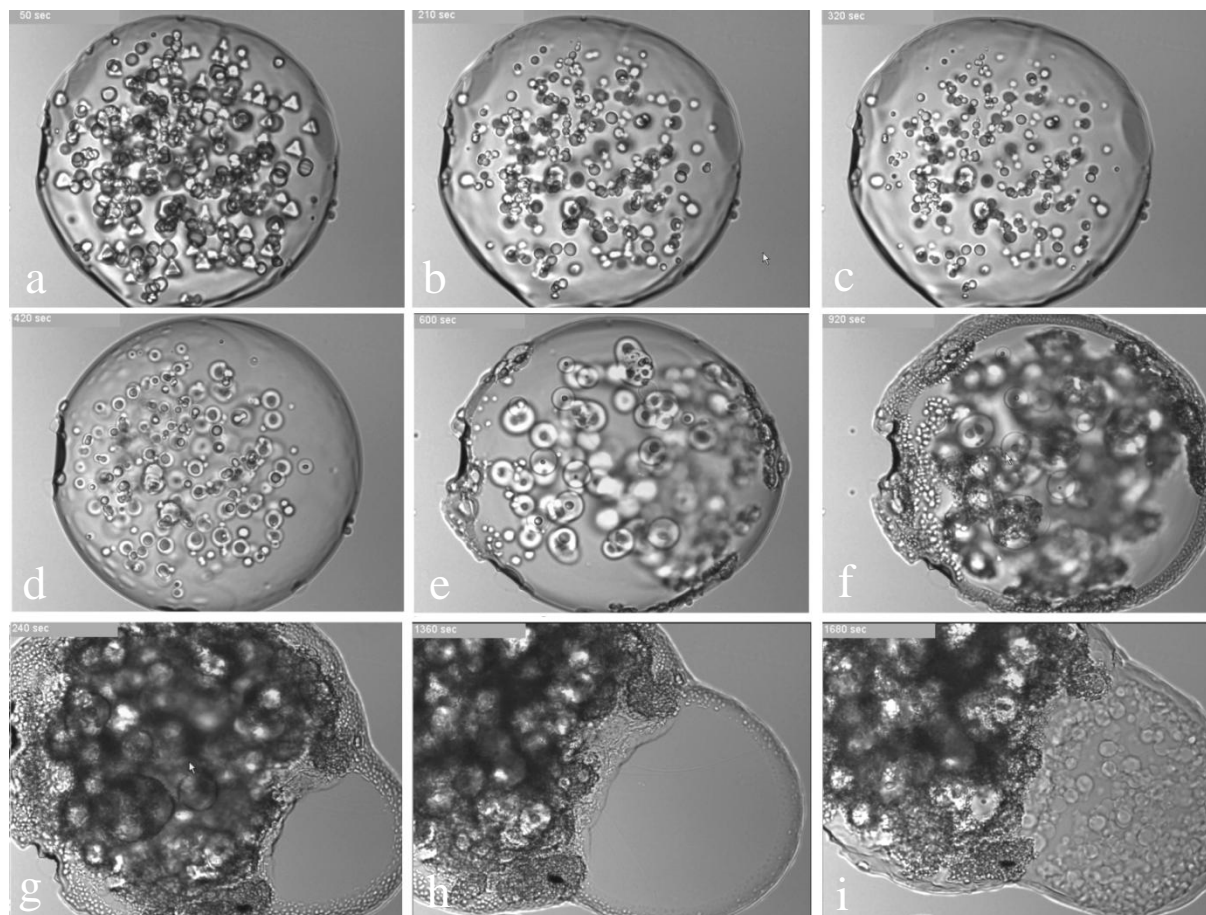
Fig. 27. The sequence of phase transition Pn3m→L3→Lα generated by slow changes of concentration of ethanol (in L1 phase) from 12% to 15% at the temperature 36ºC.

II.2.5.5. Phase transition Pn3m-H

In the phase diagram of Fig. 10 (see also Fig. 28), the line of the three-phase coexistence L1+L2+Pn3m extends between two quadruple points. The lower one L1+L2+L3+Pn3m has been discussed in the previous section. In the vicinity of the upper one, L1+L2+H+Pn3m, upon small changes of the ethanol concentration (along the dashed line) the cubic phase Pn3m can be melted either into the isotropic L2 phase (as discussed previously) or transformed the hexagonal phase.

43

We illustrate this property in Fig. 28 by the series of four images which were recorded at T=54°C upon lowering of ethanol concentration from 4% to 0%.
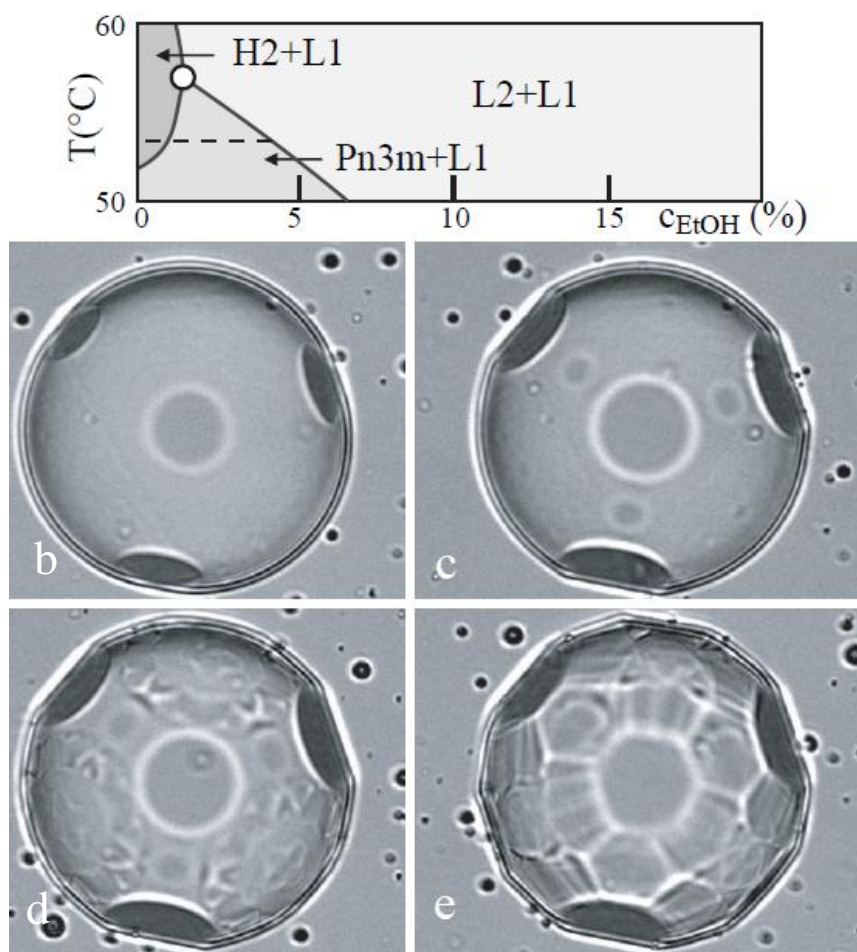
Fig. 28. Phenomena observed at 54°C upon lowering of the ethanol concentration in water: a) the pertinent part of the phase diagram from Fig.12, b) at c=4% only (111)-type facets appear at the Pn3m/L1 interface, c) birth of (202)- and (200)- type facets, d) nucleation of the hexagonal phase, e) growth of the hexagonal phase.

The first image of the Pn3m single crystal (b) was taken at the concentration of about 4% that is to say in the vicinity of the $Pn3m + L1 \Rightarrow L2 + L1$ transition. For this reason, only the (111)-type facets are present at the Pn3m/L1 interface.

On the second image (c) taken at smaller concentration c, (202)- and (200)-type facets appear. The last two images (d) and (e) show that after crossing the $Pn3m + L1 \Rightarrow H + L1$ transition line, the hexagonal phase nucleates on the crystal surface and grows.

For the precise detection of the phase transition Pn3m-H2 we have used the illumination of the polarized light. The face transition from Pn3m to H phase is shown in Fig. 29 more precisely. In fact, Fig. 29 is the full version of the Fig. 10.
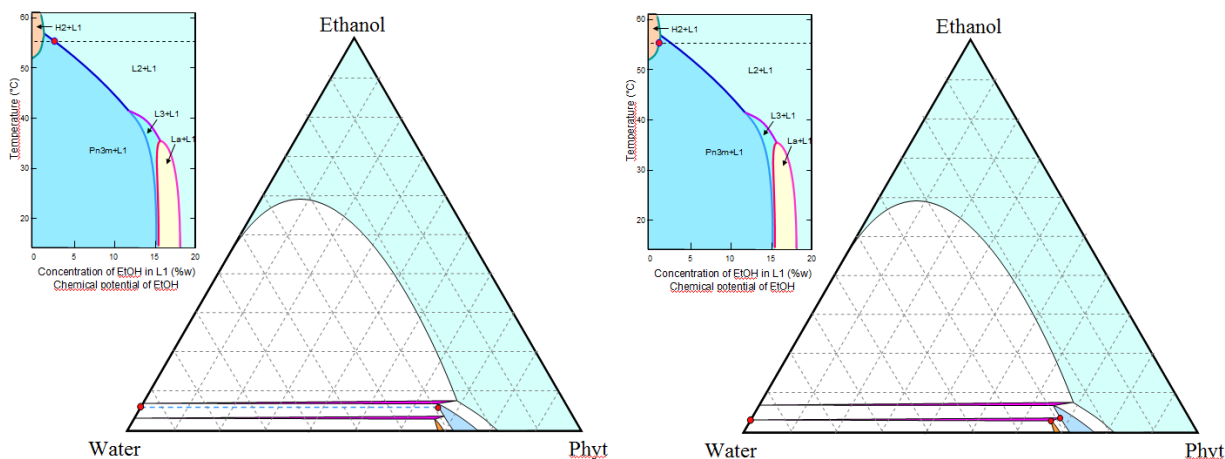
Fig. 29. The phase diagrams: a. the coexistence of three phases Pn3m-L1-L2; b. the coexistence of two phases Pn3m-L1-H2.

II.2.5.6. Phase transition Im3m→L3

We can observe the phase transition Im3m-L3 as well as Pn3m-L3. For this reason the only thing we have to add to the system is the fourth component – 1,2-Distearoyl-sn-glycero-3-phosphoglycerol, sodium salt (DSPG). Adding DSPG to the system leads to forming the new domain between Pn3m and L2 phases. This domain corresponds to the Im3m phase. In Fig. 30a-d one can see the crystal of Im3m phase oriented with its (001) facet parallel to the capillary wall, which was obtained under the concentration of ethanol equal 12% and the temperature equal 32°C.

While we increased the concentration of ethanol, the facets of Im3m crystal started to disappear (Fig. 30b). Subsequently, the facets (100) and (010) disappeared and on the surface of the crystal a thin layer of L3 phase started to be visible. We can risk to suppose that in this case the phase transition Im3m-L3 but not Im3m-L2 takes place, because under the increasing the concentration of ethanol either Pn3m phase or Im3m phase for the temperatures 20-40^{0}C are transformed into the L3 phase (II.2.5.4).
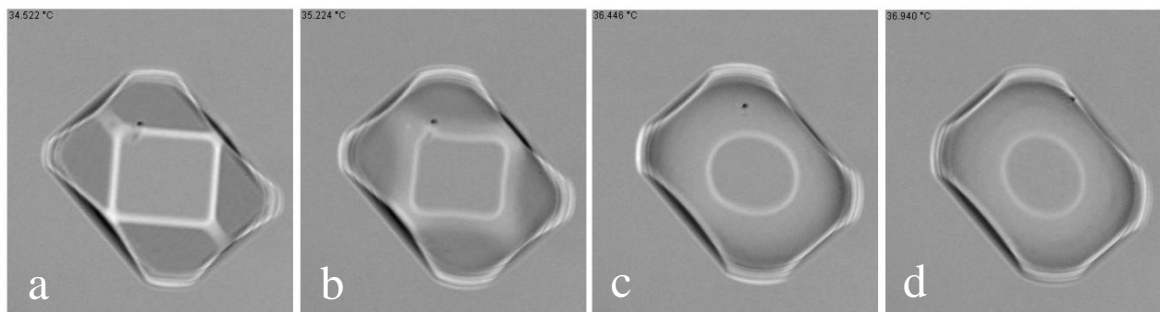
Fig. 30. Phase transition Im3m-L3 by increasing the concentration of ethanol from 12% to 14% at 32^{0}C.

II.2.5.7. Phase transition Pn3m→Im3m

In order to obtain the phase transition Pn3m-Im3m we used a four component system which contains phytantriol/water/ethanol/DSPG. Using the tentative phase diagram we have obtained Im3m phase under 12 % of ethanol and 35°C (Fig. 31a-c).
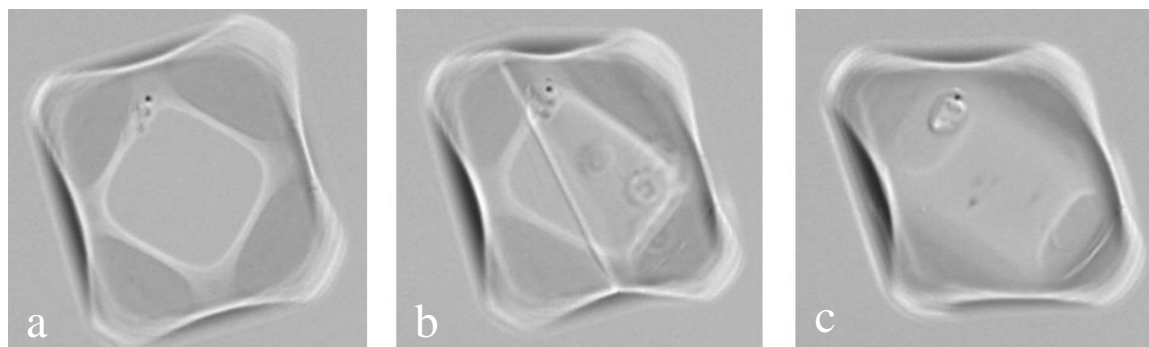
Fig. 31. Phase transition Im3m-Pn3m by increasing the concentration of etanol from 8% to 12% at the temperature 35°C.

We also measured the amount of the DSPG which was equal to 1.8% in the solution of the phytantriol. But it still remains to be answered whether all the amount of DSPG is used to create Im3m phase, because some of it can be washed out from the capillary. And we can't exactly say what is the amount of DSPG in the crystal. Some amount of DSPG is wasted to create the vesicles that are washed out from the capillary in order to clean the sample's surroundings.

II.3 Discussions

II.3.1. Growth by redistribution

Upon the changes in physicochemical conditions, i.e. the augmentation of the temperature T or lowering the humidity, facets of Pn3m in L1 crystal extend their size while the rough parts of crystal surfaces are shrinking.

This phenomenon has no counterpart in usual crystal/melt or crystal/solution system because it occurs at a constant number N_s of surfactant molecules in Pn3m and Ia3d crystals. Called "pseudo-growth" or "growth by redistribution", it is a characteristic of truly liquid-crystalline cubic lyotropic structures in which the number of surfactant (or water) molecules per unit cell can vary continuously as a functions of T and/or h. If, for instance, the number of surfactant molecules per unit cell n_{uc} decreases upon the changes in temperature T and humidity h mentioned above, then, at constant N_s, new unit cells have to be created as if crystals were growing [30].

Now, in the case when facets are metastable i.e. when nucleation is prohibited on facets, the growth (in terms of the total number of unit cells $N_{uc}=N_s/n_{uc}$) takes place only on rough parts of crystal surfaces and as a consequence, facets extend their size (see Fig. 33).

II.3.2. The ratchet effect

Theories of crystal shapes are usually focused on the equilibrium shape corresponding to the unique minimum of the total surface energy at constant crystal volume [60]. But in the real system the absolute minimum of the total energy can be accompanied by the secondary minima where the crystalline growth is blocked and the total surface thus stays in the metastable phase. All this result in the so called ratchet effect which takes place when the cyclic changes of temperature (Fig. 15) are applied to the crystal. This effect is the consequence of the metastability of the facets of crystal. We have observed the evolution of the form of the surface of crystal Pn3m (Fig. 34a-h) by the cyclic modification of the

47

temperature. It is possible to obtain the ratchet effect also by the variation of the ethanol concentration in the L1 phase, but it can be problematic for our experimental setup. The evolution of the crystal's surface takes place, because the number of the molecules of surfactant inside the crystal stays constant because the surfactant is not soluble in the phase L1. Observed extension of the facets of the crystal can be explained by the creation of new elementary unit cells on the rough parts of the crystal. These new unit cells must be created, because the number of molecules of the surfactant per unit cell decreases when the temperature increases or the concentration of ethanol decreases (Fig. 33).
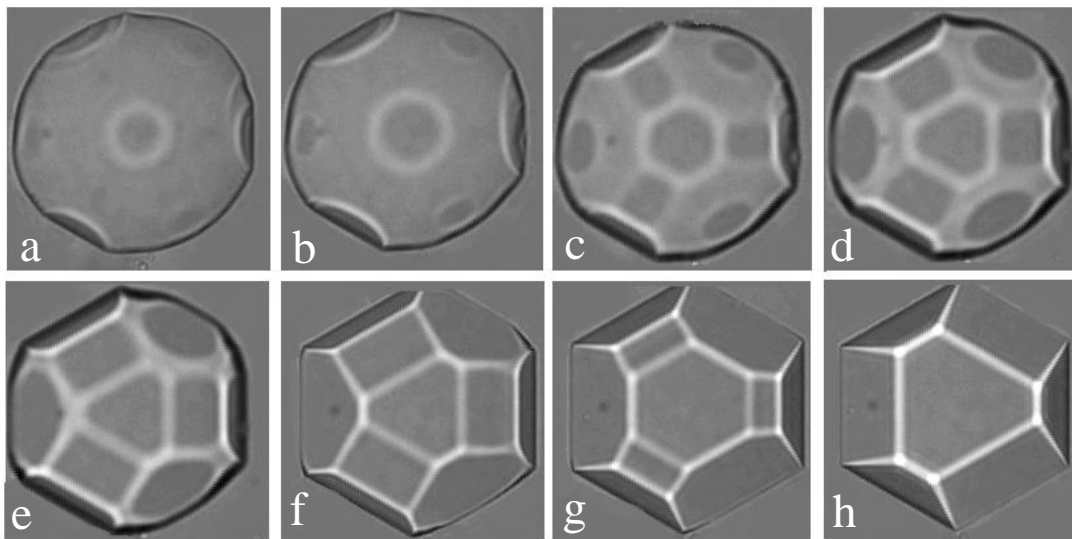
Fig. 32. Ratchet effect: evolution of the facets of the Pn3m crystal in L1 phase under the temperature cycling. Concentration of ethanol c_s = 8%.

A cyclic variation of the temperature was applied to the Pn3m crystal. During the positive ramp of the temperature, the size of the facets increased by the "redistribution" process (discussed earlier). During the negative ramp that the initial size of the facets will be recovered. It is so for the symmetric ramp. For an asymmetric ramp used in experiment this reversibility is broken. As a result we observed the growth of the facets size (Fig. 32d). If we apply sufficient number of the cycles, we obtain the crystal Pn3m which is limited exclusively by (111) facets (Fig. 32h).
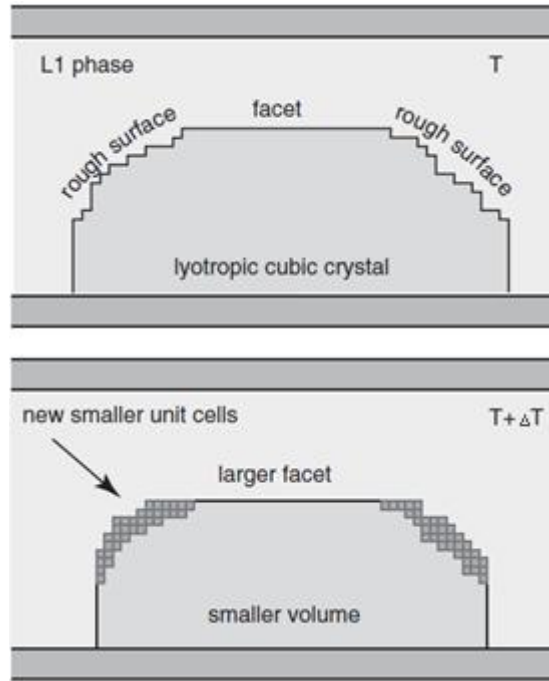
Fig. 33. Principle of the pseudo-growth phenomenon in lyotropic liquid crystals. For simplicity, a simple cubic crystal with (100)-type facets is presented.
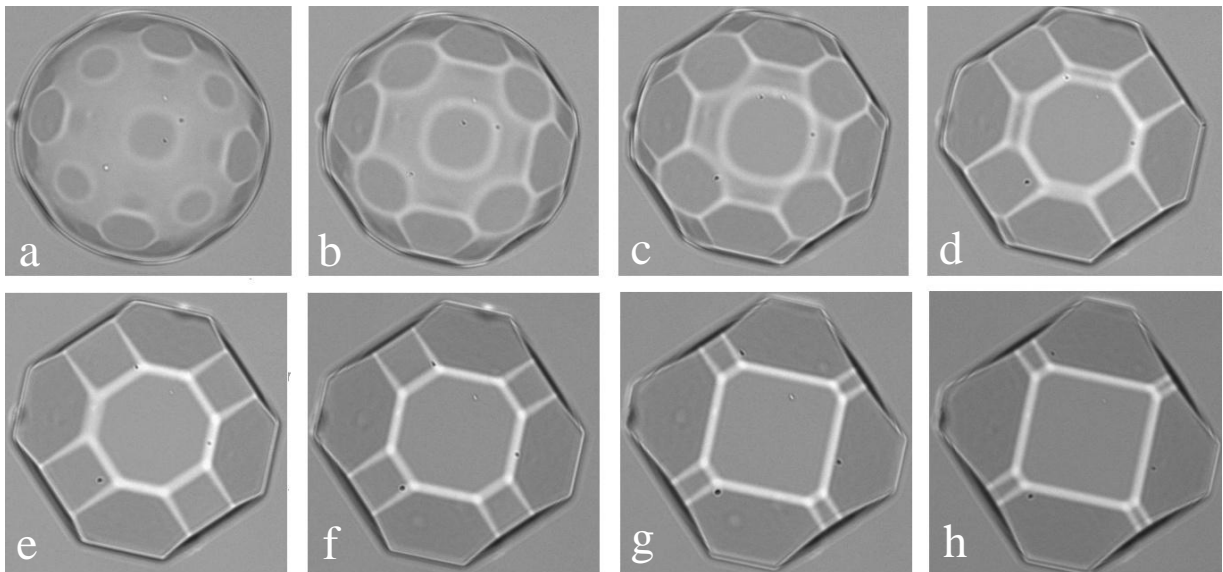
Fig. 34. Ratchet effect: evolution of the facets of the Im3m crystal in L1 phase under the temperature cycling. The concentration of ethanol c_s = 12%.

The series of photographs in Fig. 32 and Fig. 34 illustrate the behavior of Pn3m and Im3m crystals during one period of the temperature variation. The a, b, c, d photographs have

been taken during the slow positive temperature ramp. They illustrate the "pseudo-growth" phenomenon during which facets increase their size at the expense of rough surfaces that shrink.

II.3.3. Deformation of Pn3m crystal in a temperature gradient parallel to the capillary walls, (111)//glass orientation

When a temperature gradient parallel to the longitudinal axis of the glass capillary is applied, one observes a progressive deformation of Pn3m crystals situated at the capillary walls. This is illustrated by the series of four photographs in Fig. 35 which were taken at intervals of one hour. The temperature gradient applied here was gradT=0.6K/mm. Clearly, upon the action of the temperature gradient, the facets located on the colder side of the crystal increase their size while those located on the warmer side are shrinking.
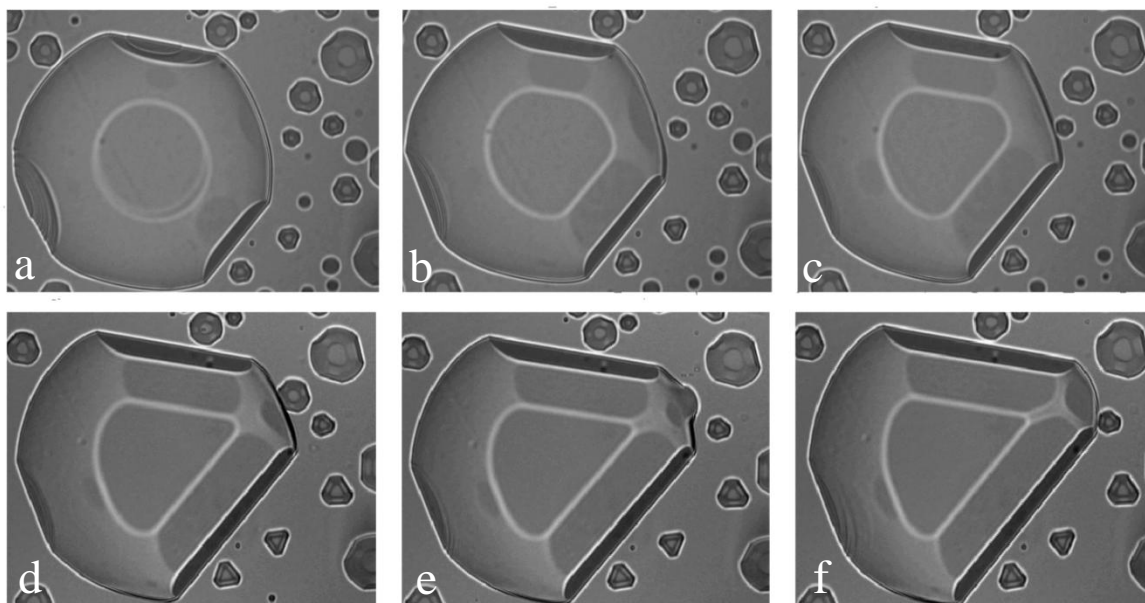
Fig. 35. Thermopermeation or the Ludwig-Soret effect: evolution of the facets situated on the colder side of the Pn3m crystal in L2 phase, concentration of ethanol 8%.

These processes occurring at warmer and colder sides of the crystal are similar to growth and melting of crystals. On the colder side, the apparent growth of the crystal involves

exclusively progression (an outward motion) of rough surfaces, the facets being blocked. The apparent "melting" of the crystal on its warmer side is rather a kind of a "deconstruction" process taking place both on rough surfaces and on facets. The rough surfaces are regressing continuously while the motion of facets is mediated by nucleation and collapsing of steps of a macroscopic height. Such macroscopic steps are visible on the warmer facet in Fig. 35 [59].

II.3.4. Phase diagram of the quaternary system Phytantriol+DSPG/ Ethanol/ Water

From the previously obtained data (the stages of R. Sheshka and P. Faye) we have already known the phase diagram of the ternary phytantriol/water/ ethanol mixture (Fig. 36).
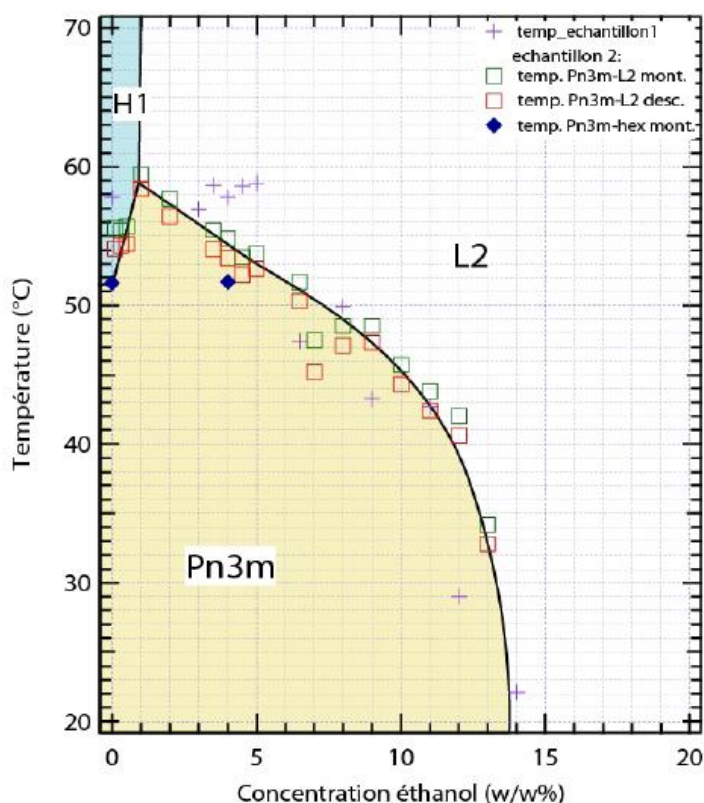
Fig. 36. Phase diagam of the ternary phytantriol/water/ethanol system obtained previously by R. Sheshka and P.Faye.

Using this phase diagram we were able to select the appropriate temperature and concentration conditions to obtain the needed phase.

When exploring this diagram in the range of the temperatures between 20°C and 43°C we concluded that this phase diagram has to be modified, because two other phases L3 and Lα are in fact situated between Pn3m and L2 phases. For example, at 33°C under increasing concentration of ethanol from 8% we observed first the transition into the L3 phase then from L3 to Lα phase, finally from Lα to L2. All data obtained by this method are summarized on the phase diagram in Fig. 37.
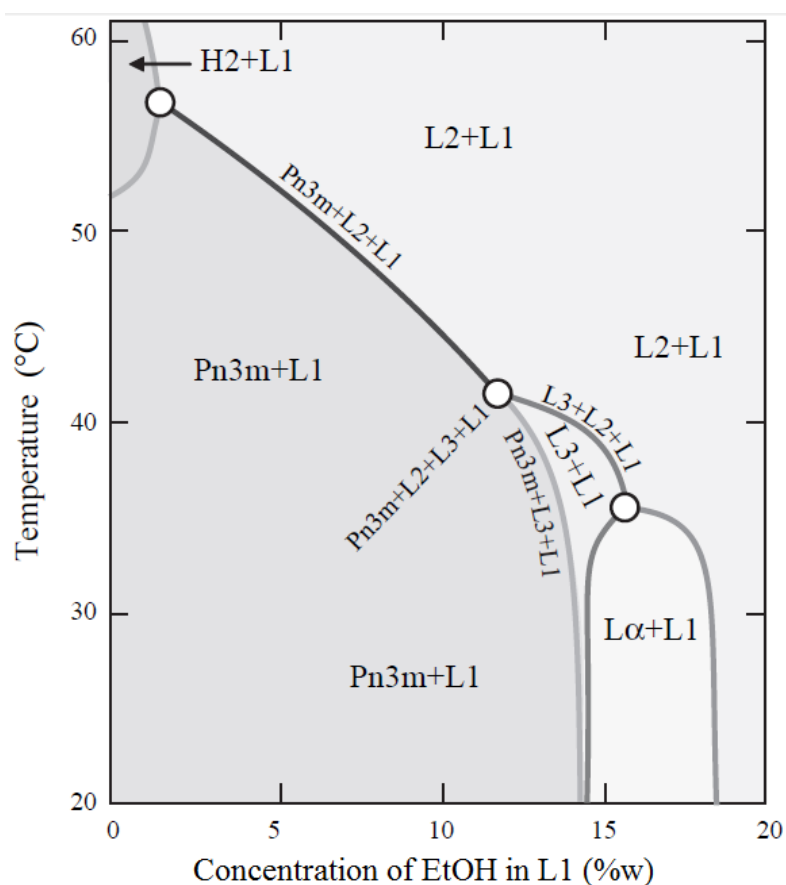
Fig. 37. Corrected phase diagram of the the phytantriol/water/ethanol system.

As it have been mentioned in chapter II.2.5.7 to obtain the phase transition Pn3m→Im3m the forth component - DSPG – has to be added to the system already containing water, phytantriol and ethanol. In practice we mixed the phytantriol with 1.8% of DSPG. We have found that this concentration is sufficient to induce the Im3m phase. The question which

remains still to be answered is: what is the concentration of DSPG in Im3m phase? Indeed, during the preparation of the sample by the *ad hoc* method (Fig. 18) some amount of DSPG was certainly wasted and washed out from the capillary.

With such a sample we have found that the new transition line Pn3m-Im3m is present on the phase diagram. In Fig. 38 inverted full triangles indicate observations of this Pn3m to Im3m transition which can be achieved by variation of both the temperature and the ethanol concentration. The phase diagrams shown in Figs. 36-38 are not the orthodox ones.
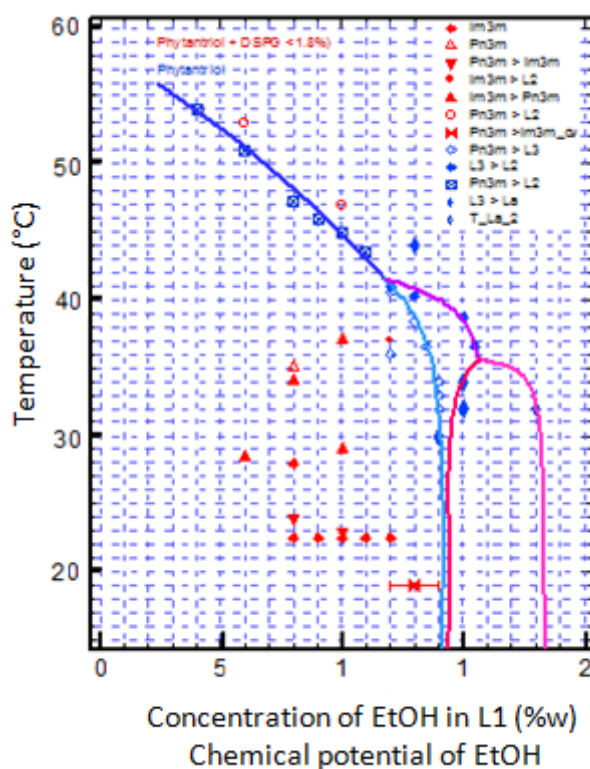
Fig. 38. New phase diagram of the the phytantriol/water/system/DSPG.

The most common method for plotting composition in a ternary system uses the Gibbs triangle (Fig. 39). The corners represent the pure components A, B and C. The edges AB, BC and AC represent the corresponding binary compositions. Ternary compositions are plotted as points within the triangle ABC [63].

To represent completely the thermodynamic behavior of the ternary system the effect of the temperature has to be considered. By plotting the temperature on an axis perpendicular

53

to the composition triangle the phase diagram takes the shape of a right triangular prism (Fig. 39). We did not achieve the exploration of the whole triangular prism because such a task would be too complicated and time consuming.
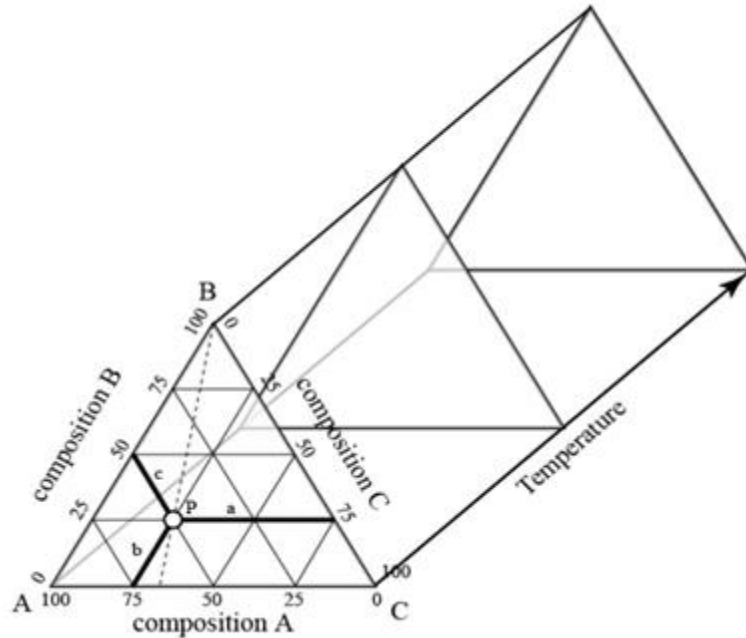
Fig. 39. Phase diagram of the ternary mixture ABC.

Instead of that, we show in Figs. 40, 41, 42, and 43 several isothermal sections of this 3D phase diagram.

In Fig. 40 we show the tentative structure of the isothermal section for temperature higher than 43°C in agreement with the simplified phase diagram shown in Fig. 37. The isothermal section shown in Fig. 40 contains two biphasic domains Pn3m+L1 and L2+L1 as well as the triangular three phase coexistence domain Pn3m, L2, and L1.
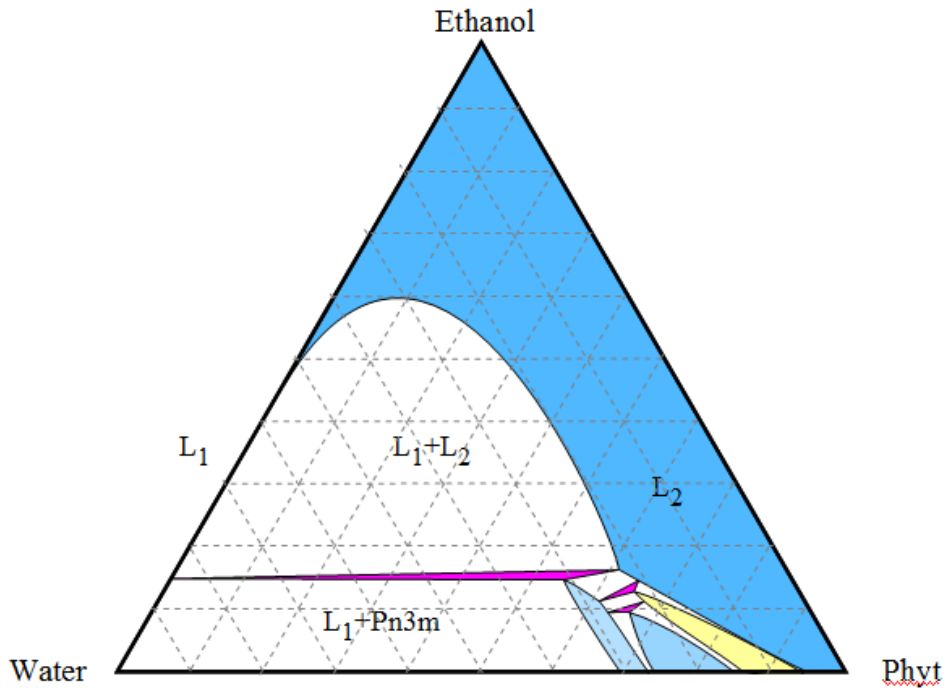
Fig. 40. Phase diagram of the ternary phytantriol/water/ethanol system for the temperatures higher than 43°C.
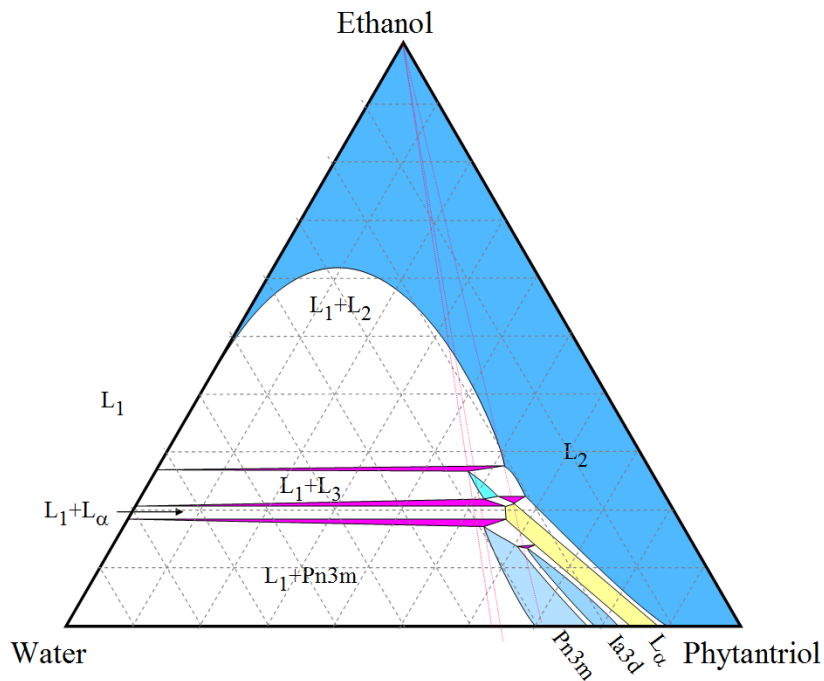
Fig. 41. Phase diagram of the ternary phytantriol/water/ethanol system for the temperatures lower than 43°C.

For temperatures lower than 43°C the triangular three phase domain Pn3m/L2/L1 is splitted into three phase domains because the fourth phase appears – the L3 phase. This is visible in Fig. 41. Let us stress that the three phase domain L1/L2/L3 involves the coexistence of three isotropic phases. There are three triangles of the three phase coexistence: L1/L2/L3; L1/Pn3m/L3; L3/L2/Pn3m. The image in Fig. 41 experimentally proves this. There is a unique temperature 43°C where four phases coexistence is possible (Fig. 41).

II.3.5. L1-in-Pn3m inclusions: slopes of phase boundaries and molecular diffusivities

In our study, the phase behavior of phytantriol/water/ethanol system has been explored by varying two intensive parameters: the temperature T and the concentration c_s of the water/ethanol solution flowing through the capillary and surrounding the sample. Results of our observation are summarized in the simplified phase diagram T versus c_s shown in Fig. 37. Each point in this phase diagram is supposed to represent an equilibrium state of the ternary mixture in which the temperature is uniform and the chemical potentials of all components are equal in all coexisting phases. In practice, the isothermal condition is quite easy to satisfy as the typical length scale of sample of ~ 100 μm because the thermal relaxation time is quite short.

The chemical equilibrium is much more difficult to reach because molecular diffusivities are much smaller than the thermal ones. As an example, let us consider the process of relaxation after an isothermal negative variation of concentration $\Delta c_s = c_s - c_s'$ inside the biphasic domain Pn3m+L1. It is illustrated by the series of four images (a-d) in Fig. 42. Clearly, the process of relaxation involves nucleation and growth of L1 inclusions inside the Pn3m crystal.

This phenomenon can be understood with the help of the phase diagram shown in Fig. 42e and f. The experiment starts from the state of equilibrium in which the Pn3m monocrystal coexists with the ethanol/water solution at the concentration c_s. The composition of the crystal corresponds to the position (a) at the boundary of the monophasic domain Pn3m.

After the change of the ethanol-in-water concentration from c_s to c_s' the system evolves toward the new equilibrium state represented in Fig. 42e and f by the second tie line extending from c_s' to a'. Let us emphasize that during this evolution the mass of phytantriol inside the Pn3m crystal remains constant because phytantriol is not soluble in the surrounding water/ethanol solution. On the contrary, changes in masses of water and/or ethanol contained in the crystal are necessary. To find these changes, let us remark first that the axis labeled 'ethanol' in Fig. 42f, directed from point a to the 'ethanol' vertex of the Gibbs triangle (Fig. 42e) is a locus of points in which the content of ethanol increases. On the axis labeled 'water' the inverse occurs. Now, one can ask what is the slope of the a-a' segment with respect to these axes?

The answer to this question can be interred from the observation that inclusions of L1 phase nucleate and grow in Pn3m crystals when the concentration of ethanl c_s is lowered fast enough (see Fig. 42a-e). Our experiments have also shown that L1-in-Pn3m inclusions shrink when the concentration of ethanol is increased.

To explain these observations, let us remind that a similar phenomenon has been observed in the C12EO2/water binary system [64] in the L1+Pn3m coexistence range (see Fig. 43) upon heating. Let us suppose that the initial state of the Pn3m-in-L1 crystal is represented by the point a in Fig. 43. If the heating rate was slow enough (quasi-static), the composition of the crystal would follow the border of the Pn3m domain from a to a'. However, the molecular diffusivity of water in Pn3m phase is much slower than the thermal diffusivity. Therefore, upon a steep temperature change, the interior of the Pn3m crystal follows a different trajectory: first, rapidly, from a to b and then, slowly, from b to a'. In the state b, the crystal is out of equilibrium and the nucleation of L1 inclusions occurs. In the present case of the phytantriol/water/ethanol ternary mixture, the nucleation of L1 inclusions can occur if molecular diffusivities of water and ethanol in the Pn3m crystal are different. One can argue that the diffusivity of ethanol, completely soluble in both water and phytantriol, is larger than the diffusivity of water which is only partially soluble in phytantriol (miscibility gap). In such a case, if the starting point is a in Fig. 42b, and the concentration of ethanol in the L1 phase is lowered rapidly, the interior of a large Pn3m crystal (like the one in Fig. 42a-e) follows the trajectory aba' which drives the Pn3m phase into the state out of equilibrium b, characterized by an excess of water so that the nucleation of L1 inclusions occurs.
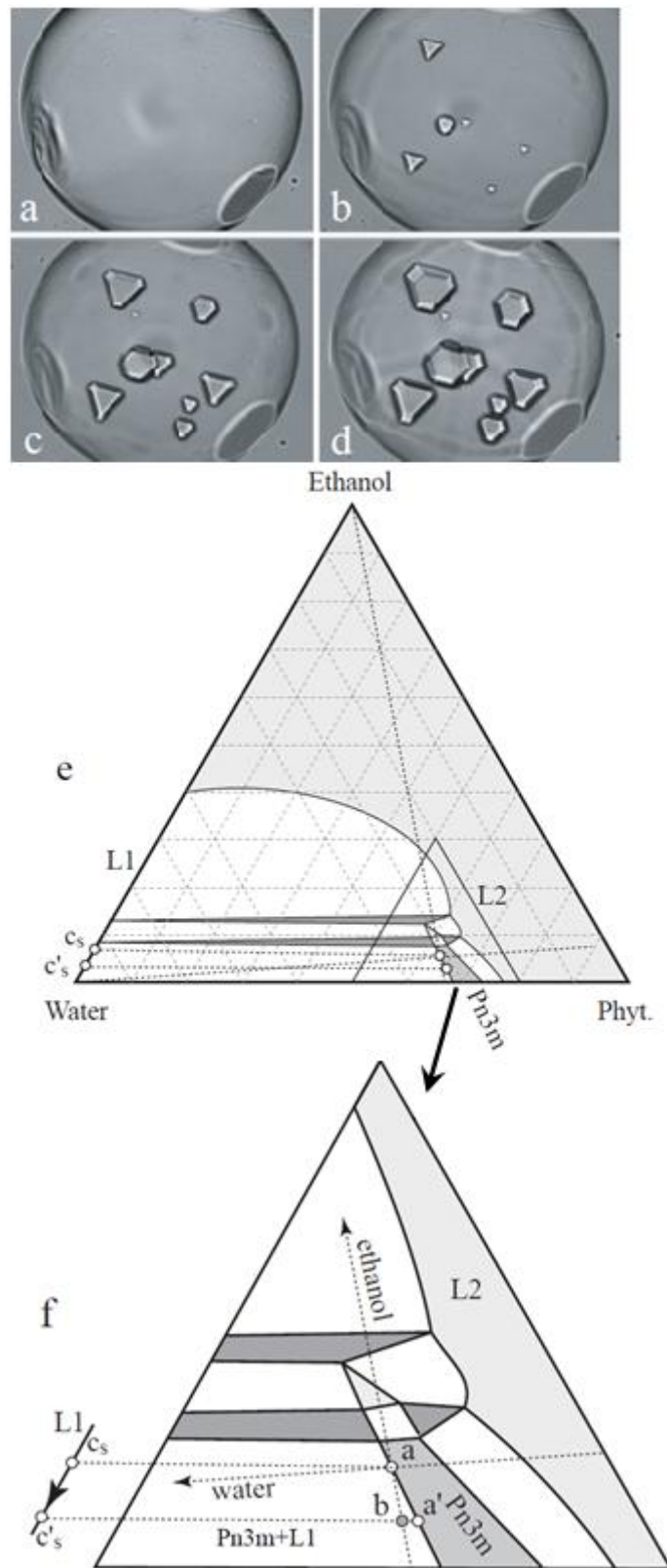
Fig. 42. Nucleation of L1 inclusions in a Pn3m-in-L1 crystal driven by a fast negative change of the ethanol concentration from c_s to c'_s at T=40°C: a-d) observations, e-f) tentative phase diagram of the PWE ternary system.
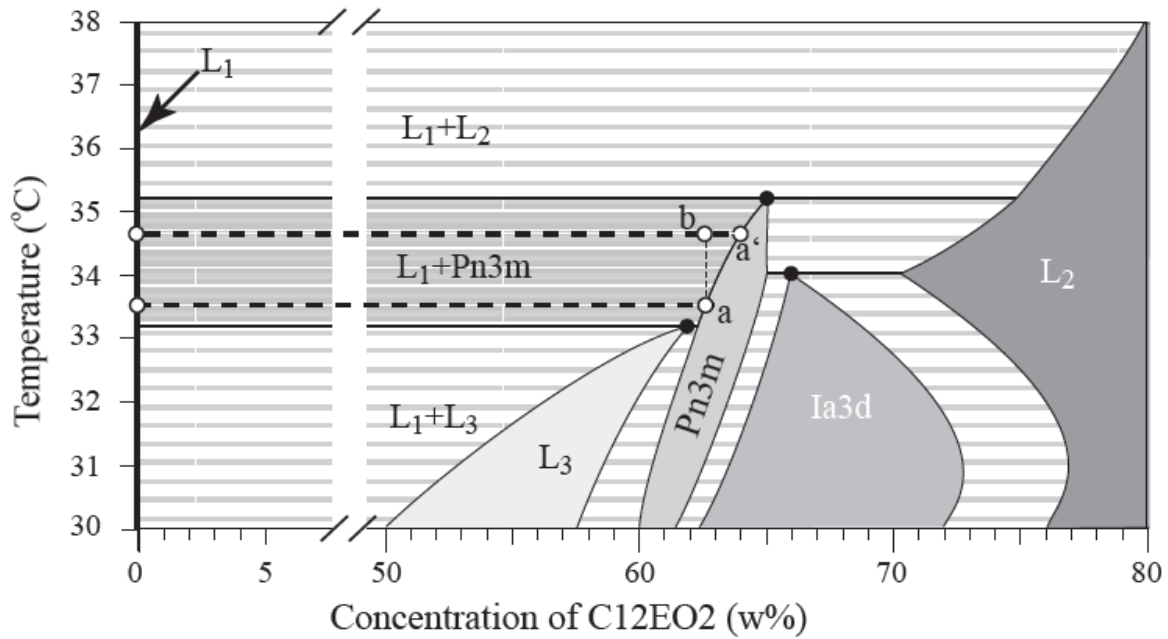
Fig. 43. Out of equilibrium excursion driven by a rapid heating in the binary system C12EO2/water. It results in nucleation of L1-in-Pn3m inclusions.

We can conclude that the (L1+Pn3m)/Pn3m boundary is tilted to the left with respect to the "ethanol" axis as shown in Fig. 42f.

II.3.6. Isoplethal nucleation of L1 inclusions

We have observed that nucleation of L1 inclusions in Pn3m-in-L1 crystals occurs also at isoplethal conditions (i.e. at c_s = const) when temperature T is raised too rapidly. It means that the boundary between the L1+Pn3m and Pn3m domains is tilted with respect to the T axis of the full 3D phase diagram of the phytantriol/water/ethanol system as shown in Fig. 44.
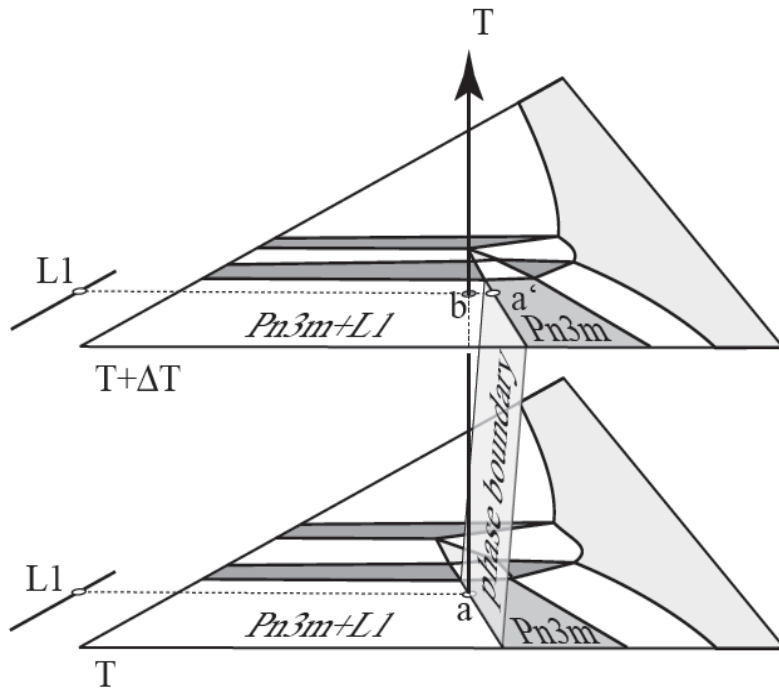
Fig. 44. Excursion into the L1+Pn3m coexistence domain driven by heating from T to T+ΔT. The isothermal section at temperature T is the same as in Fig. 42f.

III. Experiment alanalysis of the cubosomes by means of cryo-transmission electron microscopy

III.1. Aim of the experiments

We would like to investigate the geometry of small cubosomes by cryo-TEM. The phase diagram of the mixture of phytantriol and water has been already examined in details in Fig.37. The topology of the phase diagram with the regions occupied by cubic phases was determined. We would like to use cryo-TEM for the investigation of the cubosomes formed of Pn3m bicontinuous phase (previous chapter) and compare their geometry with the structure of cubosomes calculated by minimization of the Landau-Ginzburg free energy functional (next chapter). We expect that the images of small cubosomes obtained in cryo-TEM from vitrified samples will enable us better understanding the process of their formation and the influence of size of cubosomes on their structure.

III.2. Cryo-transmission electron microscopy (cryo-TEM)

'The transmission electron microscope can be compared with a slide projector. In a slide projector light from a light source is made into a parallel beam by the condenser lens; this passes through the object and then focused as an enlarged image onto the screen by the objective lens' [64]. In the electron microscope the light source is replaced by the electron source, the glass lenses are replaced by magnetic lenses, and the projection screen is replaced by a fluorescent screen. [64]. All the measurements are made in vacuum and the object of the investigation has to be thin enough to allow electrons to pass through it.

The transmission electron microscope is composed of an electron optical column, a vacuum system, the necessary electronics, and control software. The electron column includes elements analogous to those of a light microscope, with the exception that the light source is replaced by an electron gun, which is built into the column, and the glass lenses are replaced by

electromagnetic lenses. The power of the magnetic lenses can be changed depending on the current.

The electron beam comes from the electronic gun at the top of the column and is condensed into a parallel beam at the specimen by the condenser lenses. Typically the thickness of the pattern is about 0.5 μm or less. Higher energy electron can penetrate thicker samples. After passing through the sample electrons are collected and focused by the objective lens and a magnified real image of the pattern is projected by the projection lens onto the screen at the bottom of the column. Vacuum is necessary in the technique of TEM, otherwise the electrons would collide with air molecules and be scattered or absorbed.

All the characteristics of cryo-TEM used in our experiments are shown in Fig. 45. The electron gun for the TEM we used in our experiments is lanthanum hexaboride LaB6. LaB6 guns depend on thermoionic emission of electrons from a heated source, a lanthanum hexaboride crystal. LaB6 can provide high brightness and have significantly longer lifetimes, but require higher vacuum levels, which increases the microscope's cost.

Phase contrast and diffraction contrast are the most important factors in image formation for crystalline patterns. Lenses in cryo-transmission electron microscopy play the same role as the lenses in optical microscopy with the exception that the electromagnetic lenses focus the beam of the electrons not the light. To obtain a high resolution image a special technique is needed to avoid aberration. If the light or a beam of electrons don't have the same wavelength, the focus after the transition through the lens will not be in one point but in different points.

Observation

Source of the electrons lanthanium hexaborure (LaB6) of 200kV

TEM JEOL 2011

LPS UPS Orsay

Lens of high resolution UHR
focale : 1.9 mm
Cs : 0.5 mm
Cc : 1.1 mm
Resolution : 1,4 Å in line, 1,94 Å in point
tilt : ± 22°

Cold object carrier (cryo-microscopy)
stability on temperature : -182°C
tilt : ± 15° in cold
Resolution of cryo-TEM : 5Å crystals
9-15Å isolated particles , cryocut

Dedicated to:
- cryoME (nano-objects)
- high resolution

source of electrons

Condenser lens

Objective lens

Object carrier

Difraction lens
Intermediate lens
Projective 1
Projective 2

Display

Plans films

Filter loss of energy (GIF)
camera CCD 1024x1024
resolution in energy <1,5 eV

Fig. 45. Characteristics of cryo-transmission electron microscopy used in experiment at the University of Orsay, Paris-Sud.

III.3. Preparation of the samples

The specimen must be small and stable enough to permit the introduction into the microscope and thin enough to permit transmission of electrons. In our experiment we made our samples not thicker than 40nm (the thickness of the microscope's grid). The water should be removed from the sample and the sample should be in its original state. First, the pattern are treated in liquid nitrogen container then replaced by 3 mm diameter copper specimen grid at liquid nitrogen temperatures and coated with a structureless carbon film of 0.1 μm thick. Obviously, freezing techniques can also cause the damage of the sample. Vitrification is a rapid freezing process that occurs so quickly that water molecules do not have enough time to crystallize. They form a vitreous (amorphous) solid that causes no damage to the sample structure. Fig. 46 shows the trajectory of the electron beam passing through the pattern.
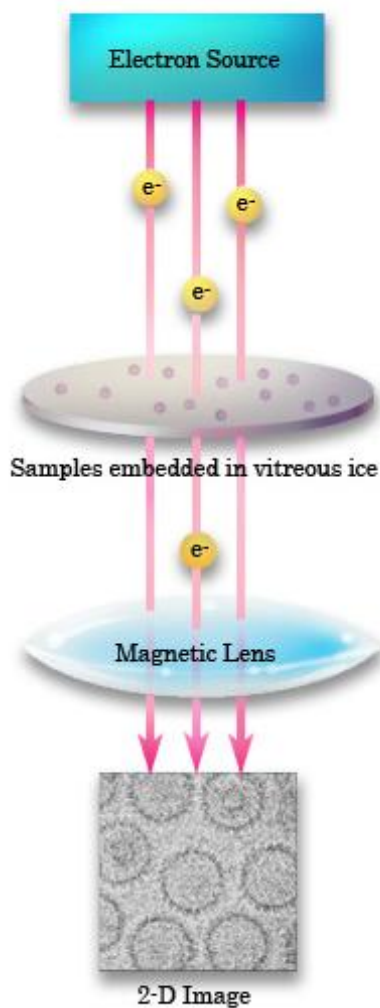
Fig. 46. Trajectory of the electron beam passing through the sample [64].

III.4. Results

We have prepared the cubosomes using the method which is well-known in the literature [36]. Although, the attempts to prepare cubosomes using the phase diagram of phytantriol/water/ethanol system without using any stabilizing agent have been taken, they didn't give any satisfactory results: particles were stuck together.

To prepare cubosomes we mixed some amount of phytantriol with water and a stabilizer Poloxamer-407. The standard method of preparation of the cubosomes gives the particles of Pn3m symmetry. The procedure of preparation of the cubosomes is shown in Fig. 47. We mixed some amount of phytantriol with the stabilizer (according to ratio in the publication) and water

and ultrasonicated this mixture within 10 or 15 minutes. The cubosomes were cryo-fixed on the day of their preparation and analyzed on the second day of cryo-fixation.
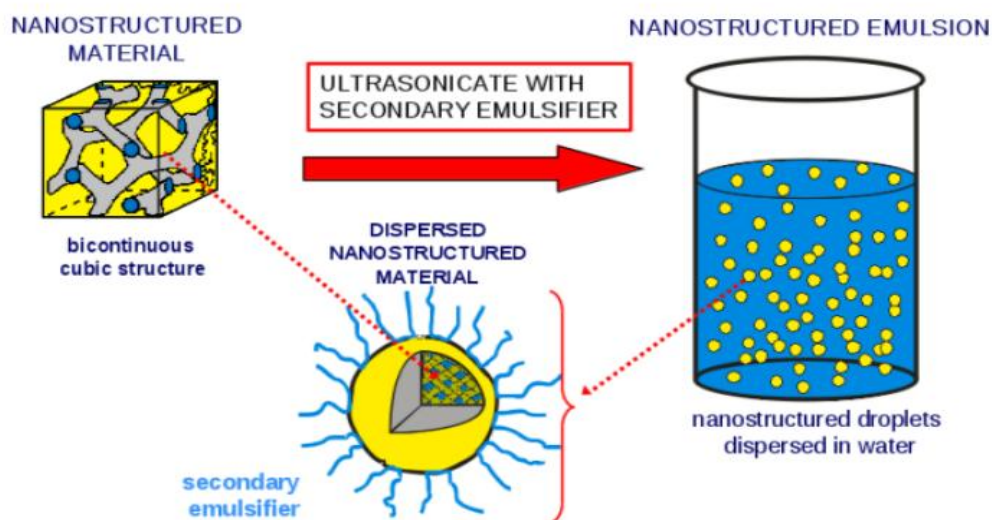
Fig. 47. Standard method for the preparation of the cubosomes (picture is taken from the presentation of Dr. Jeril Degrouard, University of Orsay, Paris-Sud).

The first images on the first day after the preparation are shown in Fig. 48.
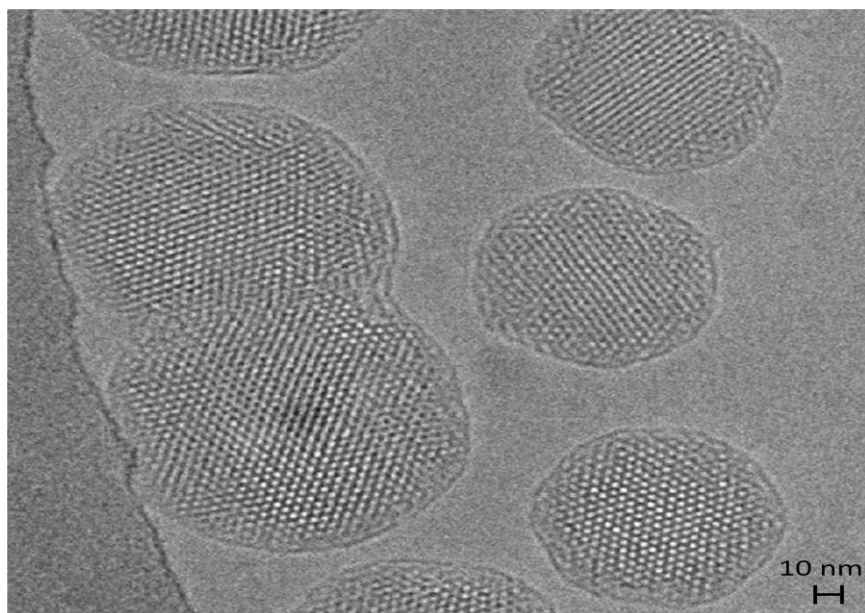
Fig. 48. Images of the cubosomes obtained by cryo-TEM on the first day after preparation, defocus −4000 nm.

65

We have observed many particles with a well-organized internal structure. After one day of preparation we haven't observed any contamination of our samples and the formation of vesicles.
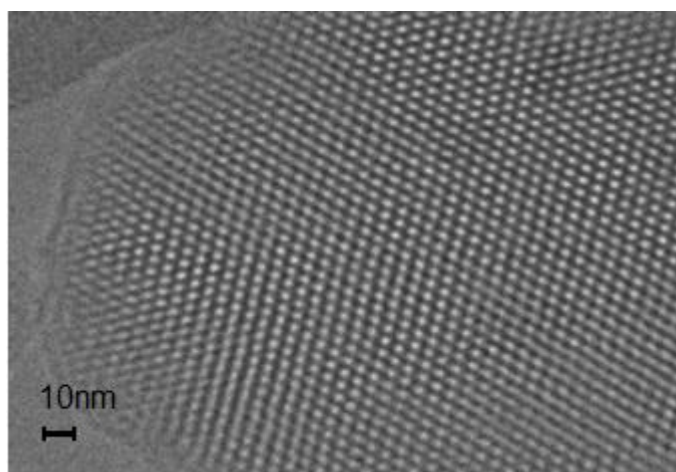
Fig. 49. Images of the cubosomes obtained by cryo-TEM on the first day after preparation, defocus – 4000 nm.

Preparing cubosomes with high accuracy results in the images with the contrast which allowed us to see the periodic structure of the channels inside the particle (Fig. 49).

We have repeated the experiments after one month of the preparation of the cubosomes. In this case the images were not as good as previous ones. The particles were contaminated and the formation of additional structures took place (Fig. 50).
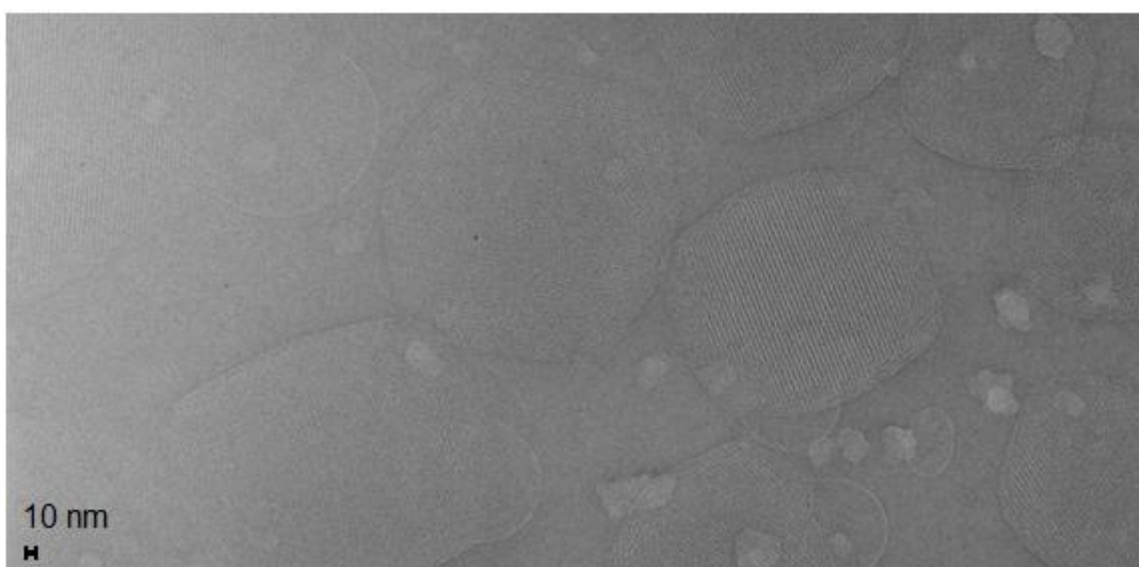
Fig. 50. Images of the cubosomes obtained by cryo-TEM after one month after the preparation, defocus – 3000 nm.

66

We have observed enough images of the cubosomes to make the statistics. After making a statistics we concluded that the particles within the sizes from 125 nm to 170 nm tend to be spherical while those with the larger sizes approximately 300 nm – 370 nm tend to have polyhedral shape (Fig. 51). The histogram of the sizes of spherical cubosomes is shown in Fig. 52.
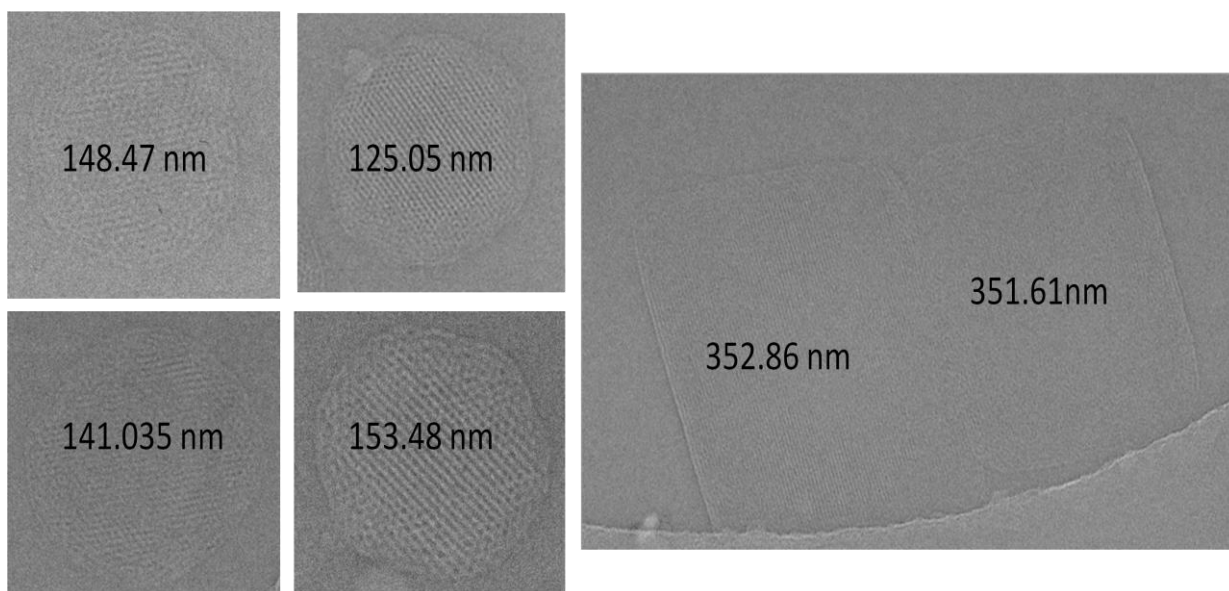
Fig. 51. Images of the cubosomes obtained by cryo-TEM, defocus – 3000 nm.
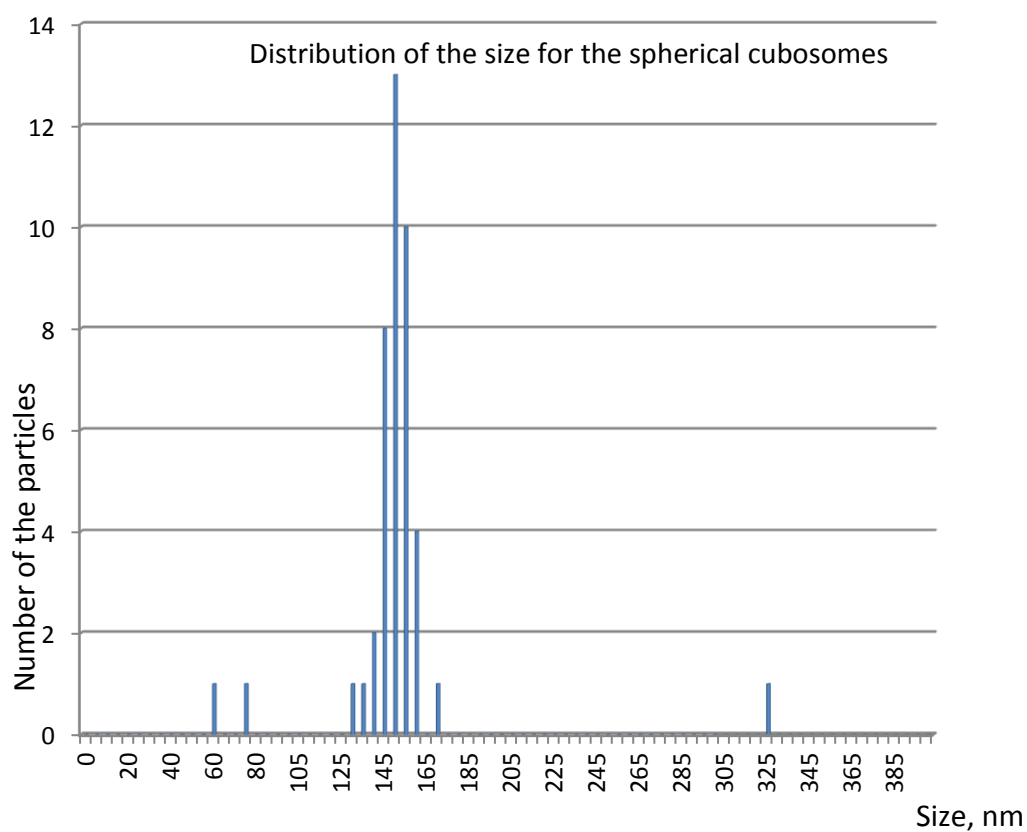
Fig. 52. Distribution of the size for the spherical cubosomes.

We organized in a systematic way these images obtained by cryo-TEM. We have already mentioned that cubosomes were investigated either on the second day of the preparation or after one month of storing in the fridge.

First, we will concentrate on the images of the cubosomes which were obtained one day after cryo-fixation. Not all the images obtained will be shown but the best and the most informative ones. In Fig. 53 two cubosomes obtained one day after cryo-fixation are shown. The image was obtained with the defocus of 1600 nm. The sizes of the cubosomes were calculated using the program ImageJ.
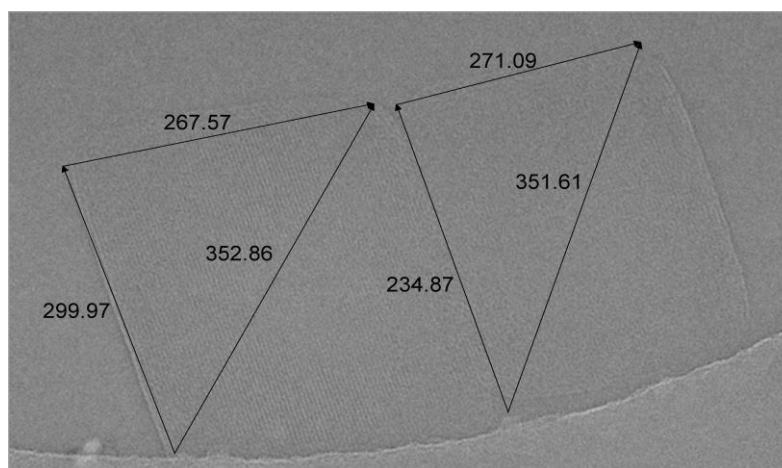
Fig. 53. Images of the cubosomes with rectangular shape obtained by cryo-TEM with the defocus of 1600 nm. Sizes of the particles are shown in nanometers.

In Fig. 54 there is a cubosome which was obtained as in the previous case, but with the defocus of 2000 nm. As it can be seen from the image the cubosome shown in Fig. 54 has smaller size in comparison with the cubosomes shown in Fig. 53. It has rather spherical shape than rectangular. If one compares the cubosome shown in Fig. 54 with the schematic illustration of the spherical cubosome shown in Fig. 55, one can notice striking resemblance between these two images. In the experimental image of the cubosome there are some defects that can be seen in the surface. Making the comparison with the model structure we can speculate that the cubosomes are built of the bicontinuous phase of Pn3m symmetry.

It is important to note that most of the particles were often attached to the grid. This area is not penetrable for the electron beam. Therefore, it is difficult to obtain details of the internal structure [65].
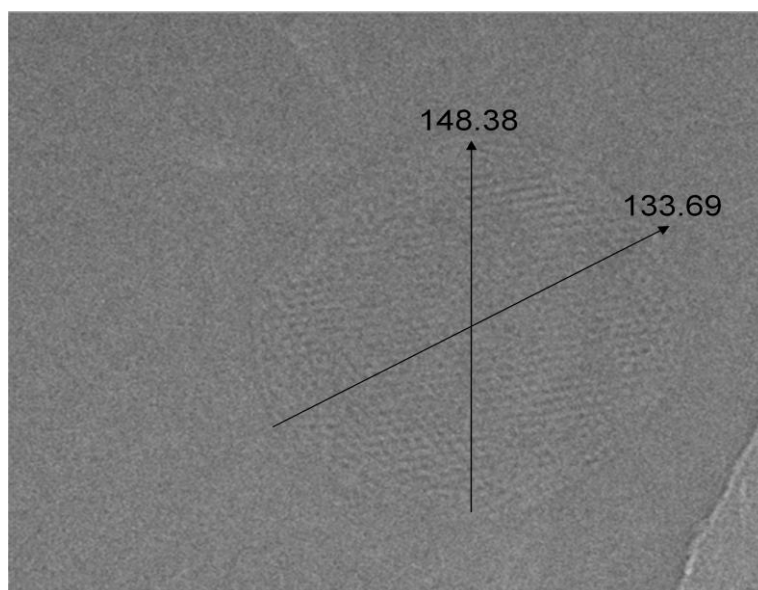
Fig. 54. Image of the spherical cubosome obtained by cryo-TEM with the defocus of 3000 nm. Sizes of the particles are shown in nanometers.
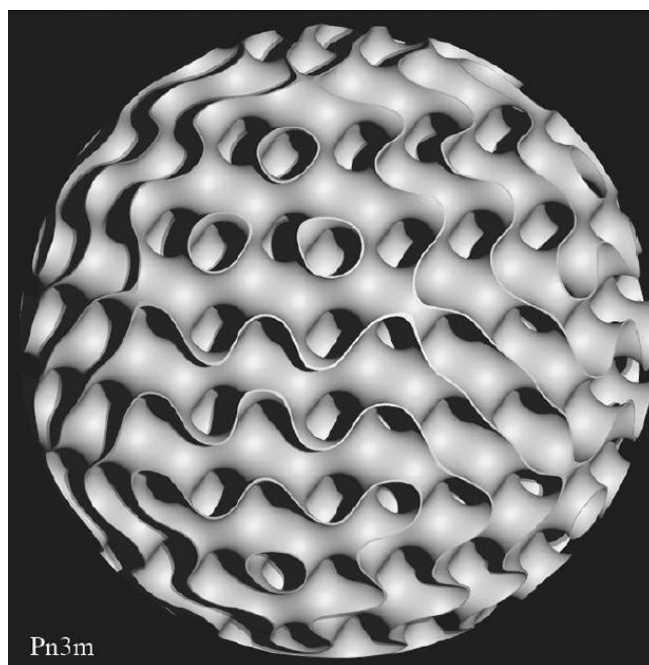
Fig. 55. Cut of the bicontinuous cubic liquid crystalline phase Pn3m (Spherical domain of the Level Surface. The level Surface has the same grey shade on its two sides) [83].

We also observed that smaller particles could adhere to each other forming a polyhedral shape 'big particle' (see Fig. 56). In Fig. 57 there are images of cubosomes where the internal structure is well seen. In some cases we saw small cubosome which is located near the biggest one like in Fig. 58. The effect of the stabilizer is also visible in the cryo-TEM images. Fig. 59 shows the cubosome with attached vesicles. Such cubosomes with ''ears'' are often encountered in the experiments.
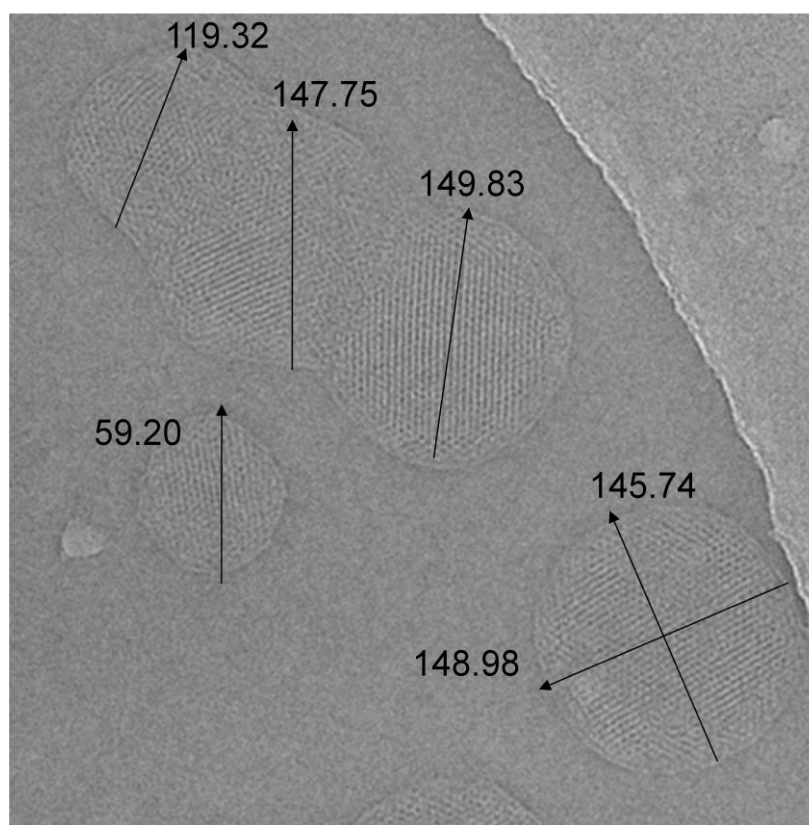
Fig. 56. Images of the cubosomes obtained by cryo-TEM with the defocus of 3000 nm. Sizes of the particles are reported in nanometers.
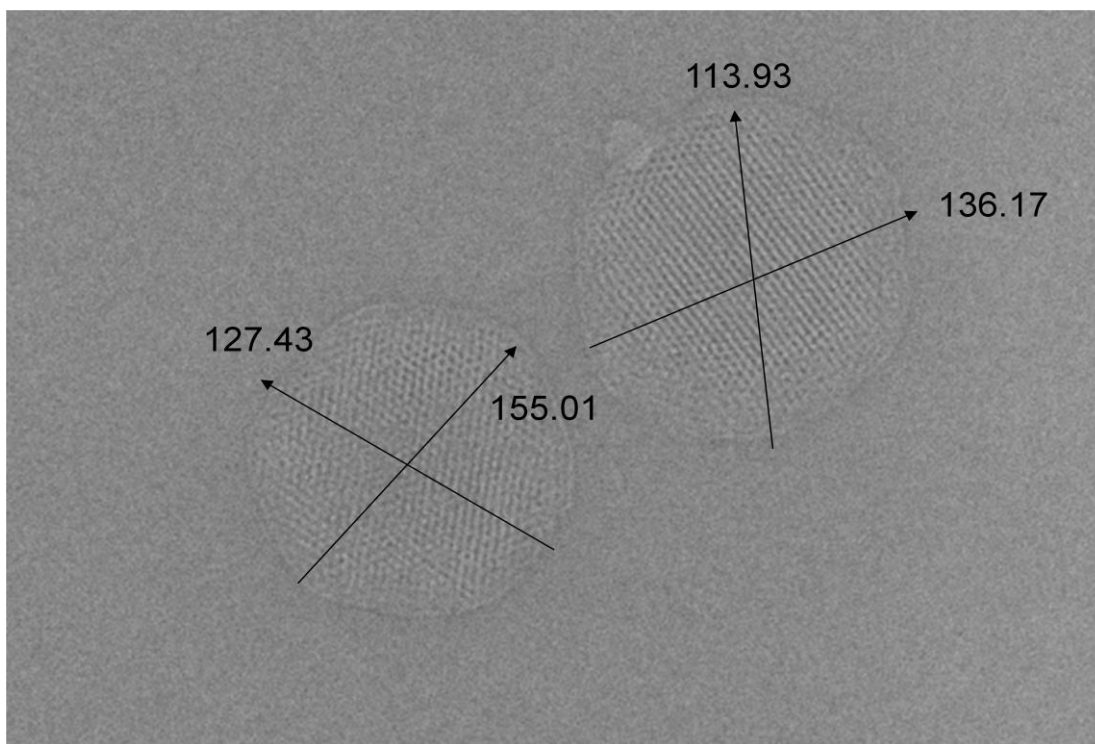
Fig. 57. Images of the cubosomes obtained by cryo-TEM with the defocus of 3000 nm. Sizes of the particles are reported in nanometers.
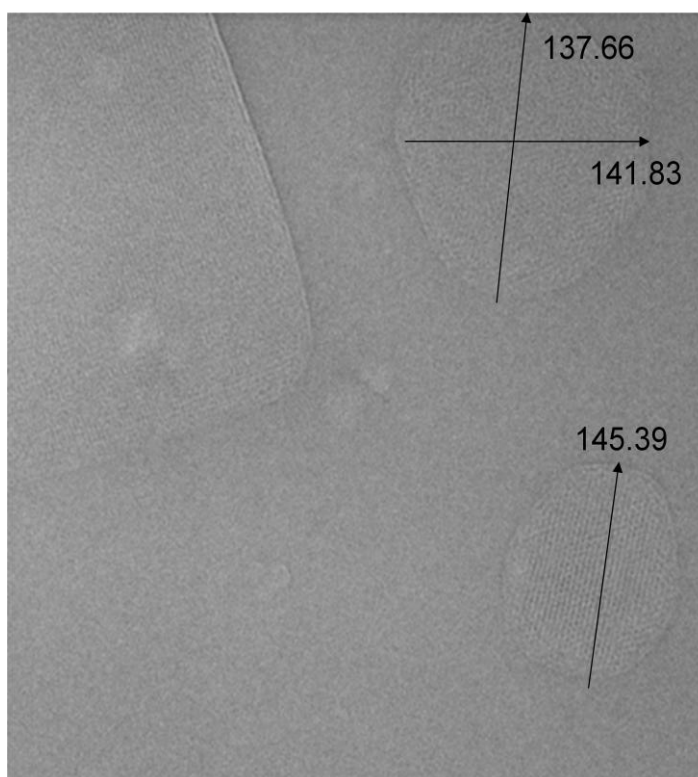
Fig. 58. Images of the cubosomes obtained by cryo-TEM. Defocus 3000 nm. Sizes of the particles are reported in nanometers.

71
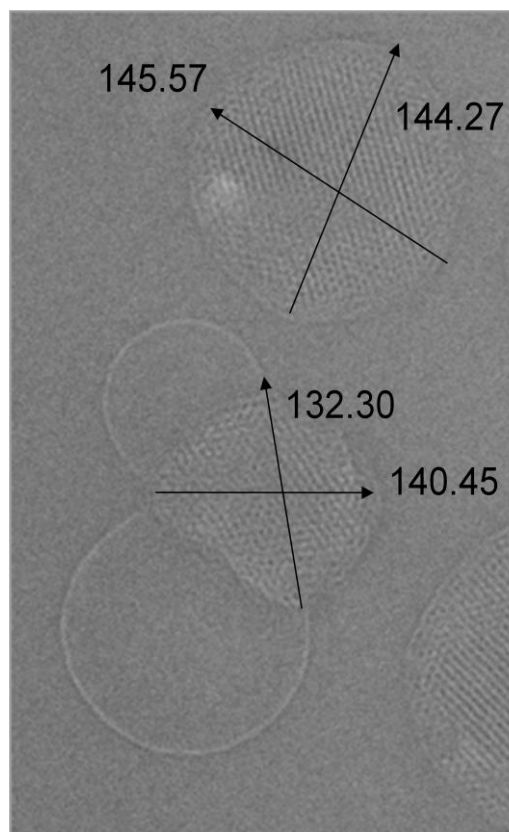
Fig. 59. Images of the cubosomes with attached vesicles obtained by cryo-TEM with the defocus of 2000 nm. Sizes of the particles are reported in nanometers.

After one month of storing the particles in the fridge, contaminations were also detected. Fig. 60 shows the image of the sample stored. The cubosomes are located very close to each other, have spherical shape and well-ordered structure. Contaminations are also visible.
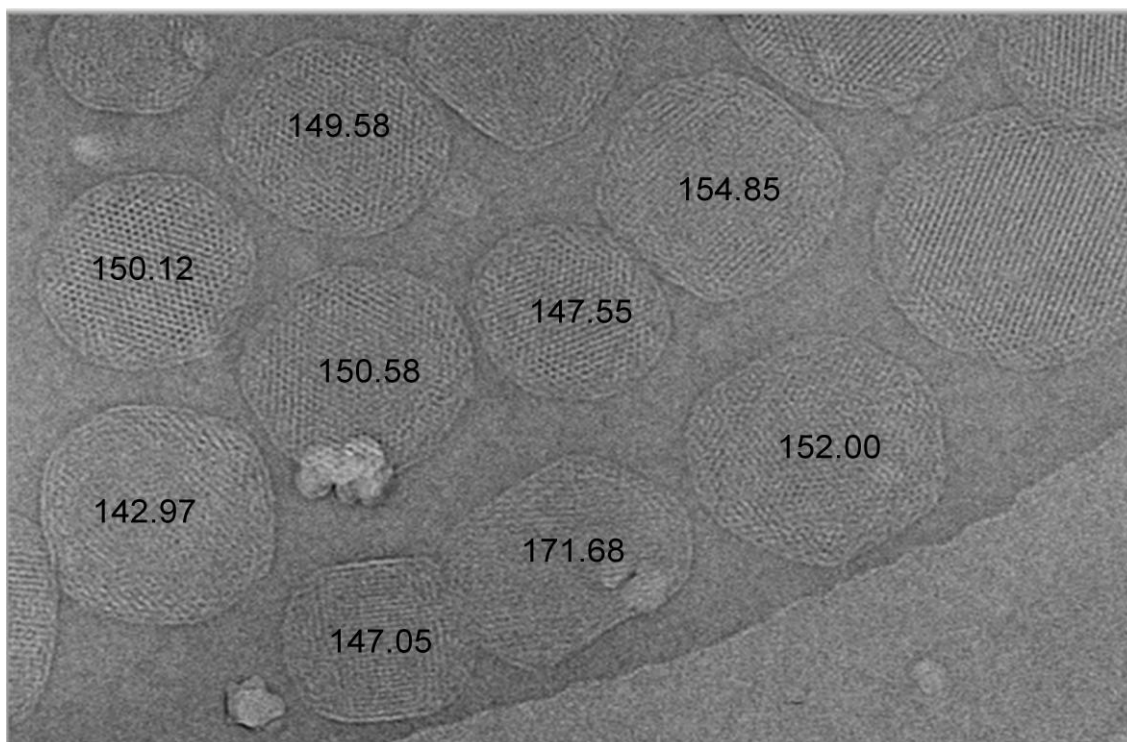
Fig. 60. Images of the cubosomes obtained by cryo-TEM with the defocus of 3000 nm. Samples were stored during one month in the fridge. Sizes of the particles are reported in nanometers.
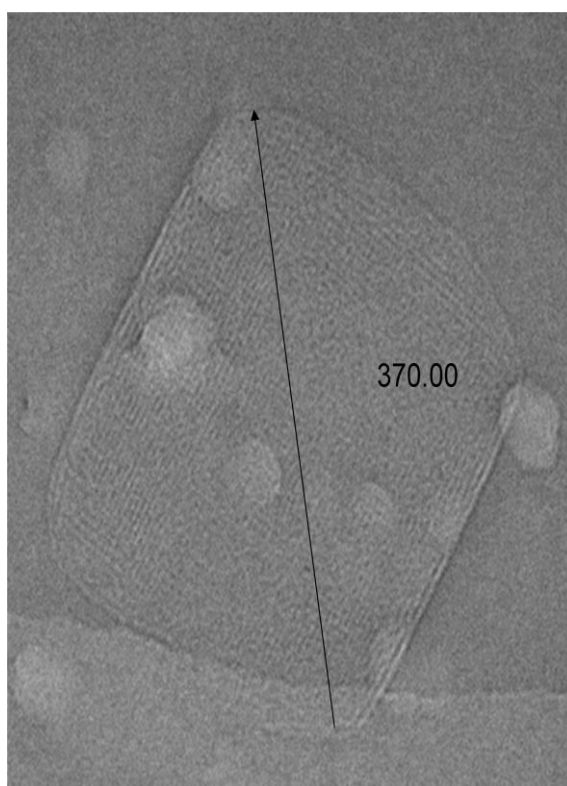
Fig. 61. Image of the cubosome obtained by cryo-TEM. Defocus 3000 nm. Sample was stored during more than one month in the fridge. Sizes of the particles are reported in nanometers.

73

When the samples are stored for the time longer than one month, larger contamination of the pattern takes place as can be seen in Fig. 61 or in Fig. 62.
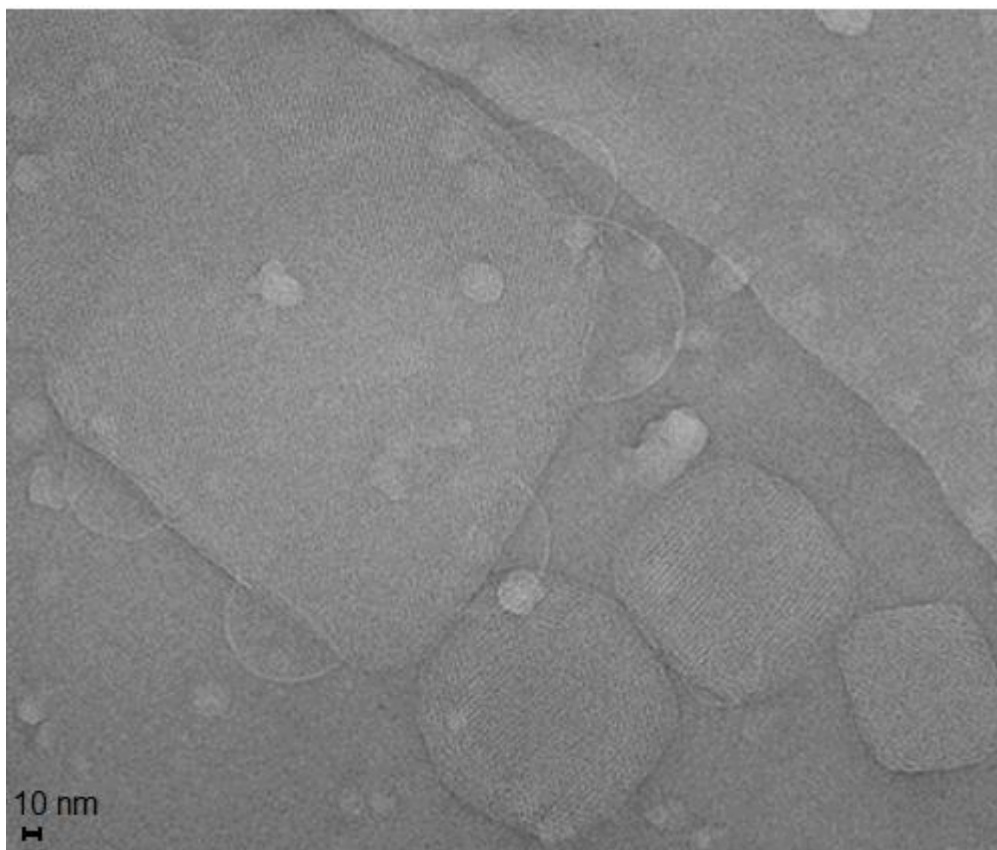
Fig. 62. Image of the cubosome obtained by cryo-TEM with the defocus of 4000 nm. Experimental conditions: sample was stored during more than one month in the fridge.

In Fig. 63 and Fig. 64 the images that were made after one day after cryo-fixation and after one month of preservation are presented. In all these images well-defined cubic or hexagonal structure can be seen. In the last row of Fig. 63 (third image defocus 4000 nm) the hexagonal structure of the particle is well visible. While in the last row of Fig. 64 (first image defocus 4000nm) cubic structure is observed. The crystalline order can be destroyed in some parts of the particle mainly because of the destructive feature of the electron beam passing through the sample. From our experimental observations it follows that nanoparticles of cubic phases (cubosomes) are metastable or unstable which makes the theoretical investigation of cubosomes difficult.

⊢⊣ 10 nm Defocus 2000 nm	⊢⊣ 10 nm Defocus 2000 nm	⊢⊣ 10 nm Defocus 3000 nm
⊢⊣ 10 nm Defocus 3000 nm	⊢⊣ 10 nm Defocus 3000 nm	⊢⊣ 10 nm Defocus 3000 nm
⊢⊣ 10 nm Defocus 3000 nm	⊢⊣ 10 nm Defocus 2000 nm	⊢⊣ 10 nm Defocus 2000 nm
⊢⊣ 10 nm Defocus 2000 nm	⊢⊣ 10 nm Defocus 3000 nm	⊢⊣ 10 nm Defocus 4000 nm
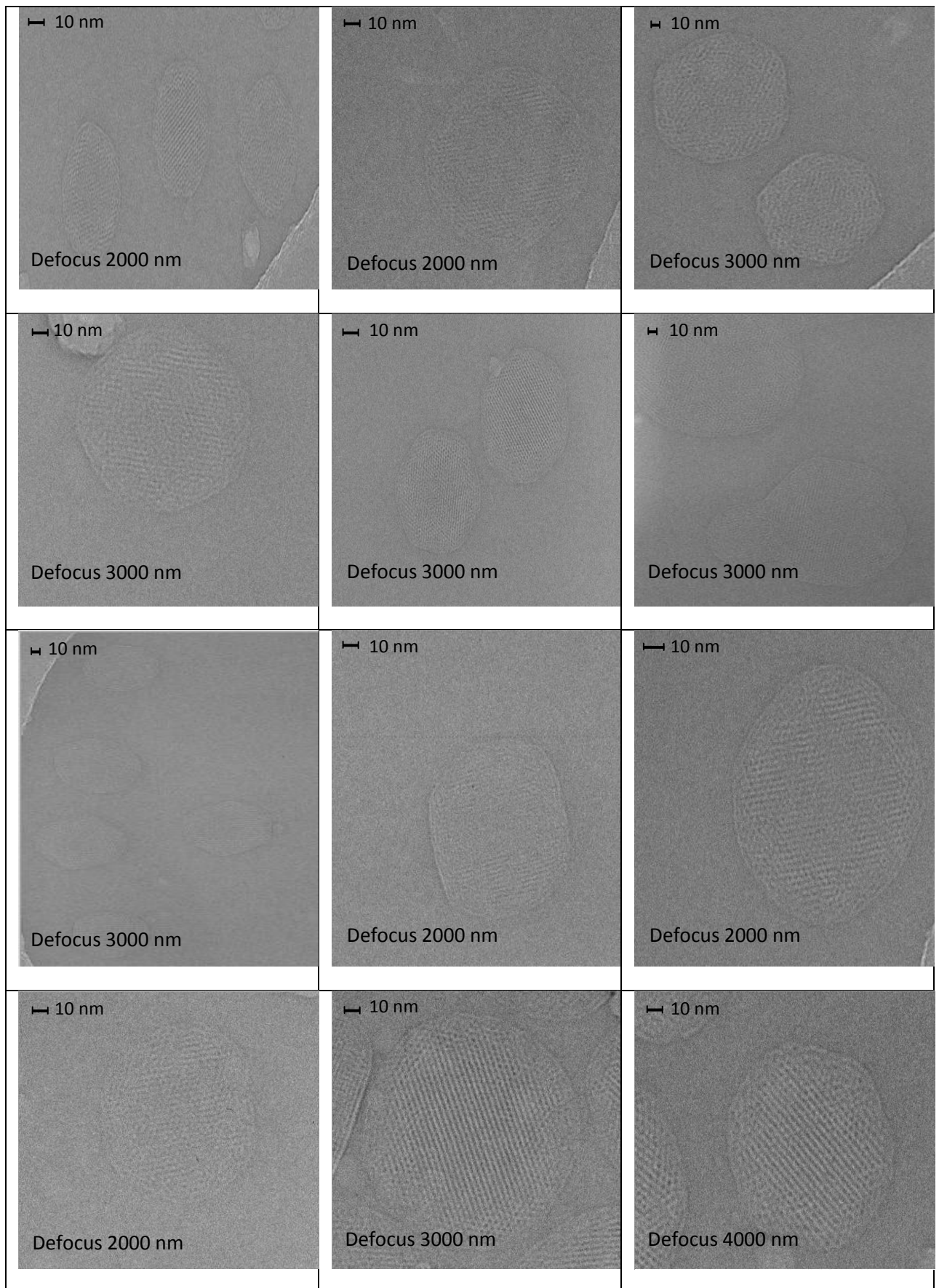
Fig. 63. Images of the cubosomes obtained by cryo-TEM. Samples were measured after one day of cryo-fixation.
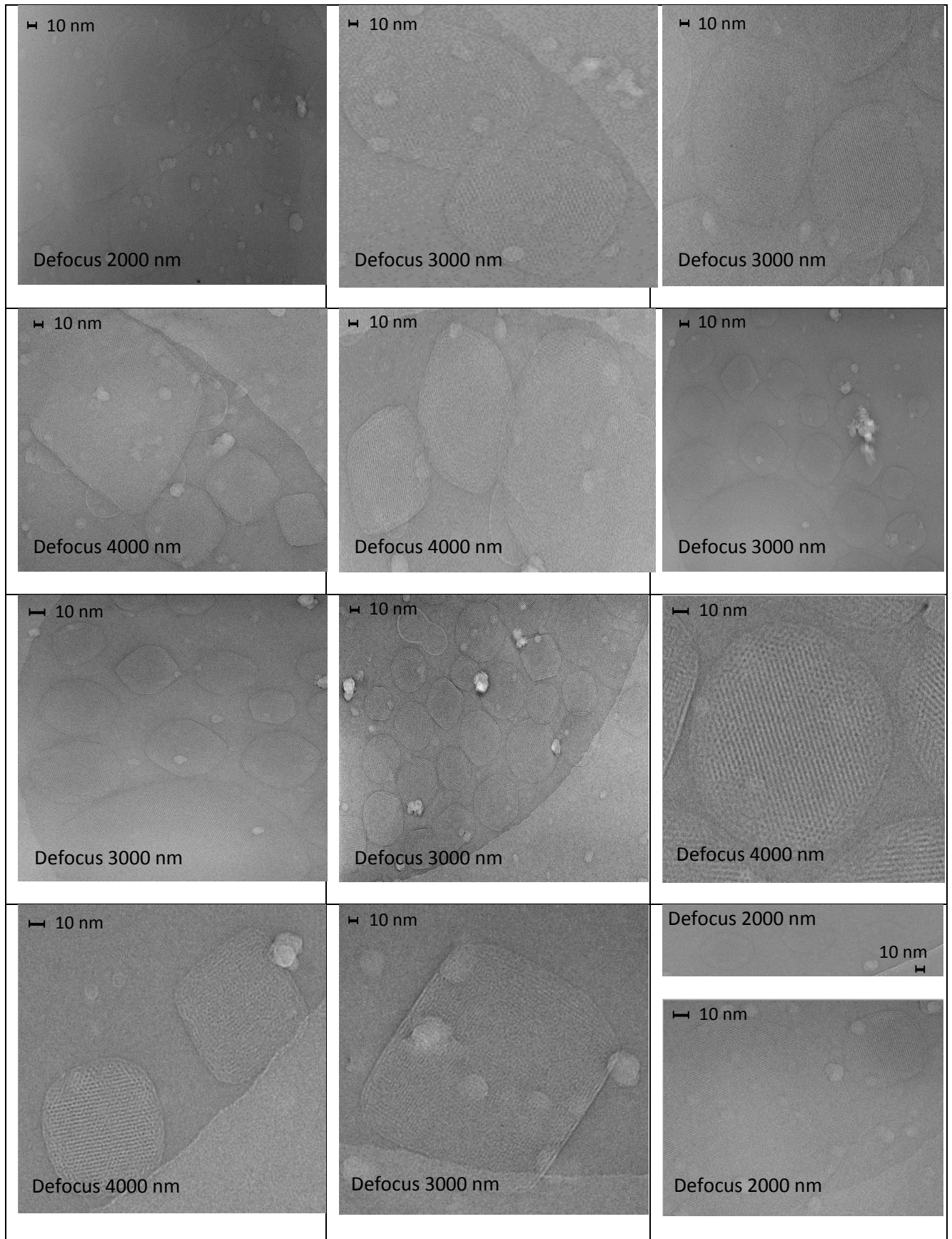
Fig. 64. Images of the cubosomes obtained by cryo-TEM. Samples were stored during one month in the fridge.

IV. Theoretical analysis of the cubosomes

Cubic liquid bicontinuous phases can be described mathematically using a nodal approximation. Structures that are created by the mixture of surfactant/oil/water or surfactant/water can be visualized by triply periodic minimal surfaces. A monolayer or a bilayer that is formed in such a mixtures can be described by a mathematical theory, in our case by means of Landau-Brazovskii functional. The cubic bicontinuous phases can be characterized by the genus, energy and the surface area of the calculated structures.

In bicontinuous liquid crystalline phases the bilayer separates the volume into two disjoint networks of channels and behaves like an elastic membrane. For a fixed topology the elastic energy of the membrane depends on the mean curvature, H, of the surface describing the center of the bilayer according to the Helfrich formula [66]:

$$F_b = 2k \int H^2 dA \qquad \text{(IV.1)}$$

where k is the bending rigidity, and dA is the infinitesimal area element. In bulk, the minimum of the functional (IV.1) corresponds to triply periodic minimal surface, because the minimal surfaces have zero mean curvature at every point. The surface with zero mean curvature has saddle-like shape at every point (except flat points). A plane is a special case of the minimal surface. The functional (IV.1) has been successfully applied to the studies of vesicles built of lipid bilayers. The agreement between experimental results and the calculations performed for different shapes of vesicles was excellent [67, 68, 69].

In physical systems triply periodic surfaces cannot extend to infinity. They have to be bounded by the walls of the vessel or by the surrounding coexisting phases. The latter case concerns for example the monocrystals of cubic phases [70], or dispersion of nanoparticles build of cubic phases in the isotropic phase [71]. Such nanoparticles are called cubosomes and may be used as nano containers for drug delivery, in a similar way as liposomes. When the bicontinuous phase coexists with an isotropic phase, its structure at the interface has to be deformed in order to avoid free edges exposed to the isotropic phase, because the free edges are mainly built of hydrocarbon chains. Due to the hydrophobic effect, the free edges

77

connect with each other and the bilayer in the bicontinuous phase forms a closed surface, where the surface is defined by the midplane of the bilayer. It is obvious that it is not possible to close the channels of the triply periodic surface with a zero mean curvature surface. The surface at the interface has to be build of the pieces of the surface with positive and negative mean curvatures. This will result in an increase of the bending energy (IV.1). The bending energy increase depends on the direction of the interface with respect to the unit cell, since the periodic bicountinuous phase is not isotropic. Unfortunately, the structure of the interface between the bicontinuous and the isotropic phases cannot be directly observed experimentally. The measurements of the surface tension for such interfaces were not yet conducted. The question of the shape and elastic energy of the surface representing the lipid bilayer at the interface between the cubic and isotropic phases remains open. It is the subject of the present study.

Most of the work devoted to the studies of nanoparticles and monocrystals of the cubic lyotropic liquid crystal is experimental [69, 70]. It has been observed in experiments that the formation of facets on a spherical droplet of the bicontinuous lyotropic liquid phase of symmetry Pn3m takes place in a well defined order. First the facet (111) is created next (100) (see Fig. 19). The order of facets formation must be related to their stability and the stability must be related to the structure of the facets, because different curvatures of the surfaces closing the free edges result in different values of the energy (IV.1). However, it is difficult to determine experimentally the structure of the facets of monocrystals of lyotropic bicontinuous phases. The size of the unit cell of the cubic bicontinuous phases is much smaller than the resolution of the optical microscopes. Since the monocrystals are soft, application of AFM techniques is also problematic. Cryo-TEM methods are the most useful so far. Unfortunately, the images obtained from cryo-TEM experiments are generated by electrons scattered through the whole sample. Thus, limited information about the structure of the surface of the sample can be inferred indirectly from cryo-TEM experiments.

The knowledge about the structure of the surface of the cubosomes and monocrystals could be obtained from appropriate theoretical calculations. So far, however, the theoretical description is restricted to purely geometrical models based on the properties of triply periodic nodal surfaces [72] and to lattice models [73, 74]. The mathematical modeling based on the nodal surfaces allows for investigation of topological properties of the studied

structures, but the shape of the bilayer and the elastic energy (IV.1) of the examined object cannot be determined. Therefore, it is necessary to use appropriate free energy models to obtain the knowledge on the shape and the excess energy of the bilayer at the interface with an isotropic phase. The surface tension for the (111) and (100) orientations for the bicontinuous phase confined by the hydrophilic walls was calculated in Ref. [71, 72] in the lattice model for different thickness of the slits. However, the surface tension in lattice models depends on the orientation of the interface with respect to the principal lattice directions even in the case of gas-liquid coexistence. For this reason it was not possible to compare the surface energies for different orientations of the cubic phase with respect to the slit walls or an interface.

We are interested in the geometry and stability of interfaces formed when the Pn3m phase is surrounded by an isotropic phase. In particular, we would like to examine the geometry of the facets formed at the droplet of the Pn3m phase. The mathematical modeling of the bicontinuous phases in terms of the functional (IV.1) is however very difficult in the presence of the interface. It requires minimization of the functional (IV.1) for functions describing the location of the bilayer. These functions are not know a priori and cannot be easily parameterized. Therefore, we decided to perform the calculations within the framework of a relatively simple Landau-Brazovskii type model with one scalar order parameter related to the local concentration of water [75, 76].

IV.1. Landau-Brazovskii functional

The free energy functional for systems inhomogeneous on the mesoscopic length can be written in the form:

$$\mathcal{F}[\phi(\mathbf{r})] = \int d^3\mathbf{r}(|\Delta\phi(\mathbf{r})|^2 + g[\phi(\mathbf{r})]|\nabla\phi(\mathbf{r})|^2 + \mathfrak{f}[\phi(\mathbf{r})]) \qquad \text{(IV.2)}$$

This functional successfully describes systems as diverse as binary or ternary mixtures, block copolymers, colloidal particles with competing attractive and repulsive interactions of different range, or magnetic systems with competing ferromagnetic and antiferromagnetic

interactions [75, 77-83]. The order parameter ф(**r**) in (IV.2) depends on the physical context. In the case of block copolymers or ternary water-surfactant-oil mixtures ф(**r**) is the local concentration difference between the polar and the nonpolar components. In the case of lipids in water ϕ^2(**r**) describes the local concentration of water. At the center of the lipid bilayer ф(**r**) = 0. The bilayer divides the space into the disjoint water channels, one of them on one side of the bilayer, where ф(**r**) > 0, and the other side of the bilayer, where ф(**r**) < 0. The sign of ф(**r**) allows to distinguish between the two disjoint channels of water. The fluid in each channel, however, has the same physical nature. For this reason in the case of lipids in water functional (IV.2) must be an even function of ф.

In the homogeneous phases the concentration of water is independent of the position. In such case ф(**r**) = const and $\nabla\phi = \Delta\phi = 0$, therefore $f[\phi]$ is the free energy density of the homogeneous phases. In the case of the phase coexistence between water - and lipid-rich phases we can postulate for $f[\phi]$ the form with three minima of equal depth, where ф = ±1 both represent the water-rich phase, $f[\phi(\mathbf{r})] = (\phi(\mathbf{r})^2 - 1)^2(\phi(\mathbf{r}))^2$. The inhomogeneous distribution of the components, in particular the formation of the bilayer, is possible when the corresponding free energy is lower than for any homogeneous structure. When the concentration ф(**r**) becomes position-dependent, then $(\nabla\phi)^2 > 0$. $\mathcal{F}$ can decrease for $(\nabla\phi)^2$ increasing from zero when $g[\phi(\mathbf{r})] < 0$. On the other hand, the Laplacian term $|\Delta\phi|^2$ leads to the incease of $\mathcal{F}$, and the length scale of the inhomogeneities (the size of the unit cell in the case of the periodic phases) is determined by the competition between the terms supporting and suppressing the special oscillations of ф(**r**). Unlike in Ref. [78-83] where $g[\phi(\mathbf{r})]$ was approximated by a constant, we assume after Ref. [75] the form $g[\phi(\boldsymbol{r})] = g_2\phi(\boldsymbol{r})^2 + g_0$.with $g_2 = 4.01 - g_0$, and $g_0 = -3$.

In the mean-field approximation the stable or metastable phases of the system correspond to the minimum of the functional (IV.2). In order to minimize the functional we discretize the field ф(**r**) on the cubic lattice (see Fig. 65).
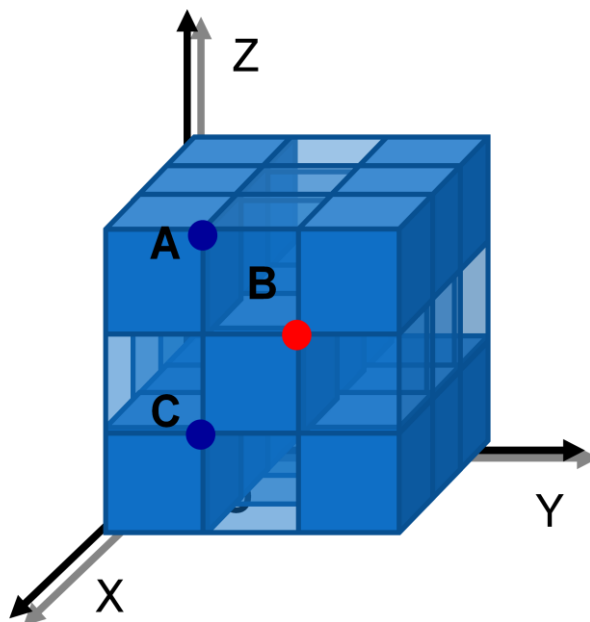
*Fig. 65. Discretization of the field ɸ(**r**) on the cubic lattice.*

After discretization, the problem of minimization of the functional is converted to the problem of minimization of the function of many variables, where the variables are the values of the field ɸ(**r**) at the lattice points. We use the conjugate gradient method to minimize the function numerically [75].

The aim of our calculation was to examine bicontinuous cubic phase in front of the hydrophilic wall. Bicontinuous triply periodic phases have been studied extensively in the last decades [75, 84], but there are almost no publications about the properties of the interface of these phases with an isotropic phase. In our work we wanted to fill this gap investigating the structure of the bicontinuous phase of D symmetry at the boundary with an isotropic phase.

IV.2. Building the initial configurations

In order to determine the structure of a given facet we assume that ɸ(**r**) is periodic in the directions parallel to it and in the perpendicular direction the cubic and the isotropic phases are present at the two sides of the facet. We chose the coordinate frame with x and y

directions parallel, and z direction normal to the facet. Periodicity in x and y directions and the assumption that at large enough distance from the facet the bulk phases are not disturbed, allows to obtain the structure of the near-surface layer of the cubic phase by translation in the x and y directions of the elementary computational cuboidal cell (Fig. 66).
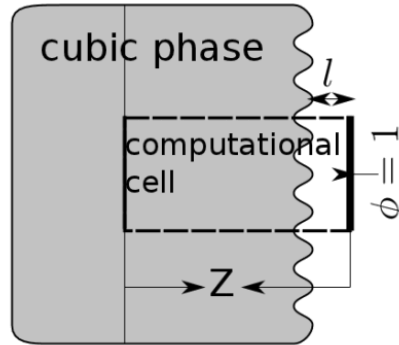
*Fig. 66. The cross-section of the computational cuboidal cell. Z is the thickness of the cell in z direction. The sizes of the cell in x and y directions depend on the orientation of the facet and are shown in Fig. 67. Periodic boundary conditions are imposed on the dashed lines. At the thin solid line ɸ(**r**) has the form obatained for the bulk phase. At the thick solid line ɸ(**r**)=1 indicate the water rich phase. l is the distance of the interface from the face of the computational cuboidal cell with ɸ(**r**)=1.*

The size of the cuboid in x and y directions is determined by the value of the unit-cell length of the bulk cubic phase and the orientation of a given facet. The sizes of the computational cells are different for each facet due to different symmetries in each case. We apply periodic boundary conditions in x and y directions and fixed boundary condition in z direction, where the field ɸ on one side of the cuboid is composed of the bulk cubic phase and on the other side it is ɸ= ±1 as in the isotropic phase. The facet is formed at the boundary with the isotropic phase, near the face of the cuboid with the boundary condition ɸ= ±1.

We used the nodal approximation (eq.IV.3) to build the initial configuration for the field ɸ(**r**) in the cuboids:

$$\psi_D(x_1, x_2, x_3) = \cos\left(\frac{2\pi}{L} \cdot x_1\right)\cos\left(\frac{2\pi}{L} \cdot x_2\right)\cos\left(\frac{2\pi}{L} \cdot x_3\right) - \sin\left(\frac{2\pi}{L} \cdot x_1\right)\sin\left(\frac{2\pi}{L} \cdot x_2\right)\sin\left(\frac{2\pi}{L} \cdot x_3\right) \text{ (IV.3)}$$

where the coordinate frame is chosen such that x_i are parallel to the edges of the cubic unit cell of the bulk phase. The linear size L of the periodic cubic element described by the nodal approximation (IV.3) is taken as the size of the unit cell of the bulk bicontinuous cubic

diamond phase, which is known from the previous calculations [75]. Such a cubic element of size L is shown in Fig. 67b.
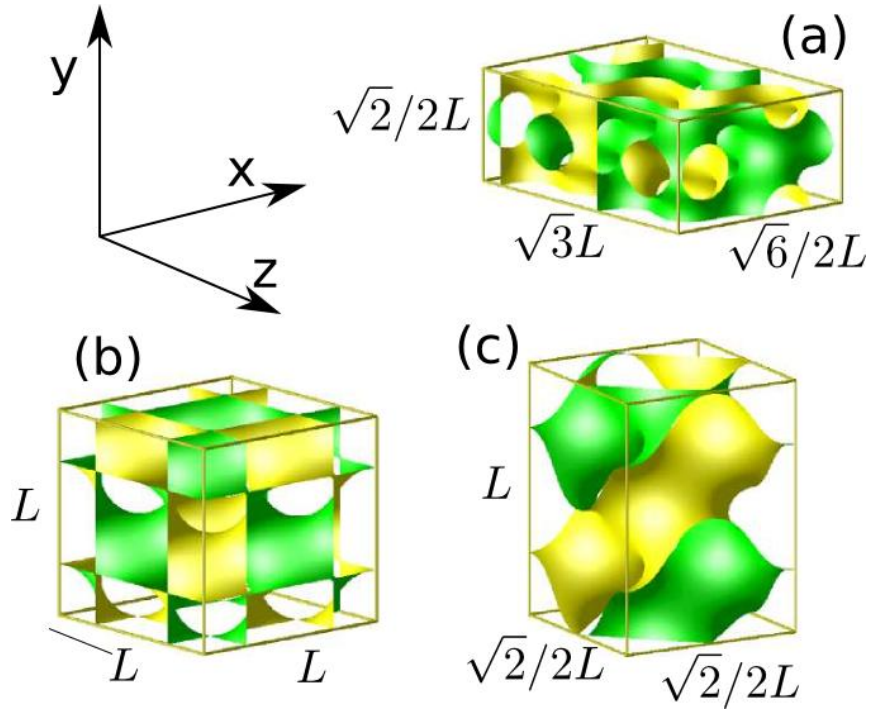
Fig. 67. Computational cells for the facets: a) (111) $\sqrt{6}/2L \times \sqrt{2}/2L \times \sqrt{3}L$, b) (100) $L \times L \times L$, c) (110) $\sqrt{2}/2L \times L \times \sqrt{2}/2L$. Green and yellow colors show different sides of the surface $\phi(\boldsymbol{r}) = 0$.

The initial configurations for all cuboids used to determine the structure of the facets perpendicular to the directions [111]. [100], and [110] are shown in Fig. 67 a, b, c, respectively.

The size of the cuboids in x and y directions is the period of the cubic phase in the corresponding direction. The size is kept constant. In z direction we consider a range of thicknesses of the cuboid, $Z_{min} < Z < Z_{max}$. We chose $Z_{max}= 8Z_{min}$ of the smallest cuboid in z direction is equal to the period of the cubic phase in this direction. Z assumes the values which are multiples of the number of grid points times the distance between the grid points. For the facets (111) x, y, and z axis in the cuboid should be indentified with $[\bar{1}01]$, $[\bar{1}2\bar{1}]$, and [111] directions, respectively. Thus, in z direction the period for (100), (110), and (111) is, $\sqrt{2}/2L$, and $\sqrt{3}L$, respectively.

The size of the cuboid, for calculating the (100) facets, in x and y direction is equal to L, and the size in z direction (normal to the facet (100)) is varied from L to 8L. x, y, and z axis in the cuboid should be identified with [100], [010], and [001] directions, respectively. The cuboidal cell cut out of the cubic phase for the calculations of (100) facet is shown in Fig. 68.
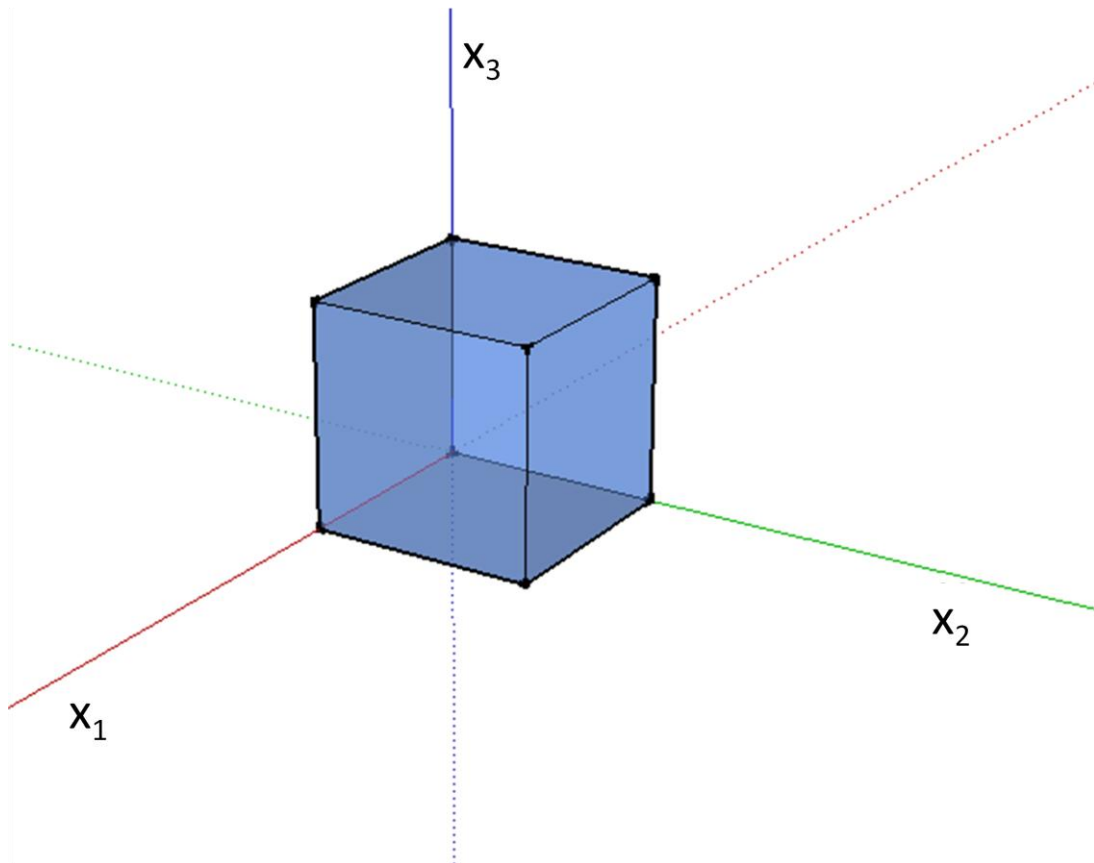
Fig. 68. Schematic representation of the cuboidal computational cell for calculations performed to investigate the structure of (100) facets.

The size of the cuboid, for calculating (110) facets, in x and y direction is equal to $\sqrt{2}L$, and L, respectively. The size in Z direction (normal to the facet (110)) is varied from $\sqrt{2}/2L$ to $8\sqrt{2}/2L$. x, y, and z axis in the cuboid should be identified with [100], [001], and [110] directions, respectively. The cuboidal cell out of the cubic phase for the calculations of (110) facet is shown in Fig. 69.
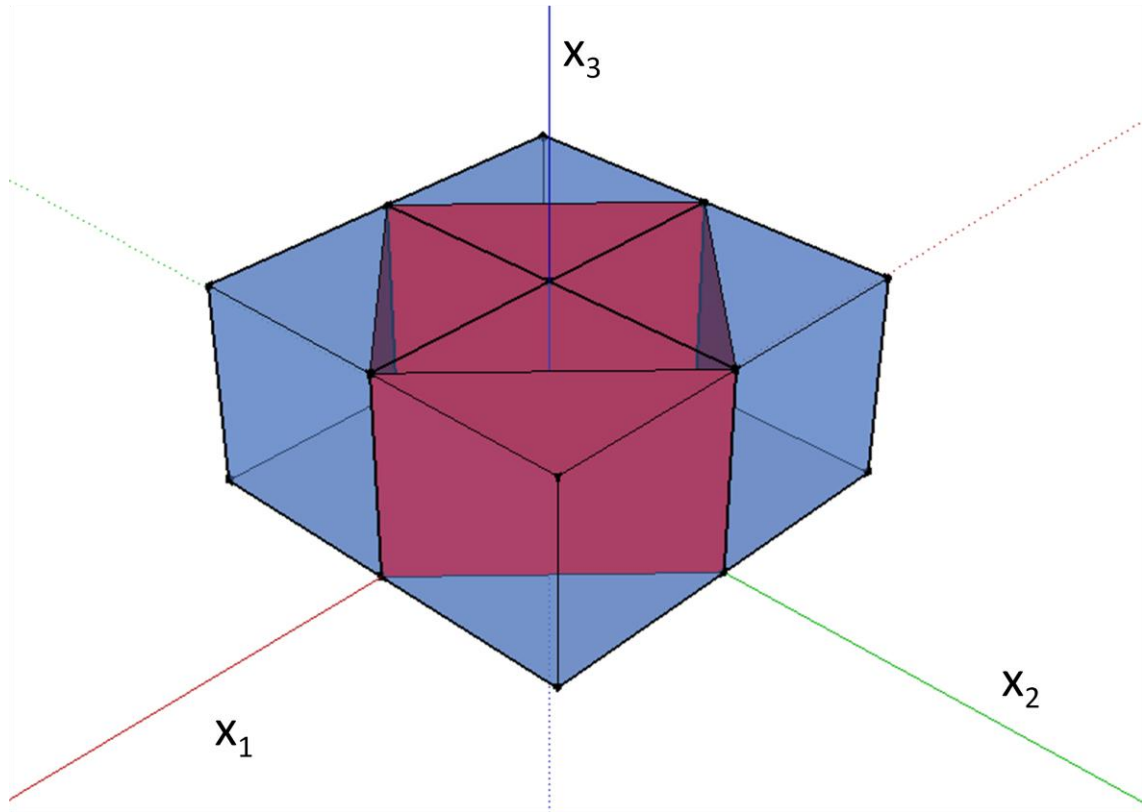
Fig. 69. Schematic representation of the cuboidal computational cell for calculations performed to investigate the structure of (110) facets.

The size of the cuboid, for calculating (111) facets. In x and y directions is equal to $\sqrt{2}/2L$ and $\sqrt{6}/2L$, respectively, while the size in z direction (normal to the facet (111)) is varied from $\sqrt{3}L$ to $8\sqrt{3}L$. The cuboidal cell cut out of the cubic phase for the calculations of (111) facet is shown in Fig. 70.
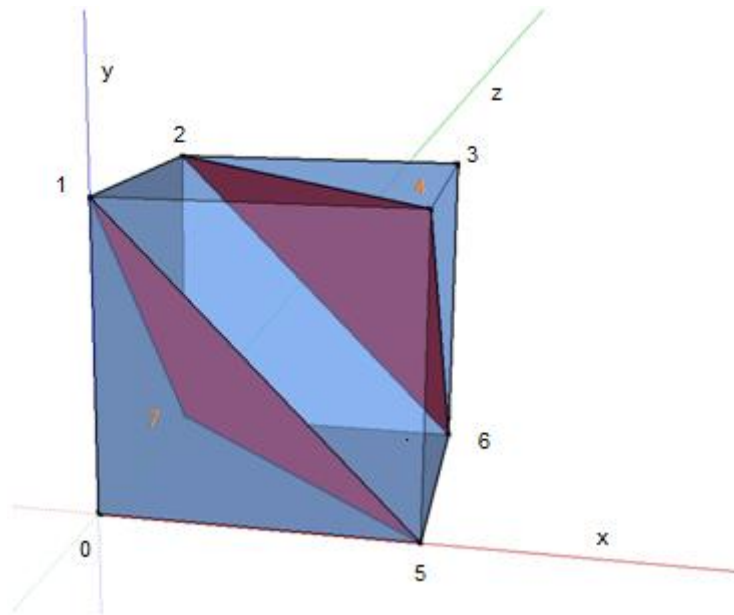
Fig. 70. Building (111) facet of the cubic phase. The triangles show the planes parallel to the surface of the (111) facet.

IV.3. Results

The functional (IV.2) is minimized with respect to $\phi(\mathbf{r})$ with the imposed boundary conditions and for a given Z, where Z is the size of the computational cell in z direction. This way a function of Z, F(Z), equal to the minimum of the functional (IV.2) for a given Z is obtained for a range of $Z_{min} < Z < Z_{max}$. F(Z) has local minima for $Z = Z_n$ with fixed distance between them $\Delta Z = Z_{n+1} - Z_n$. ΔZ depends on the orientation of the facet. Each minimum corresponds to a different topology of the layer of the cubic phase. F(Z) is the free energy under the constraint of fixed thickness Z of the computational cell. When the constraints are released the free energy assumes a minimum. We therefore indentified the structure of the facet for a given topology with the structure obtained for $Z = Z_n$. The corresponding surface describing the shape of the bilayer is given by $\phi_{Zn}(\mathbf{r})$.

Our goal was to examine the structure and the stability of the facets created at the interface between a monocrystal or a nanoparticle of the lyotropic liquid crystal phase surrounded by the isotropic phase.

IV.3.1. Facets orthogonal to the [111] direction

According to the experimental observations (see section II.2.5.1) the (111) facet are the most stable for the diamond Pn3m bicontinuous phase. This is in agreement with the results of the theoretical calculations, where the facets have been obtained by the minimization of the functional (IV.2) subject to appropriate boundary conditions.

Within the period of cuboid (see Fig. 67a) along z axis which is $\sqrt{3}L$, the facets are formed at 3 different positions when the channels of the bicontinuous phase are closed at one side of the surface composed of amphiphilic molecules given by the equation $\phi(\mathbf{r}) = 0$ (see Fig. 71 right column) and at 3 other positions when the channels of the bicontinuous phase are closed on the other side of this surface (see Fig. 71 left column).

Fig. 71. The (111) facets are formed at different thickness of the bicontinuous phase. The facets are formed when the thickness of the bicontinuous phase is increased by $\sqrt{3}/6L$. Left and right panels show the facets with closed channel at one of the two sides of of the surface $\phi(\mathbf{r}) = 0$.

The distances between the positions of adjacent facets are comparable and equal to approximately $\sqrt{3}/6L$. The formation of a new facet is related to the change of the topology of the growing nanoparticle of the monocrystal. The open channels of the (111) facets form a triangular lattice. The surface of the facet is approximately flat. Such a unique structure of the (111) facets may explain their exceptional stability.

The facets shown in Fig. 71 are obtained for different sizes of the cuboids for which the functional (IV.2) has a minimum with respect to the thickness of the cubic phase in z direction. The change of the topology is monitored by the calculations of the genus of the surface $\phi(\mathbf{r}) = 0$ contained in computational cell. The genus is obtained by calculating Euler characteristics of the surface $\phi(\mathbf{r}) = 0$ using equation (V.1) given in Mathematical formulas used in numerical calculations V.I.

For the fixed topology (the same genus) we obtained configurations for the (111) facets for which the free energy is optimized with respect to the thickness of the cubic phase in z direction. It means that when the thickness is decreased or increased from the optimal value, the free energy increases.

In Fig. 72 we plot the values of the free energy for the (111) facets as the function of the thickness of the cuboid F(Z). We also show the Helfrich free energy calculated for $\phi(\mathbf{r}) = 0$ for the configurations obtained by minimization of the functional (IV.2). It is interesting to note that the positions of the minima are approximately the same for the calculations performed for the functional (IV.2) and (IV.1). Thus, we can speculate that the shapes of the facets obtained by direct minimization of the functional (IV.1) would be very similar to the shapes obtained by direct minimization of the functional (IV.2). It has to be noted that minimization of the functional (IV.1) is much more difficult since the parametrization of the surface of a cubic phase is practically impossible.
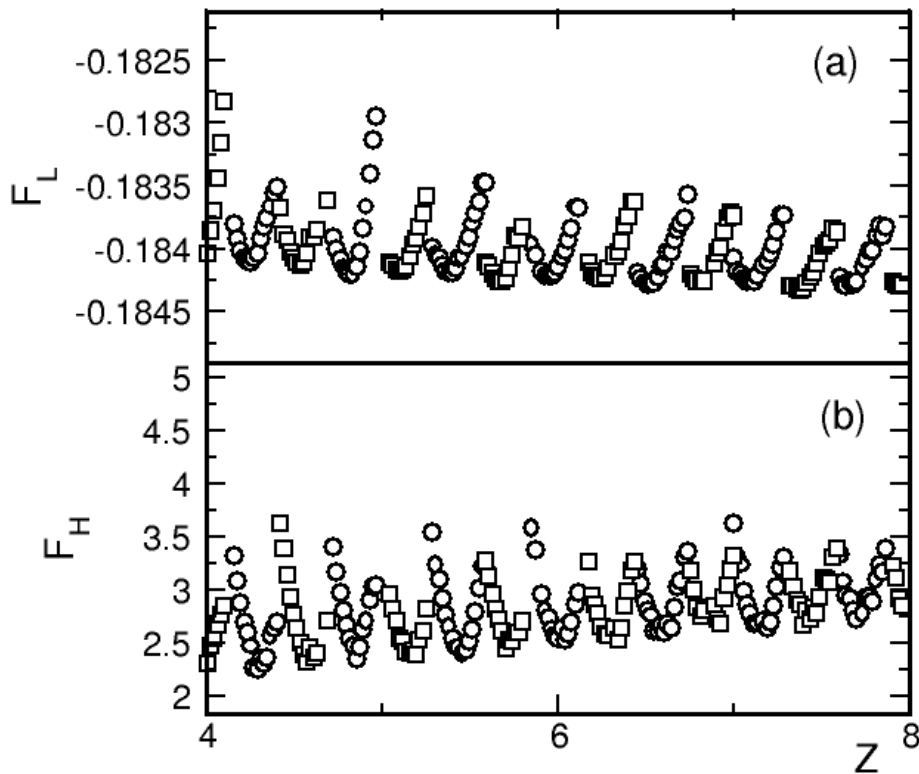
Fig. 72. (a) The Landau-Brazovskii free energy per unit volume as a function of the thickness of the cuboid (Z). (b) The Helfrich free energy per surface area of the plane parallel to the facet as a function of the thickness of the cuboid (Z). The distance on horizontal axis is given in units $\sqrt{3}L$, which is the period of the cuboid in z direction. The circles and the squares denote the configurations with the open channels on one or the other side of the surface $\phi(\mathbf{r}) = 0$.

IV.3.2. Facets orthogonal to the [100] directions

The (100) facets are formed at four different positions within the period of the cuboid L in z direction. The subsequent facets are separated by the distance L/4. When the new facets is formed the topology is changed. The shapes of the facets are for the thickness of the cubic phase in the range from z to z+L are presented in Fig. 73. Unlike, in the case of (111) facets, at the same thickness of the bicontinuous phase, two different facets may be formed when the channels are closed on one or another side of the surface formed by amphiphilic molecules $\phi(\mathbf{r})$ = 0. These facets are structurally and energetically the same. The configuration in the left and right columns are obtained when the channels are closed on

89

green side or yellow side of the surface $\phi(\mathbf{r}) = 0$. At each row the configurations obtained for the same thickness of the cubic phase are presented.

It is interesting to note that for (100) facets we can obtain two structures of the facets for a given fixed topology. They are stable and have similar energies. The shapes of the facets are shown in Fig. 74. When the facets are formed, the structure of the bicontinuous phase is deformed. Amphiphilic molecules in bulk bicontinuous phase form a surface which is identical with a triply periodic minimal surface. Such configuration has the lowest energy. At the boundary with the isotropic phase, the triply periodic minimal surface has to be deformed in order to avoid configurations with free edges exposed to the isotropic phase.
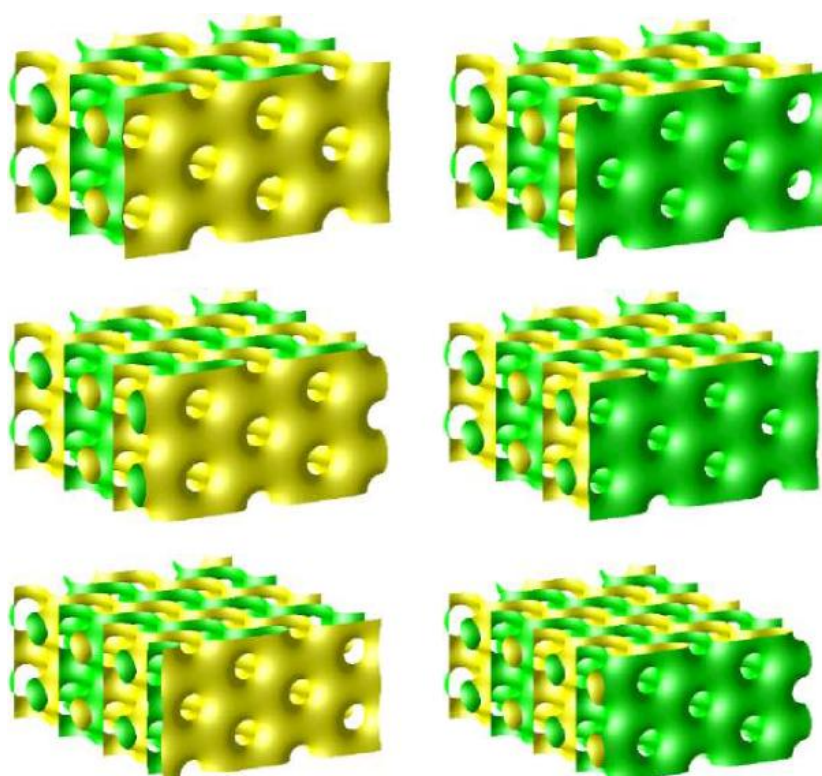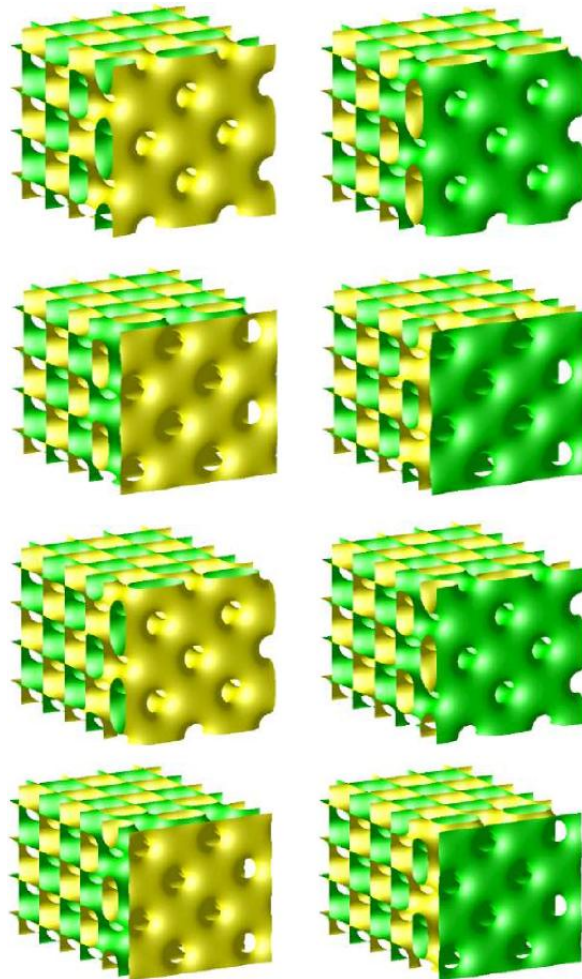

Fig. 73. The (100) facets are formed at different thickness of the bicontinuous phase. The facets are formed when the thickness of the bicontinuous phase is increased by 1/4L. Left and right panels show the facets with closed channel at one of the two sides of the surface $\phi(\mathbf{r}) = 0$.

The interior of the crystal of bicontinuous phase can be deformed to a different degree and this deformation depends on the structure at the boundary. If the structure of the facet at the boundary is such that its energy is optimized then the bicontinuous phase is deformed more away from the boundary. However, it is also possible to avoid large deformations of the bicontinuous phase. In such a case the energy of the facets is not optimized. This leads to two kinds of facets which are presented in Fig. 74. The first one of those facets is formed when the channels which are closed, form cylindrical bulges directed along the diagonal of the computational cell (right panel). The second configuration (left panel) is appropriately flat with the open channels forming a square lattice of holes as presented in Fig. 74.
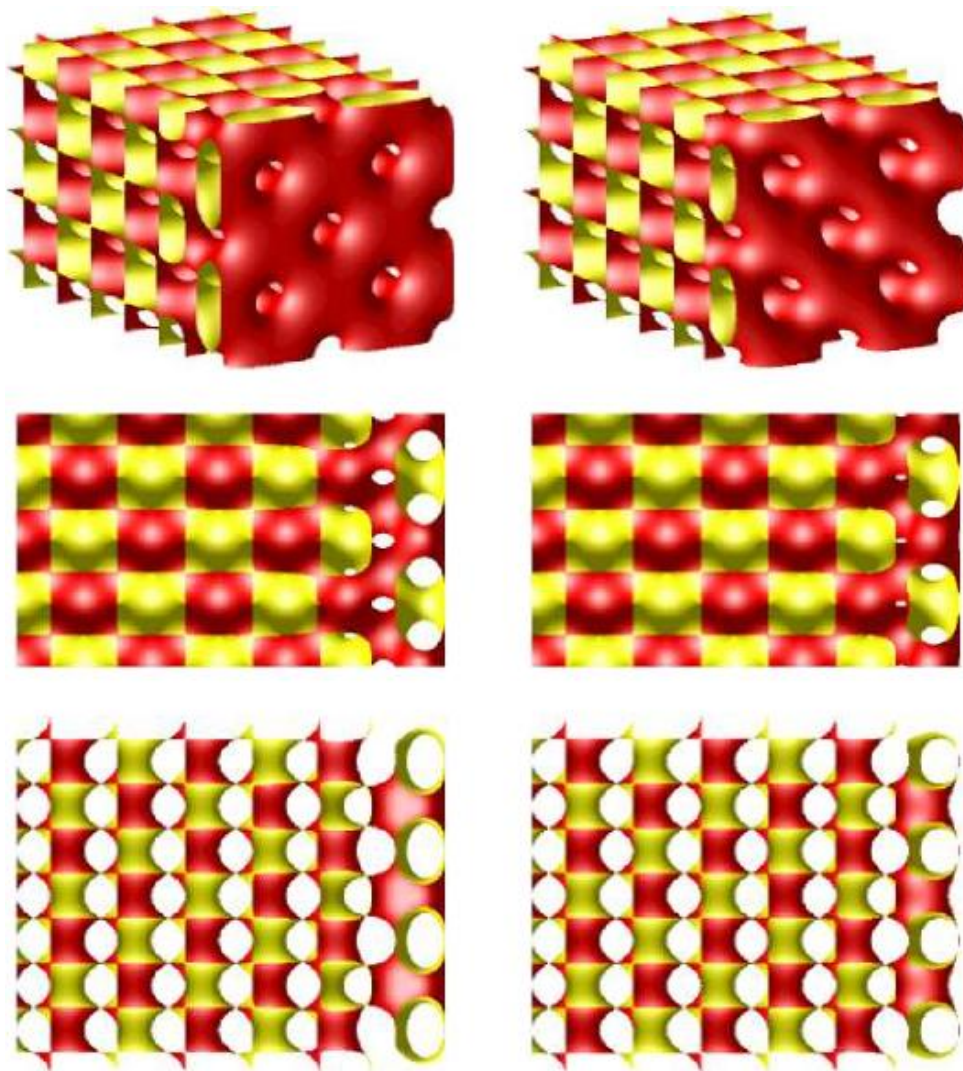
Fig. 74. Two types of (100) facets. Left and right panels show the facets formed when the bicontinuous phase is deformed more and less by the creation of the facet.

The structure of (100) facets were studied in a lattice model [74, 85]. Only the structure with the bulges along the diagonal of the cubic cell was obtained in those calculations. This is because in the lattice model only a few lattice points from the cubic cell. In the continuous model, the order parameter field is discretized on a large grid. Thus, the results of calculations can describe the structure of the facets more accurately.

IV.3.3. Facets orthogonal to the [110] direction

In the case of the (110) facet, two configurations with different topology can be distinguished within the period of the cuboid along z axis. In Fig. 75 we show the configurations with the lowest energy for the set of configuration with the same topology. The (110) facets are formed when the thickness of the bicontinuous phase increases by $\sqrt{2}/4L$. The open channels of (110) facets are arranged in the triangular lattice for the optimal configurations.
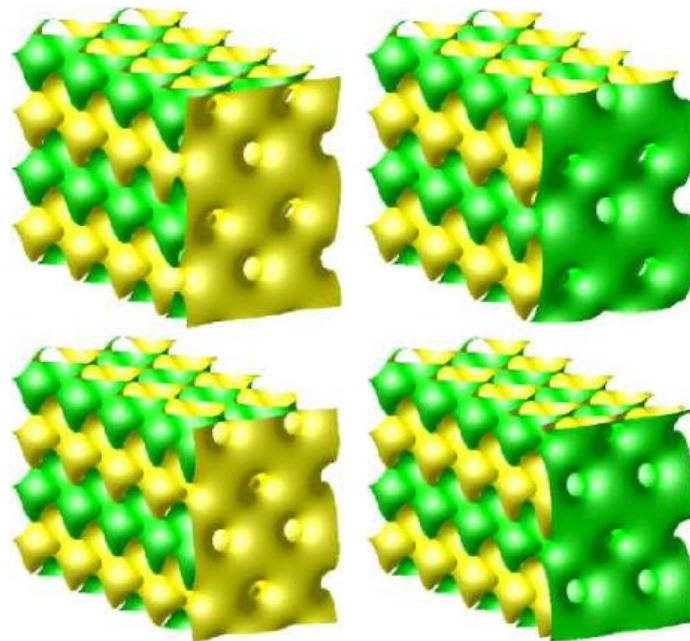
Fig. 75. The (110) facets are formed at different thickness of the bicontinuous phase. The facets are formed when the thickness of the bicontinuous phase is increased by $\sqrt{2}/4L$. Left and right panels show the facets with closed channel at one of the two sides of the surface $\phi(\mathbf{r})$=0.

This is very similar to the configurations obtained for (111) facets. The difference between these two types of facets is manifested when the thickness of the cubic phase is not optimal. In the case of (111) facets the open channels are still arranged in a triangular lattice, but for (110) facets this triangular order is no longer present. In Fig. 76 right column shows the configuration for (110) facet with the open channels arranged in a triangular lattice and left column shows the configuration without triangular order. The configurations with triangular arrangements of the open channels are more flat than the one without the triangular order. However, they are less flat than the configurations obtained for (111) facets. Only one of these configurations is stable for a given thickness of the facet. For a fixed topology the more stable configuration is the one with more flat facets as shown in Fig. 76.

In the case of (111) and (100) facets the channels are parallel and perpendicular to the [111] and [100] directions, respectively. In the case of (110) facet the channels are at an angle to the [110] direction. The formation of a flat facet should be easiest for the [111] direction since it is enough to connect the channels with an approximately planar surface and the triply periodic surface can be deformed at the connection. The formation of (100) facet should be more difficult since the channels should be closed by a semi cylindrical surface. In the case of (110) facet the adjacent channel are directed at a certain angle. Therefore, the formation of a flat surface will require larger deformation of the triply periodic surface near the facet, as shown in Fig. 76.

93
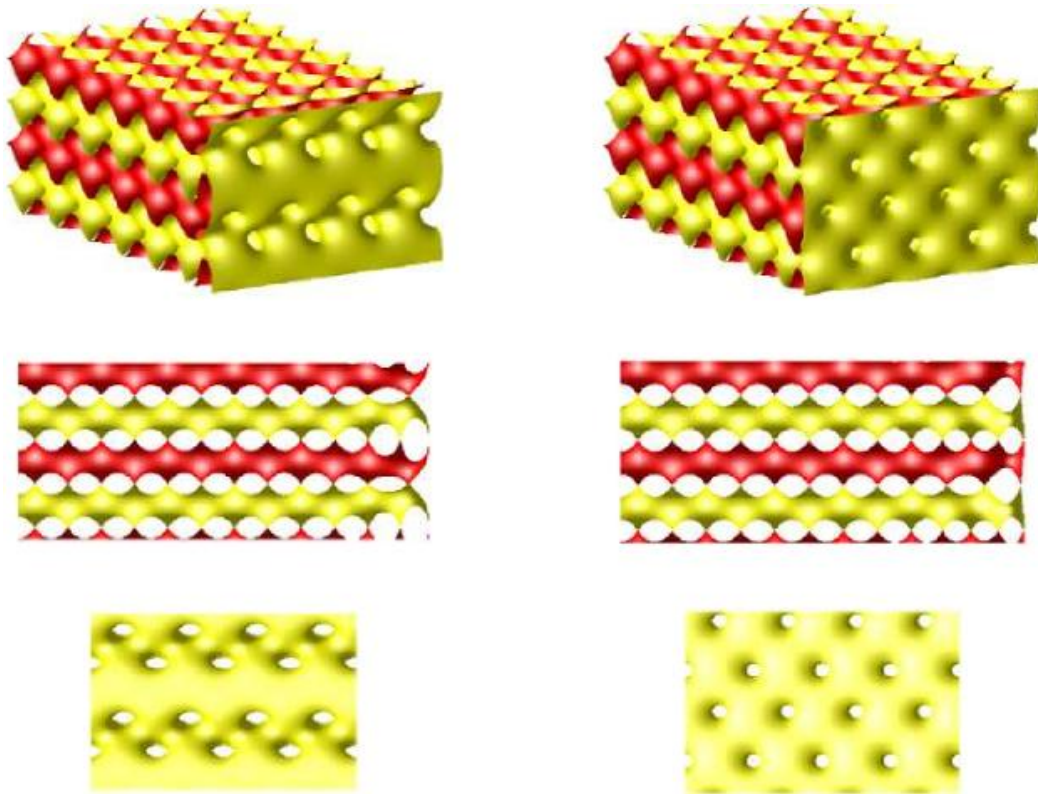
Fig. 76. Two types of (110) facets. Left and right panels show zigzag and flat facets, respectively.

IV.3.4. Stability for different directions

We have analyzed the stability of the facets by calculating also the bending energy F_b per surface area for the surface $\phi(\mathbf{r}) = 0$ contained inside the computational cell. The configurations with the lowest energy are the same both when the energy is calculated from the functional (IV.2) where the field $\phi(\mathbf{r})$ is taken into account and when the energy is calculated from the functional (IV.1) where only the shape of the surface $\phi(\mathbf{r}) = 0$ is considered. Thus, we can safely restrict the analysis of the data obtained from minimization of the functional (IV.2) to the surface $\phi(\mathbf{r}) = 0$. In an ideal situation the mean curvature of a triply periodic minimal surface should be zero at every point. In practice in numerical calculations the mean curvature is very close to zero. The formation of the facets deforms the triply periodic minimal surface. This deformation and thus deviation of the mean curvature from the optimal value is the largest in the vicinity of the facet. When analyzing the values of the local mean curvature on a surface $\phi(\mathbf{r}) = 0$ we observed that the

deformation of the triply periodic minimal surface due to formation of the facets propagates inside the cubic phase up to the distance of one, two unit cell length L. (The mean curvature was computed from the field ɸ($\mathbf{r}$) using the equation Eq. V.3 given in the Mathematical formulas used in numerical calculations) This suggests that the cubic phase inside a monocrystal (cubosome) is significantly deformed only near its boundary with an isotropic phase. We can try to define a specific "surface (interfacial) energy" associated with this deformation. The deformation should be different for different facets since the cubic phase is anisotropic. We can suspect that the stability of different facets may be related to different surface energies for different facets. We have estimated and compared the energies of formation of different facets by calculating the bending energy (IV.1) for the same size of the cuboids in z direction and dividing it by the surface area of the computational cell in x-y plane. Such energy was the smallest for (111) facets and the biggest for (110) facets. This is in agreement with the results of the experiments in which (111) facets are the most stable. Moreover, the difference in energy between (111) and (100) facets is larger than the difference in energy between (100) and (110) facets.

The better stability of more flat facets may be explained by considering the mean curvatures of the surface ɸ($\mathbf{r}$) = 0. Both a plane and a triply periodic minimal surface have zero mean curvature at every point. Thus, in order to minimize the functional (IV.1) it would be the best if the surface ɸ($\mathbf{r}$) = 0 were built mainly of planar and triply periodic minimal surfaces. Unfortunately, "gluing" these two surfaces results in their deformations. From our calculations it follows that these deformations are the largest for (110) facets and the smallest for (111) facets.

IV. 4. Cubosomes

Using Landau-Brazovskii functional it is hard to perform calculations for cubosomes of the 'natural' sizes of about 100 nm. However, it is possible to calculate small cubosomes of about 0,001 % of the size of the experimentally observed ones. In the Figs. 77-86 we present the calculated structures of these nanoparticles. These structures can be helpful in understanding the internal structure of the cubosomes. In section IV.4 the formation of different facets of diamond phase using Landau-Brazovskii functional is described. In those

calculations we have determined how the internal structure of the cubosomes may be influenced by the existence of the facets. However, the shape and the internal structure of cubosomes depend not only on the structure of the facets. It is also important how the facets are connected with each other and what is the shape of the cubosomes. The calculations performed for small cubosomes may help to answer these questions.

The most simple particle that we obtained in our calculations is shown in Fig. 77.
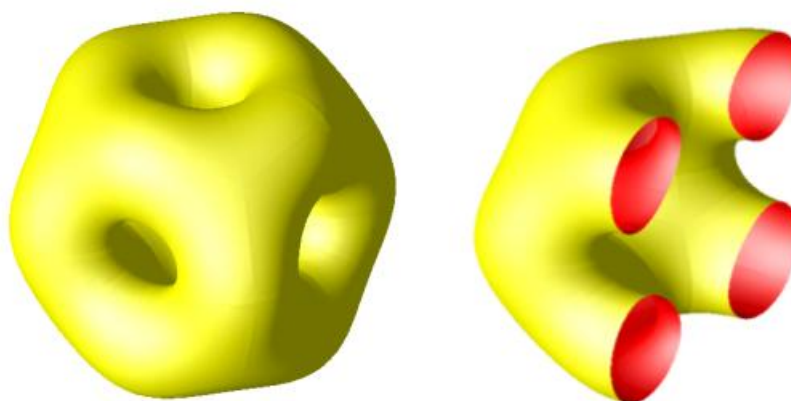
Fig. 77. Cubosome with genus 5 calculated by minimization of the functional (IV.2).

In Figs. 78-81 cubosomes have cubic shape with four holes in each face of the cube. It is interesting to note that the cubosomes which look seemingly the same may have quite different internal structure. It has been shown [75] that there may exist different bicontinuous cubic structures characterized by the same symmetries but different topology. Here, we have found analogous phenomenon, the existence of cubosomes with the same symmetries, very similar shapes but different internal structure. The examples of such cubosomes are presented in Figs. 78-81. These cubosomes have four open channels on each facet. Without knowing their internal structure we could incorrectly guess that they are the same. In fact, each cubosome is substantially different from other cubosome. We have calculated genera for all the structures to be able to express those topological differences in a more quantitative way. For the cubosomes with four open channels at the walls (Figs. 78-81) the genus can differ quite substantially from 16 to 33. The existence of the structures with those extreme values of the genus is quite surprising. In the first case (genus 16) the interior of the cubosome is deformed, in the second case (genus 33) the walls of the cubosomes seem to be not compatible with the interior of the cubosome. It is also

interesting to note that there may exist cubosomes with the same topology, but substantially different shape. Such cubosomes are shown in Fig. 83 and Fig. 84. Both cubosome have the same genus which is equal 46.
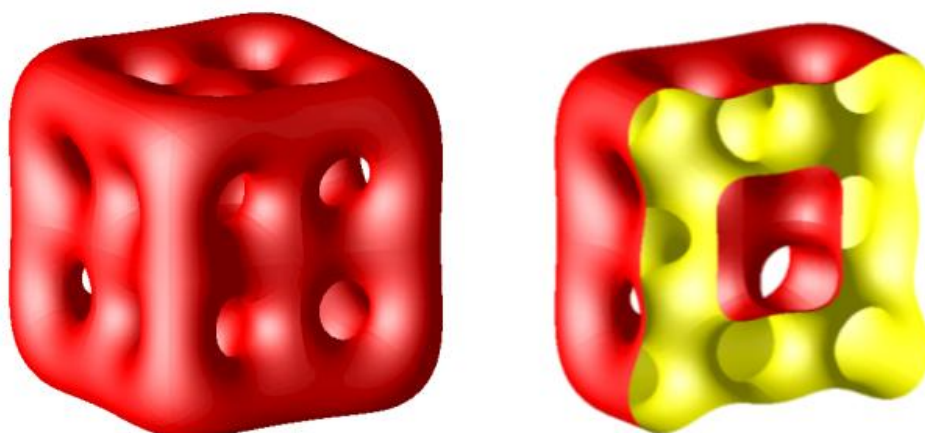
Fig. 78. Cubosome with genus 23 calculated by minimization of the functional (IV.2).
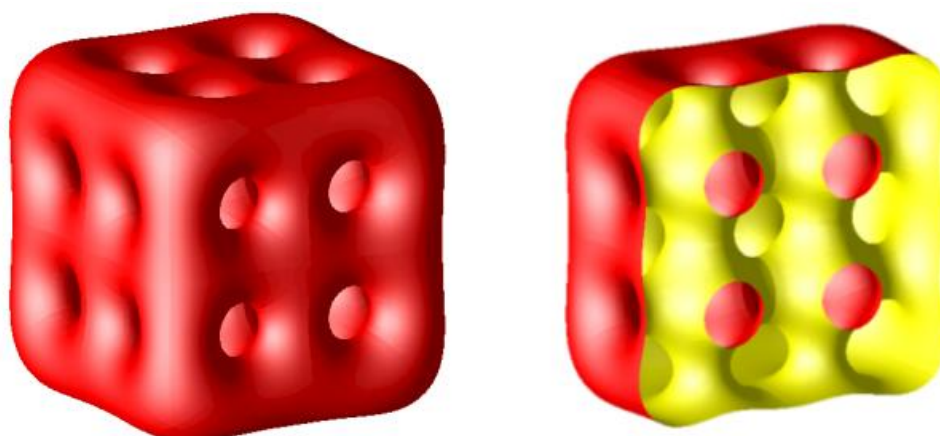
Fig. 79. Cubosome with genus 28 calculated by minimization of the functional (IV.2).
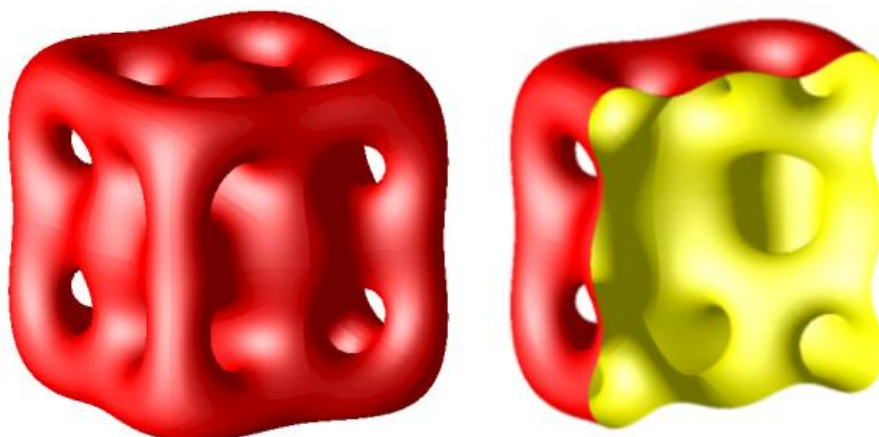
Fig. 80. Cubosome with genus 16 calculated by minimization of the functional (IV.2).
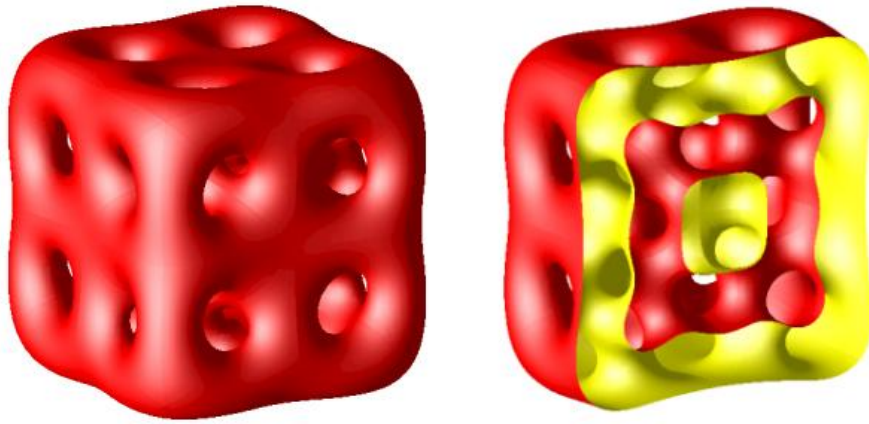
Fig. 81. Cubosome with genus 33 calculated by minimization of the functional (IV.2).
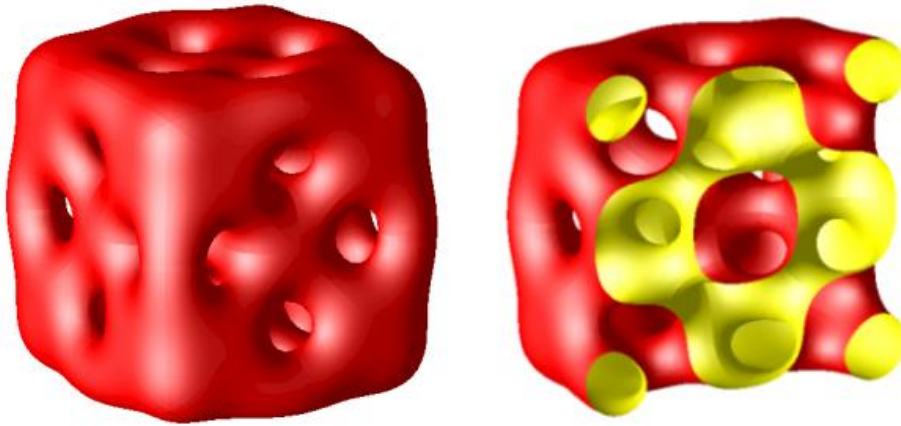
Fig. 82. Cubosome with genus 46 calculated by minimization of the functional (IV.2).
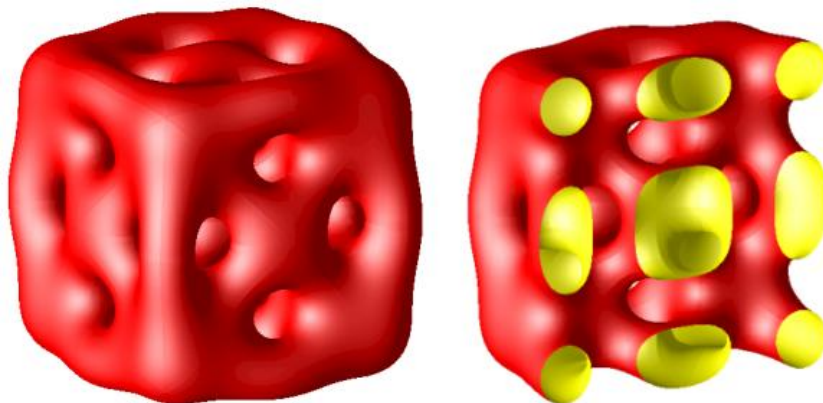
Fig. 83. Cubosome with genus 46 calculated by minimization of the functional (IV.2).
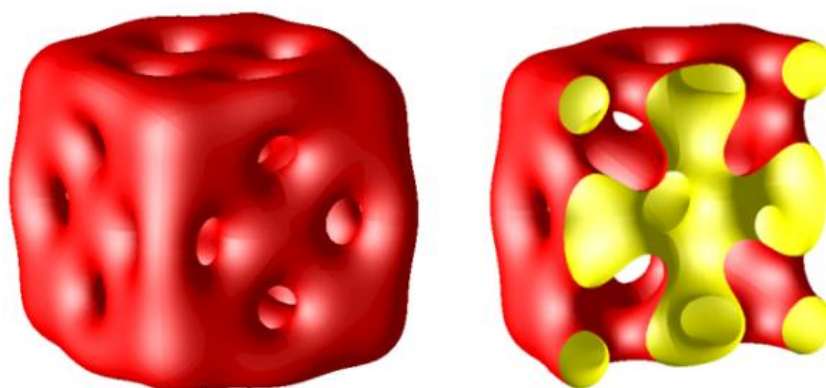
Fig. 84. Cubosome with genus 28 calculated by minimization of the functional (IV.2).
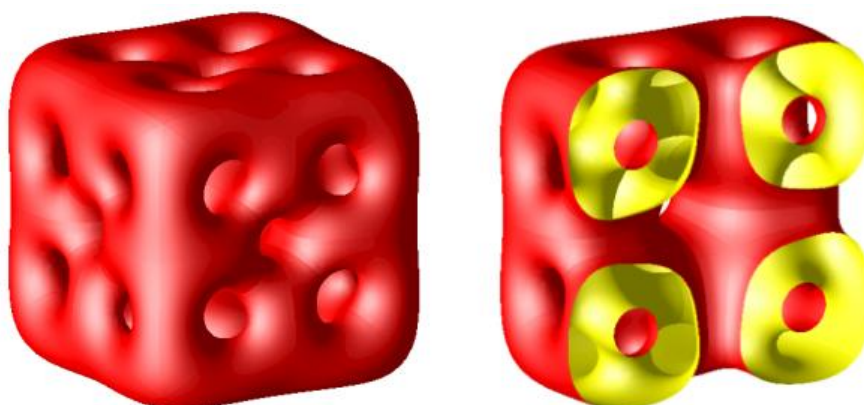
Fig. 85. Cubosome with genus 30 calculated by minimization of the functional (IV.2).
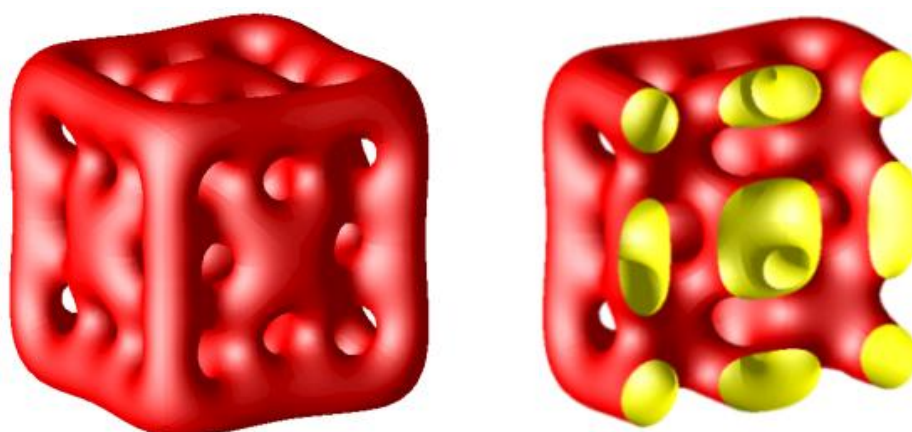
Fig. 86. Cubosome with genus 59 calculated by minimization of the functional (IV.2).

V. Mathematical formulas used in numerical calculations

V.1 Euler characteristics, genus

The order parameter field $\phi(\mathbf{r})$ carries enormous amount of information about the local structure of the phases we have investigated. The most interesting is the topology of the phases, described by the surface $\phi(\mathbf{r}) = 0$, dividing positive and negative regions of the order parameter field. Thus it was crucial in our studies to find the location of the surface $\phi(\mathbf{r}) = 0$. We use simplified version [75] of marching cubes algorithm [86] to determine the location of the surface $\phi(\mathbf{r}) = 0$. In our analysis of the investigated structures the surface $\phi(\mathbf{r}) = 0$ is represented as a set of connected triangles.

The triangulated surface is used to calculate the Euler characteristics, χ, of the surface inside the computational cell. The calculation of χ can be done according to the Euler formula $\chi = F + V - E$, where *F, V, E* is the number of faces (*F*), vertices (*V*), and edges (*E*) of the polygons cut out by the surface $\phi(\mathbf{r}) = 0$ in the small cubes of dimension of lattice spacing.

The Euler characteristic for the closed surface is related to the Gaussian (K) curvature and genus (g) of this surface in the following way [87, 88]

$$\chi = \frac{1}{2\pi} \int_S K dS = 2(1 - g), \qquad (V.1)$$

where the integral is taken over the surface S. Genus is an integer number and tells how many holes are in a closed surface. For example the genus for a sphere is zero, for a torus is one and for a pretzel is two. The structures we have investigated are infinite and periodic. The genus for an infinite surfaces is infinite, of course, but for a finite piece of this surface, in a cell, is finite and characterizes the surface. Due to periodicity the cuboidal computational cells can be treated as a closed surface in four dimensions, making calculation of genus unambiguous [89]. Therefore the genera of the structures inside the cuboids can be calculated according to: $g = 1 - \frac{\chi}{2}$, where χ was the Euler characteristics for the surface inside a computational cell. We calculate the genera for the structures just to detect topological changes.

V.2. Curvatures

The Gaussian and the mean curvatures present another characteristics of the internal surfaces given by $\phi(\mathbf{r}) = 0$. In the description of the model we have mentioned that some of the structures in the model should be characterized by zero mean curvature at every point of the internal interface. Here we present the method used to compute Gaussian and mean curvatures. The unit normal $\mathbf{n}(\mathbf{r})$ at the point $\mathbf{r}$ is given by the gradient of the field $\phi(\mathbf{r})$ at the surface $\phi(\mathbf{r}) = 0$:

$$\mathbf{n}(\mathbf{r}) = \frac{\nabla\phi(\mathbf{r})}{|\nabla\phi(\mathbf{r})|} \qquad (V.2)$$

The mean (H) curvature is given by the divergence of the unit vector [74], normal to the surface at the point $\mathbf{r}$, $\mathbf{n}(\mathbf{r})$

$$2H(\mathbf{r}) = -\nabla \cdot \mathbf{n}(\mathbf{r}) \qquad (V.3)$$

and the Gaussian curvature (K) by the formula [75, 76, 77]

$$2K(\mathbf{r}) = n(\mathbf{r}) \cdot \nabla^2 n(\mathbf{r}) + [\nabla \cdot n(\mathbf{r})]^2 + [\nabla \times n(\mathbf{r})]^2 \qquad (V.4)$$

In numerical calculation of the curvatures we used the following formulas [74, 90, 91]:

$$H = -\frac{1}{2\sqrt{\phi_x^2 + \phi_y^2 + \phi_z^2}} \frac{B}{A} \qquad (V.5)$$

$$K = \frac{1}{\phi_x^2 + \phi_y^2 + \phi_z^2} \frac{C}{A} \qquad (V.6)$$

Where A, B, and C are obtained from:

101

$$\det \begin{pmatrix} (\phi_{xx} - \lambda) & \phi_{xy} & \phi_{xz} & \phi_x \\ \phi_{yx} & (\phi_{yy} - \lambda) & \phi_{yz} & \phi_y \\ \phi_{zx} & \phi_{zy} & (\phi_{zz} - \lambda) & \phi_z \\ \phi_x & \phi_y & \phi_z & 0 \end{pmatrix} = A\lambda^2 + B\lambda + C \tag{V.7}$$

and are given by:

$$A = -\left(\phi_x^2 + \phi_y^2 + \phi_z^2\right) \tag{V.8}$$

$$B = \phi_x^2\left(\phi_{yy} + \phi_{zz}\right) + \phi_y^2\left(\phi_{xx} + \phi_{zz}\right) + \phi_z^2\left(\phi_{xx} + \phi_{yy}\right) - 2\phi_x\phi_y\phi_{xy} \\ - 2\phi_x\phi_z\phi_{xz} - 2\phi_y\phi_z\phi_{yz} \tag{V.9}$$

$$C = \phi_x^2\left(\phi_{yz}^2 - \phi_{yy}\phi_{zz}\right) + \phi_y^2\left(\phi_{xz}^2 - \phi_{xx}\phi_{zz}\right) + \phi_z^2\left(\phi_{xy}^2 - \phi_{xx}\phi_{yy}\right) \\ + 2\phi_x\phi_z\left(\phi_{xz}\phi_{yy} - \phi_{xy}\phi_{yz}\right) + 2\phi_x\phi_y\left(\phi_{xy}\phi_{zz} - \phi_{xz}\phi_{yz}\right) \\ + 2\phi_y\phi_z\left(\phi_{yz}\phi_{xx} - \phi_{xy}\phi_{xz}\right) \tag{V.10}$$

The mean and Gaussian curvatures have to be computed at the points of the surface $\phi(\mathbf{r}) = 0$. The derivatives of the field $\phi(\mathbf{r})$ at the point $\mathbf{r}_0$, for which $\phi(\mathbf{r}_0) = 0$, according to the formulas (V.8), (V.9), (V.10).

V.3. Discretization of derivatives

The fist and the second derivatives in the gradient and Laplasian term of the functional (IV.2) at the point **r** = (i, j, k) h on the lattice were calculated according to the following formulas [86]

$$\frac{\partial \phi(\mathbf{r})}{\partial x} \rightarrow \frac{\phi_{i+1,j,k} - \phi_{i-1,j,k}}{2h}, \tag{V.11}$$

and

$$\frac{\partial^2 \phi(\mathbf{r})}{\partial x^2} \rightarrow \frac{1}{12h^2} \left(-\phi_{i+2,j,k} + 16\phi_{i+1,j,k} - 30\phi_{i,j,k} + 16\phi_{i-1,j,k} - \phi_{i-2,j,k} \right), \tag{V.12}$$

and similar in y and z directions.

The mixed derivatives are calculated [90] according to

$$\frac{\partial^2 \phi(\mathbf{r})}{\partial x \, \partial y} \rightarrow -\frac{1}{2h^2} \left(\phi_{i+1,j,k} + \phi_{i-1,j,k} + \phi_{i,j+1,k} + \phi_{i,j-1,k} - 2\phi_{i,j,k} - \phi_{i+1,j+1,k} \right. \tag{V.13}$$
$$\left. - \phi_{i-1,j-1,k} \right).$$

Moreover, the calculation of derivatives on the lattice boundary requires taking into account the points outside the lattice. These points are given by appropriate boundary conditions.

VI. Conclusions

The **experimental part** of our work had two aims: 1 - investigation of the phase diagram of the lyotropic system used for production of cubosomes, 2 - production of cubosomes and their observation by means of a transmission electron microscope (TEM).

The starting point of our experimental research was the phase diagram of the phytantriol/water/ethanol ternary system established previously by R. Sheshka and P.Faye (students on M1 practice in the LPS lab). We reexamined this phase diagram in much more details using a new experimental setup tailored for an automated and accurate control of the ethanol concentration. This new investigation of the phytantriol/water/ethanol phase diagram led to several discoveries:

1 - We have found that the addition of ethanol in adequate concentrations to the L1 phase surrounding our samples (droplets of phytantriol) induces the L3 (sponge) and Lα (lamellar) phases beside the already known L2, Pn3m and H1 phases.

2 - The corrected phase diagram Temperature-vs-ethanol concentration has several remarkable features such as the line of phase coexistence of three isotropic phases (L1+L2+L3) limited by two quadruple points (L1+L2+L3+H1 and L1+L2+L3+Pn3m). To the best of our knowledge the existence of the quadruple points was not reported in the literature so far. Moreover the phase coexistence of three isotropic phases is a unique result presented only in our work.

3 - The phenomenon of the nucleation of L1 inclusions in the Pn3m phase was reported in previous studies [70] but only in our work the explanation of this phenomenon was given.

4 - The sequence of phase transition Pn3m+L1 $\rightarrow$ L3+L1 $\rightarrow$ Lα+L1 $\rightarrow$ L1+L2 was detected for the first time (Fig. 27).

We attempted also to elaborate a novel method of preparation of dispersed nanoparticles of the liquid crystalline Pn3m phase. Our aim was to prepare cubosomes in a more controlled way than it was done in all known methods used previously. Unfortunately, our attempts to

104

generate nanoparticles of the liquid crystalline phase without using any stabilizing agent was unsuccessful: as expected the nanoparticles were generated but their dispersion was unstable : nanoparticles of the Pn3m phase quickly stuck together. We concluded that the role of stabilizing agent was crucial in preparation of cubosomes. Since our main goal was the investigation of the structure of cubosomes we prepared them by the ultrasonication method. We obtained many well shaped nanoparticles of Pn3m phase. In the images we can clearly see the internal either cubic or hexagonal structure [92]. We have discovered that smaller particles have spherical shapes and those with the larger sizes are polyhedral.

In the **theoretical part** of the work we were interested in the geometry and stability of interfaces formed when the Pn3m phase is surrounded by an isotropic phase. In particular, we examined the geometry of the facets formed at the droplet of the Pn3m phase. The calculations within the framework of Landau-Brazovskii model with one scalar order parameter related to the local concentration of water were performed. These calculations were done for infinitely large facets built of identical elements. Such approximation works very well for the case of the monocrystals or an interface between two phases. The calculations performed in the continuous Landau-Brazovskii model enabled detailed determination of the structure of the bicontinuous phase. In the continuous model it is much easier to study the facets formed in different directions since the structure of the lattice does not have to be taken into account.

We obtained and investigated small cubosomes by minimization of the Landau-Brazovskii functional. The size of the cubosomes obtained by mathematical modeling was smaller than the size of the cubosomes observed in transmission electron microscope. Nevertheless, these structures may be usefull in understanding the internal structure of the interwoven channels inside the particles especially in the layer close to the facet. The existence of cubosomes with the same symmetries, very similar shapes but different internal structure was observed. These cubosomes have four open channels on each facet and without knowing their internal structure one could incorrectly guess that they are the same. In fact, each cubosome is substantially different from other cubosomes.

We hope that our investigation will be useful in designing new experiment. A significant improvement can be obtained when cubosomes are built of diblock copolymer [93]. These

cubosomes will be larger than those built of phytantriol. Thus, it should be much easier to investigate them for example by AFM.

VII. Acknowledgements

I would like to express my deepest appreciation to all those who provided me the possibility to complete this project. A special gratitude I give to my research supervisor, Doctor Wojciech Góźdź, for the opportunity to participate in the project, for his experience, acquired knowledge, for support and care.

I would like express my gratitude with much appreciation to Professor Paweł Pieranski from the Labotatoire de Physique de Solides from the Université Paris-Sud CEDEX 11 for his parental care. I am grateful for all the knowledge I gained during my research visit in France.

I would like to thank Professor Alina Ciach as well for her assistance and guidance with this project.

I would like to thank Doctor Jéril Degruard for his invaluable help in performing the experiments with cryo-TEM and Doctor Inés Safi for hospitability during the first month of my stay in Orsay.

Furthermore I would also like to thank my loved ones (mother T. Antipina, brother R. Latypov) who have supported me throughout entire process, both by keeping me harmonious and helping me putting pieces together. I will be helpful forever for your love.

VIII. References

[1] B.J. Boyd, Future evolution in colloidal drug delivery systems, Expert Opin. Invest. Drug , 2008, 5, 69-85;

[2] B.J. Boyd, Controlled release from cubic liquid crystalline particles: cubosomes, in Bicontinuous liquid crystals, ed. M.L. Lynch and P.T. Spicer, 2005, pp. 285-306;

[3] B. Ericsson, P.O. Ericsson, J. E. Lafroth and S. Engstrom, Cubic phases as delivery systems for peptide drugs, ACS Symp. Ser., 1991, 469, 251-265;

[4] M. Caffrey, On the mechanism of membrane protein crystallization in lipidic mesophases, Cryst Growth Des., 2008, 8, 4244-4254;

[5] C.V. Kulkarni, W. Wachter, G.I.S. Salto, S. Engelskirchen and S. Almalli, Monolein : a magic liquid?, Phys. Chem. Chem. Phys., 2011, 13, 3004-3021;

[6] E. Nazaruk, K. Sadowska, J.F. Bernat, G. Ginalska amd R. Bilewicz, Enzymatic electrodes nanostructured with functionalized carbon nanotubes for biofuel cell applications, Anal. Bioanal. Chem., 2010, 398, 1651-1660;

[7] E. Nazaruk, S. Smolinski, M. Swatko-Ossor, G. Ginalska, J. Fiedurek, J. Rogalski, and R. Bilewicz, Enzymatic biofuel cell based on electrodes modified with lipid-crystalline cubic phase, J. Power Sources, 2008, 183, 533-538;

[8] E. Nazaruk, A. Michota, J. Bukowska, S. Shleew, L. Gorton and R. Bilewicz, Properties of native and hydrophobic immobilized in the liquid-crystalline cubic phase on electrodes, J. Biol. Inorg. Chem, 2007, 12, 335-344;

[9] P. Rowinski, C. Kang, H. Shin and A. Heller, Mechanical and chemical protection of a wired enzyme oxygen cathode by a cubic phase lyotropic liquid crystal, Anal. Chem. , 2007, 79, 1173-1180;

[10] V. Razumas, J. Kanapieniene, T. Nylander, S. Engstrom and K. Larson, Electrochemical biosensors for glucose, lactate, urea, and creatinine based on enzymes entrapped in a cubic liquid-crystalline phase, Anal. Chem. Acta, 1994, 289, 155-162;

[11] E. Nazaruk, R. Bilewicz, Catalytic activity of oxidases hosted in lipidic cubic phases on electrodes, Bioelectrochemistry, 2007, 71, 8-14;

[12] P. Rowiński, R. Bilewicz, M-J. Stebe, E. Rogalska, Electrodes Modified with Monoolein Cubic Phases Hosting Laccases for the Catalytic Reduction of Dioxygen, Anal. Chem., 2004, 76, 283;

[13] R. Bilewicz, P. Rowinski, E. Rogalska, E. Modified, Electrodes Based on Lipidic Cubic Phases, Bioelectrochemistry, 2005, 66, 3-8;

[14] V. Luzzati and F. Husson, The structure of the liquid-crystalline phases of lipid-water systems, J. Cell Biol., 1962, 12(2), 207-219;

[15] V. Luzzati, A. Tardieu, T. Gulik-Krzywicki, E. Rivas, F. Reiss-Husson, Structure of the cubic phases of lipid– water systems, Nature, 1968, 220, 485–488;

[16] K. Fontell, L. Mandell, P. Ekwall, Some isotropic mesophases in systems containing amphiphilic compounds-Acta Chem. Scand., 1968, 22, 3209–322;

[17] G. Lindblom, K. Larsson, L. Johansson, K. Fontell, S. Forsen, The cubic phase of monoglyceride-water systems. Arguments for a structure based upon lamellar bilayer units., Chem. Phys. Lipids, 1980, 27, 321-328;

[18] K. Larsson, K. Fontell, N. Krog, Structural relationships between lamellar, cubic, and hexagonal phases in monoglyceride-water systems. Possibility of cubic structures in biological systems., Chem. Phys., 1980, 27, 321-328;

[19] A. Yaghmur, P. Laggner, S. Zhang, M. Rappolt, Tuning Curvature and Stability of Monoolein Bilayers by Designer Lipid-Like Peptide Surfactants, PLoS ONE, 2007, 2, 5;

[20] M. Antonio, F. Neto and S.R.A. Salinas, The physics of lyotropic Liquid crystals. Phase transitions and structural properties, Oxford university press, 2005;

[21] W. Buchheim, K. Larson, Cubic lipid-protein-water phases, J. Colloid Interface Sci., 1987, 117(2), 582-583;

[22] T. Landth, Phase behavior in the system pine oil monoglycerides-Poloxamer 407-water at 2000, J. Phys. Chem., 1994, 98, 8453-8567;

[23] G. Clogston, D.J. Craciun, M. Hart, Controlling release from the lipidic cubic phase by selective alkylation, J. Controlled Release, Volume 102, Issue 2, 2005, 441-461;

[24] V. Luzzati, Biological membranes. Academic press, New York San Francisco London, Chap.3, 1968;

[25] S. Abrahamsson, I. Pasher, K. Larssson, K-A. Karlsson, Chem. Phys. Lipids, 1972, 9, 152;

[26] P.A. Winsor, The influenceof composition and temperature on the formation of mesophasesin amphiphilic systems. The R-Theory of fused micellar phases in Liquid Crystals and Plastic Crystals, vol.1, edited by G.W. Gray and P.A. Winsor, Ellis Horwood, 1974;

[27] P. Sotta, Polymorphism of lipid-water systems, J. Phys. II, 1983, 1, 763-772;

[28] P. Pieranski, P. Sotta, D. Rohe, M. Imperor-Clerc, Etude structural de fluids complexes, Phys. Rev. Lett., 2001, 84, 2409-2412;

[29] S. Leroy, J. Grenier, D. Rohe, C. Even, and P. Pieranski, Anisotropoc surface melting in lyotropic cubic crystals, Eur. Phys. J. A, 2006, 19-27;

[30] P. Pieranski, M. Bouchih, N. Ginstet, and S. Popa-Nita, Advances in planar lipid bilayers and liposomes, Eur. Phys. J. A, 2003, 12, 239-254;

[31] P. Pieranski and S. Leroy, Steps and dislocations in cubic lyotropic crystals, J. Phys.: Condens. Matter, 2006, 18, 6453;

[32] K. Larsson, Cubic lipid-water phases: Structures and biomembrane aspects, J. Phys. Chem., 1989, 93, 7304-7314;

[33] J.S. Patton, M.C. Carey, Watching fat digestion, Science, 1979, 204, 145-148;

[34] B. Siekmann, H. Bunjes, M.H.J. Koch, K. Westesen, Preparation and structural investigations of colloidal dispersions prepared from cubic monoglyceride-water phases, Int. J. Pharm., 2002, 244 (1-2), 33-43;

[35] M. Almegren, K. Edwards, J. Gustaffson, Cryo-transmission electron microscopy of thin vitrified samples, Curr. Opin. Colloid Interface Sci., 1996, 1(2), 270-278;

[36] P.T. Spicer, K.L .Hayden, M.L. Lynch, A. Burns, Novel process for producing cubic liquid crystalline nanoparticles (cubosomes), Langmuir, 2001, 17(19), 5748-5756;

[37] P.T. Spicer, W.B. Small, M.L. Lynch, J.L. Burns, Dry powder precursors of 'soft' cubic liquid crystalline nanoparticles (cubosomes), J. Nanopart. Res., 2002, 4(4), 297-311;

[38] L. Norlen, Skin barrier formation: The membrane folding model, J. Invest. Dermat., 2001, 117, 823-829;

[39] L. Norlen, Skin barrier structure and function: The single gel phase model, J. Invest. Dermatol., 2001, 117, 830-836;

[40] J. Borne, T. Nylander, A. Khan, Effect of lipase on monoolein-based cubic phase dispersions (cubosomes) and vesicles, J. Phys. Chem., B 2002, 106 (40), 10492-10500;

[41] D. Wyatt, D. Dorschel, A cubic phase delivery system composed of glyceryl monooleate and water for sustained release of water soluble drugs, Pharm. Dev. Technol., 1992, 16(10), 116-130;

[42] P.B. Geraghty, D. Attwood, J.H. Collet, Y. Dandiker, In vitro release of some antimuscarinic drugs from monoolein/water lyotropic liquid crystalline gels, Pharm. Res., 1996, 13 1265-1271;

[43] T. Norling, P. Landing, S. Engstrom, K. Larsson, N. Krog, S.S. Nissen, Formation of a drug delivery system based on a mixture of monoglycerides and triglycerides for usein the treatment of perodontal desease, J. Clin. Periodontol., 1992, 19, 687-692;

[44] E. Esposito, V. Carotta, A. Scabbia, L. Trombelli, P.P.D. Antona, E. Menegatti, C. Nastruzzi, Comparative analysis of tetracycline-containing dental gels: poloxamer- and monoglyceride-based formulations, Int. J. Pharm., 1996, 142 (1), 9-23;

[45] K. Lindell, J. Engblom, M. Jonstroemer, A. Carlsson, S. Engstroem, Influence of a charged phospholipid on therelease pattern of timolol maleate from cubic liquid crystalline phases, Prog. Colloid Polym. Sci., 1998, 108, 111–118;

[46] C.M. Chang, R. Bodmeier, Swelling of and drug releasefrom monoglyceride-based drug delivery systems, J. Pharm. Sci., 1997, 86 (6), 747–752;

[47] R. Burrows, J.H. Collett, D. Attwood, Release of drugs from monoglyceride-water liquid crystalline phases, Int. J. Pharm., 1994, 111, 283–293;

[48] S.B. Lesile, S. Puvada, B.R. Ratna, A.S. Rudolph, Encapsulation of hemoglobin in a bicontinuous cubic phase lipid, Biochim. Biophys. Acta, 1996, 1285 (2) 246–254;

[49] Y. Sadhale, J.C. Shah, Glyceryl monooleate cubic phase gel as chemical stability enhancer of cefazolin and cefuroxime, Pharm. Dev. Technol., 1998, 3 (4), 549–556;

[50] Y. Sadhale, J.C. Shah, Biological activity of insulin in GMO gels and the effect of agitation, Int. J. Pharm., 1999, 191 (1), 65–74;

[51] M. Nakano, A. Sugita, H. Matsuoka, T. Handa, Small-angle x-ray scattering and 13C NMR investigation on the internal structure of ''cubosomes'', Langmuir, 2001, 17, 3917-3922;

[52] M. Nakano, T. Teshigawara, A. Sugita, W. Leesajakul, A. Taniguchi, T. Kamo, H. Matsuoka, T. Handa, Dispersions of liquid crystalline phases of the monoolein/oleic acid/pluronic F127 system, Langmuir, 2002, 18 (24), 9283-9288;

[53] D. Mcloughlin, M. Imperoe-Clerc, D. Langevin, A new cubic phase containing DNA and a surfactant, ChemPhysChem, 2004, 5, 1619-23;

[54] A. Angelova, B. Angelow, B. Papahadjopoulos-Stemberg, M. Ollivon, Proteocubosomes; nanoporous vehicles with tetriary organized fluid interfaces, Langmuir, 2005, 21, 4138-43;

[55] M. Almgrem, K. Larsson, Gustafsson J, Ljusberg-Wharen H, Cubic lipid-water phase dispersed into submicron particles, Langmuir, 1996, 12, 4611;

[56] S.T. Hyde, Sten. Andersson, B. Ericsson, and K. Larsson, Cubic structure consisting of a lipid bilayer forming an infinite periodic minimum surface of the gyroid type in the glycerolmonooleate-water system, Langmuir, 1997, 13, 6964;

[57] M.L. Lynch, K.A. Kochvar, J.L. Burnes and R.G. Laughlin, Aqueous phase behavior and cubic phase containing emulsions in the C`1`2E`2 water system, Langmuir, 2000, 16, 3537-3542;

[58] J. Barauskas and T. Landh, Phase behavior of phytantriol/water system, Langmuir, 2003, 19, 9562-9565;

[59] P. Pieranski, Thermopermeation in bicontonuous liquid crystals, Liq. Cryst., 2009, 36, 1049 -1061;

[60] T. Plotzing and P. Pieranski, Ratchet effect in faceting. A growth of perfect lyotropic crystals by temperature cycles, Eur. Phys. J. A, 2004, 13, 179-188;

[61] P. Pieranski, New phenomena and a new lyotropic phase detected by isoplethal and hygroscopic method, J. Phys.: Condens. Matter, 2005, 17, S3333-S3339;

[62] J. Grenier, T. Plotzing, D. Rohe and P. Pieranski, Anisotropic surface melting in lyotropic cubic crystals, Eur. Phys. J. A, 2006, 19, 223-232;

[63] A. Prince, page 194 in "Alloy phase equilibria", Elsevier 1966;

[64] An introduction to electron microscopy, FEI;

[65] A. Yaghmur, P. Laggner, M. Almgren, M. Rappolt, Self-assembly in Monoelaidin Aqueous Dispersions: Direct Vesicles to Cubosomes Transition, Plos ONE, 2008, 3(11), 3747;

[66] W. Helfrich, Elastic properties of lipid bilayers: Theory and possible experiments, Z. Naturforsch A, 1973, 28, 693;

[67] C.K. Haluska, W.T. Góźdź, H.G. Döbereiner, S. Förster, G. Giant, G. Gompper, Hexagonal superstructures in diblock-copolymer membranes, Phys. Rev. Lett., 2002, 89, 238302;

[68] W.T. Góźdź, Spontaneous-curvature induced shape transformations of tubular polymersomes, Langmuir, 2004, 20, 7385;

[69] W.T. Góźdź, Influence of the spontaneous curvature and the microtubules on the conformations of lipid vesicles, J. Phys., 2005, B. 109, 21145;

[70] P. Pieranski, Faceting of soft crystals, Advances in Planar Lipid Bilayer and Liposomes, 2011, 14, 1-14, Academic Press;

[71] P.T. Spicer, Progress in liquid crystalline dispersions: Cubosomes, Cur. Opin. Colloid Interface Sci., 2005, 10, 274;

[72] H. Schnering, R. Nesper, Nodal surfaces ofFourier series: Fundamental invariantsof structured matter. J. Phys.: Condens. Matter, 1991, 83, 407-412;

[73] V. Babin and A. Ciach, Double-diamond phase in amphiphilic systems confined between parallel walls, J. Chem. Phys., 2001, 115, 2786;

[74] V. Babin and A. Ciach, Response of bicontinuous cubic D phase in amphiphilic systems to compression or expansion, J. Chem. Phys., 2003, 119, 6217;

[75] W.T. Góźdź and R. Holyst, Triply periodic surfaces and multiply continuous structures from Landau model of microemulsions, Phys. Rev., 1996, E. 54, 5012;

[76] W. Góźdź and R. Holyst, High genus gyroid surfaces of non-positive Gaussian curvature , Phys. Rev., 1994, E. 49, 1478;

[77] G. Gompper and M. Schick, Scattering from Internal Interfaces in Microemulsion and Sponge Phases, Phys. Rev., 1994, E49, 1478;

[78] A. Ciach, J. Pekalski, W.T. Góźdź, origin of similarity of phase diagrams in amphiphilic and colloidal systems with competing interactions, Soft matter, 2013, 9, 6301-6308;

[79] M. Seul and D. Andelman, Domain shapes and patterns: the phenomenology of modulated phases, Science, 1995, 267, 476;

[80] L. Leibler, Theory of Microphase Separation in Block copolymers, macromolecules, Macromolecules, 1980, 13, 1602;

[81] G.H. Fredrickson, E. Helfand, Fluctuation effects in the theory of microphase separation in block copolymers, J. Chem. Phys. 1987, 87, 697;

[82] W.H. Press, B.P. Flannery, S.A. Teukolsky, W.T. Vetterling, Numerical recipes, Cambridge University Press, 1990;

[83] S.A. Brazovskii, phase transition of an isotropic system to a nonuniform state, Sov. Phys. JETP, 1975, 41, 8;

[84] A. Ciach, W. Góźdź, Nonelectrolyte solutions exhibiting structure on the nanoscale, Annual Rep. Prog. Chem., Sect. C, 2001, 269-314;

[85] A. Ciach, J.G.S. Hoye, Bicontinuous phase in a lattice model for surfactant mixtures, J. Chem. Phys., 1991, 95, 5300;

[86] W.E. Lorensen and H.E. Cline, Marching cubes: A high resolution 3-D surface construction algorithm, COMPUTER GRAPHICS, 1987, 21, 163;

[87] D.A. Hoffman, Some basic facts, old and new, about triply periodic embedded minimal surfaces, Colloque de Phyisique, 1990, 51 C7, 197;

[88] D.M. Anderson, H.T. Davis, L.E. Scriven, and J.C.C. Nitsche, Conformationally asymmetric block copolymers, Adv. Chem. Phys., 1990, 77, 337;

[89] S.T. Hyde, Theory of spin relaxation of bicontinuous cubic liquid crystals, Z. Kristallogr., 1987, 187, 165;

[90] A. Ciach, Mechanical, structural and thermodynamic properties of confined self-assemblingsystems, Progr. Colloid Polym. Sci., 2004, 129, 40;

[91] A.L. Mackay, J. Klimowski, Towards a grammar of inorganic structure, Comp. and Maths. With Appls., 1986, 12B, 803-824;

[92] L. Latypova, P. Pieranski, W. Góźdź, Symmetry, topology and faceting in bicontinuous lyotropic crystals, Eur. Phys. J. E, 36, 88, 2013;

[93] T. Smart, H. Lomas, M. Massignani, M. Flores-Merino, L. Perez, and G. Bataglia, Block copolymers nanostructures, J. Nanotoday, 2008, 3, 3-4.